2021

BOOST THE DSICOVERY OF MRP7/ABCC10 SUBSTRATES AND INHIBITORS: ESTABLISHMENT OF NEW IN VITRO AND IN SILICO MODELS

Jingquan Wang

BOOST THE DSICOVERY OF MRP7/ABCC10 SUBSTRATES AND INHIBITORS: ESTABLISHMENT OF NEW IN VITRO AND IN SILICO MODELS

A dissertation submitted in partial fulfillment
of the requirements for the degree of

DOCTOR OF PHILOSOPHY

to the faculty of the

DEPARTMENT OF PHARMACOLOGY

of

COLLEGE OF PHAMACY AND HEALTH SCIENCES

at

ST. JOHN'S UNIVERSITY
New York
by

Jingquan Wang

Date Submitted 07/29/2021 Date Approved 07/31/2021

_____	_____
Jingquan Wang	Dr. Zhe-Sheng Chen

ABSTRACT

BOOST THE DSICOVERY OF MRP7/ABCC10 SUBSTRATES AND INHIBITORS: ESTABLISHMENT OF NEW IN VITRO AND IN SILICO MODELS

JINGQUAN WANG

ATP-binding cassette (ABC) transporters are responsible for the efflux of structurally distinct endo- and xenobiotics energized by ATP hydrolysis. MRP7/ABCC10 belongs to the 10th member of subfamily C and responsible for mediating MDR against a series of chemotherapeutic drugs such as taxanes, epothilones, Vinca alkaloids, anthracyclines and epipodophyllotoxins.

Establishment of new *in silico* and *in vitro* models for MRP7 substrates/inhibitors prediction

Considering the limited knowledge of MRP7, we established a homology model based on bovine MRP1 cryo-EM models. The final model was used for protein global motion analysis and docking analysis. Before docking, potential drug binding pockets were identified and evaluated. Next, MRP7 substrates and inhibitors were docked into drug binding pockets. We found that docked inhibitors and substrates formed separate clusters, from which a substrate binding region and an inhibitor binding region were proposed. This homology protein model enables the docking analysis of potential MRP7 ligands for future studies. Moreover, we established a new SKOV3/MRP7 cell line which exhibits similar drug resistance profile as the previously established HEK/MRP7 cell line. This new cell line is valuable for MRP7 substrates and inhibitors discovery. Last but not the least, we established a novel machine learning model named Mrp7Pred for large-scale MRP7 substrates/inhibitors prediction. The model was also deployed as a web server and

is freely available to users in http://www.mrp7pred.com. We successfully identified 2 substrates and 4 inhibitors from 70 FDA-approved drugs using Mrp7Pred.

New synthetic agents targeting MRP7 and overcomes MRP7-medited MDR

Previously, we identified two synthetic compounds, CMP25 and CP55, as potent ABCB1 and ABCG2 inhibitors. Here we found these two compounds also significantly reversed the MDR mediated by MRP7. Both compounds significantly sensitized MRP7-overexpressing HEK/MRP7 cells to paclitaxel and vincristine. Western blotting indicates that neither CMP25 nor CP55 alters MRP7 expression level. Immunofluorescence showed that the subcellular localization of MRP7 was not altered by these two compounds. However, intracellular accumulation of [^{3}H]-paclitaxel and [^{3}H]-vincristine were significantly increased while the efflux was significantly reduced when co-administered with CMP25 or CP55. Hydrophobic interactions were predicted as the major contributors in stabilizing the drug-protein complex via docking analysis.

ACKNOWLEDGEMENTS

I would specifically express my appreciation to Dr. Zhe-Sheng Chen, who is also my mentor, for all the training and support throughout my Ph. D years. Under the guidance of Dr. Chen, I was able to publish several high-impact papers in well-known journals which already got good citations. It is my great luck as well as honor to join Dr. Chen's lab. I would also like to thank all my lab mates and committee members for their support in my Ph. D research. I also want to thank the Department of Pharmaceutical Sciences for providing tuition coverage and teaching assistance stipend. Last but not the least, I would like to express my appreciation to my friends and families. Without their support in my life, I cannot make it through all these years.

TABLE OF CONTENT

LIST OF TABLES

LIST OF FIGURES

INTRODUCTION

The ABC transporter superfamily

Since the first discovery of the membrane transport protein P-glycoprotein (P-gp) or ATP-binding cassette (ABC) transporter B1 (ABCB1) in drug resistant cancer cells in the mid-1970s, numerous studies have been published regarding ABC transporters and their potential therapeutic roles in cancer and other diseases (1). ABC transporters are the best known for mediating multidrug resistance (MDR) and lead to failure of chemotherapy in cancer. Besides, studies also revealed their importance in cancer beyond efflux pumps such as regulating tumor promoting signaling pathways (2,3). ABC transporter superfamily is composed of 7 subfamilies, namely ABCA to ABCG, which in human derive at least 48 members with different functions. Among the 48 members, approximately 13 ABC transporters (including ABCA2/3, ABCB1/2/5, ABCC1/2/3/4/5/6/10 and ABCG2) are directly relevant to chemoresistance by mediating the efflux of chemotherapeutic agents (4), which subsequently leads to reduced intracellular concentration of drugs in cancer cells and deteriorated therapeutic efficacy. Due to the critical roles ABC transporters played in human cancers, overcoming cancer MDR by targeting the ABC transporters has been prioritized since the development of first generation of ABCB1 inhibitor, although clinical trials using these inhibitors have not yet achieved satisfactory results (5). Developing novel inhibitors of ABC transporters and repurposing approved drugs as ABC transporter modulators are still the major target in this field (6). During recent years, numerous synthesized compounds as well as FDA-approved therapeutic drugs have been discovered as potent ABC transporter modulators

in vitro and *in vivo*, which further extended our knowledge and provided candidates that have the potential for clinical applications.

Multidrug resistance proteins (MRPs)

As mentioned before, increased efflux of multiple chemotherapeutic agents can cause chemotherapy failure due to decreased intracellular drug level and thus limited efficacy (2). Such a phenomenon is termed multidrug resistance, or MDR. ATP-binding cassette (ABC) transporters have been well studied as one of the major factors that mediate MDR in cancer, since many members in the ABC transporter superfamily are responsible for the efflux of structurally distinct anticancer drugs (7). Among all ABC transporters, the ABCC subfamilies have 13 members (ABCC1 to ABCC13), 9 of which were characterized as MRPs (Table 1).(8).

Table 1. Summary of information about MRPs.

	Synonyms	Gene name	Genomic location	Sequence Length	MW. (kDa)	Classification	Subcellular localization
MRP 1	ABCC1	*ABCC1*	chr16 p13.11	1531	190	Long MRP	Basolateral
MRP 2	cMOAT, ABCC2	*ABCC2*	chr10 q24.2	1545	190	Long MRP	Apical, basolateral
MRP 3	MOAT-D, ABCC3	*ABCC3*	chr17 q21.33	1527	170	Long MRP	Basolateral
MRP 4	MOAT-B, ABCC4	*ABCC4*	chr13 q32.1	1325	170	Short MRP	Apical, basolateral
MRP 5	MOAT-C, ABCC5	*ABCC5*	chr3 q27.1	1437	165	Short MRP	Basolateral
MRP 6	MOAT-E, ABCC6	*ABCC6*	chr16 p13.11	1503	165	Long MRP	Basolateral
MRP 7	ABCC10	*ABCC10*	chr6 p21.1	1492	171	Long MRP	Not clear

MRP 8	ABCC11	*ABCC11*	chr16 q12.1	1382	170	Short MRP	Apical, basolateral
MRP 9	ABCC12	*ABCC12*	chr16 q12.1	1356	100	Short MRP	Not clear

Structurally, MRPs share structural features including multiple transmembrane domains (TMDs, also referred to as "membrane spanning domains" or "MSDs") and nucleotide binding domains (NBDs) for ATP binding and hydrolysis. The number of TMDs may differ between MRPs: MRPs 4, 5, 8 and 9 are relatively shorter MRPs since they lack the additional N-terminal TMD0, while the other members (MRPs 1, 2, 3, 6 and 7) are "long" MRPs with TMD0. As a feature found uniquely in only 5 MRPs, the function of TMD0 remains unclear.

Although MRPs have different structures and amino acid compositions, they share a similar mechanism of transport driven by ATP hydrolysis. Unlike P-gp, which extrudes mostly xenobiotics, MRPs are responsible for the extrusion of both endo- and xenobiotics, indicating its important role in regulating physiological processes as well as cancer MDR (2,9). Table 2 summarizes the substrate specificities of MRPs. In a recent structural study of MRP1, the authors revealed the potential transport mechanism and how substrate binding promotes the transport cycle (10). The cryo-EM structure of bovine MRP1 supported a unique substrate recruitment mechanism which is different from P-gp. In brief, substrates of MRP1 are likely to be recruited directly from the cytoplasm, whereas P-gp binds substrates from the inner leaflet of the lipid bilayer (11,12).

Multidrug resistance protein 7 (MRP7/ABCC10)

In 2001, multidrug-resistant protein 7 (MRP7), also known as ABCC10, was discovered as a new member of the ABCC subfamily (13). MRP7, with a mass of 171-kDa, contains three TMDs and two NBDs. MRP7 lacks a conserved N-linked glycosylation site at the N-terminus compared to MRP1-MRP3, and MRP6 which have a similar structural architecture to MRP7 (14). The expression of the *MRP7* gene is strong in a variety of tissues, including pancreas, kidneys, brain, lung, ovary, testis, prostate, colon, leukocytes and skin (15).

MRP7 is a lipophilic anion transporter involved in detoxification, transporting GSH conjugates and glucuronate conjugates (16). Previous reports revealed that MRP7 is a drug resistance factor for various anti-cancer drugs including paclitaxel, docetaxel, vincristine, and vinorelbine (17–20). MRP7 also confers resistance to nucleoside-based agents such as gemcitabine, fluoropyrimidines, and a novel class of natural product agents known as epothilone B (21).

Numerous studies showed that MRP7 expression levels can be a valuable prediction biomarker for the outcome of a variety of cancers. The Hopper-Borge's group determined that MRP7 is highly expressed in $HER2^+$ and ER^+ human breast cancer cell lines BT474, MCF7, and T47D, while the triple-negative breast cancer cell lines BT549, HS578T, and MDAMB-231 expressed the lowest levels of MRP7 (22). Moreover, higher expression of MRP7 was detected in $HER2^+$ and ER^+ breast cancer tumor specimens (22). It was found that tumors grew more quickly in $Abcc10^{-/-}$ mice harboring tumor xenografts than wild-type mice; however, in the $Abcc10^{+/+}$ mice, the tumors displayed increased apoptosis, blood vessel formation, and lung metastasis (22). The results indicated that cell lines derived from $Abcc10^{+/+}$ mice showed active migration compared

to cell lines derived from Abcc10$^{-/-}$ tumors. A previous study showed that the expression of the MRP7 protein is significantly associated with overall survival of colorectal cancer patients undergoing 5-FU-based chemotherapy (23). A low level of MRP7 protein expression was observed in colorectal cancer patients with shorter overall survival. This indicated that low MRP7 expression is predictive of a poor prognosis in colorectal cancer and MRP7 expression is worthy of future validation for its prognostic value. Zhu et al., determined the prognostic significance of ABCC subfamily members in gastric cancer using KaplanMeier survival analysis (24). The results showed that MRP7 was significantly associated with both negative and positive HER2 status. High expression of MRP7 indicated a poor prognosis. Thus, MRP7 may be a significant potential prognosis biomarker for gastric cancer (24). The association of MRP7 expression with paclitaxel sensitivity was tested in non-small cell lung cancer (NSCLC) cells. The results revealed that high expression levels of MRP7 led to a significantly lower paclitaxel sensitivity in 17 human NSCLC cell lines (25). Thus, MRP7 expression is a predictive biomarker for paclitaxel resistance in NSCLC. Apart from the association with cancer, a recent study indicated that MRP7 expression is primarily correlated with regular growth of the cell population instead of cell cycle progression (26). Overall, it is very important to deepen our understanding in overcoming MRP7-mediated cancer drug resistance.

Machine learning and drug discovery

Before the significant advancement of machine learning and deep learning algorithms, researchers have been implementing ligand-based and structure-based models for high-throughput screening of drug candidates. Discovering ABC transporter modulators was also one of the major tasks in this field. Conventional methods include

Hansch analysis, pharmacophore modeling, linear and non-linear regression. Later, with the development of machine learning techniques, supervised and unsupervised artificial neural networks have been widely applied in ABC transporter ligand prediction (27). In this section, several most popular machine learning algorithms used in drug design and discovery were introduced.

Support vector machine (SVM)

Support vector machine (SVM) is one of the most popular supervised non-linear classification models in machine learning. It was first proposed by Vapnik in 1992, used a supervised machine learning approach based on a statistical learning theory called Vapnik Chervonenkis Theory. In brief, SVM is a marginal classifier, which works by finding the optimal hyperplane to separate data with different labels at maximum margin (28). Different from fundamental marginal classifiers, SVM innovatively involved the kernel functions (such as linear, polynomial and radial basis function kernel) to transform original data into higher dimensional spaces, so that it has non-linear classification capabilities (29). The term "support vector" stands for a set of data points that locates on the margins. Given a labelled dataset:

$$(x_1, y_1), \dots, (x_n, y_n), x_i \in \mathbb{R} \; and \; y_i \in \{-1, 1\}$$

where x_i is a feature vector and y_i is the class label. Here the label was set 1 and -1 for reasons explained below. Then the optimal hyperplane is defined as:

$$D(x) = wx^T + b$$

where w is the learnable weight vector and b is the learnable bias that SVM will learn via the training process. Then the margin could be expressed as a minimal τ that holds:

$$\frac{y_i D(x_i)}{||w||} \geq \tau$$

Then we can apply a constraint $\tau||w|| = 1$. Here, maximizing the margin τ is equivalent to minimizing $||w||$. To simplify the calculation, we can convert the problem to minimize $\eta(w) = \frac{||w||^2}{2}$, which subject to constraints:

$$|y_i| \, (wx_i^T + b) \geq 1$$

This problem could be solved by introducing the Lagrange multipliers:

$$Q(w, b, \alpha) = \frac{1}{2}||w||^2 - \sum_{i=1}^{n} \alpha_i [y_i (wx_i^T + b) - 1]$$

Here $\alpha_i's$ are Lagrange multipliers. By differentiating and substituting ***w***, we get

$$\max \; Q(\alpha) = \sum_{i=1}^{n} \alpha_i - \frac{1}{2} \sum_{i,j=1}^{n} \alpha_i \alpha_j y_i y_j (x_i x_j)$$

subject to $\sum_{i=1}^{n} y_i \alpha_i = 0, \; \alpha_i \geq 0, \; i = 1, \ldots n$

To enable the soft margin, the optimization could be reformulated as $minimize \; \eta(w) = \frac{||w||^2}{2} + C \sum_i \xi_i \, , where \; y_i (wx_i^T + b) \geq 1 - \xi_i$. Here when $\xi_i's$ are not zero, vectors are allowed to locate within the margins. *C* is the penalty factor, a tunable parameter of SVM.

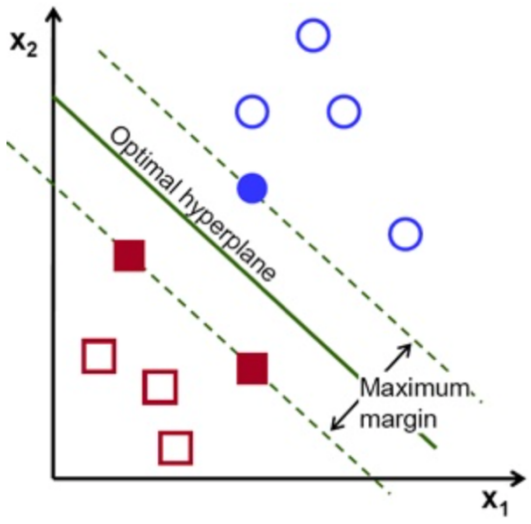

Figure 1. SVM illustration. Positive and negative were displayed as blue circles and red squares, respectively. Support vectors were represented as solid shapes. The hyperplane was represented as green solid line.

Figure 1 showed an illustration of SVM classifier. The reason why SVM could solve non-linear problems is the introduction of kernel functions (30). The main idea of kernel functions is to add additional dimensions to the training data and convert the problem to a linear problem in higher dimensional space. The most common kernel functions include linear kernel, Gaussian kernel and polynomial kernel. The representation of each kernel is given below:

$$K_{linear}(\boldsymbol{x_1}, \boldsymbol{x_2}) = < \boldsymbol{x_1}, \boldsymbol{x_2} >$$

$$K_{Gaussian}(\boldsymbol{x_1}, \boldsymbol{x_2}) = \exp\left(-\gamma \left|\left|\boldsymbol{x_1} - \boldsymbol{x_2}\right|\right|^2\right)$$

$$K_{polynomial}(\boldsymbol{x_1}, \boldsymbol{x_2}) = (< \boldsymbol{x_1}, \boldsymbol{x_2} > +1)^d$$

Linear kernel is the standard scaler product. The Gaussian kernel is also known as RBF kernel, where γ is the inverse-width parameter which is related to the number of support vectors. In polynomial kernel, the parameter d is the degree of polynomial function (31).

Various SVM models for drug discovery has been developed over the past decade, and SMV has shown promising performance in compound activity prediction and non-linear structure-activity relationship modeling (32). However, intuitive accessibility is one of the major shortcomings of SVM which makes it hard to illustrate the chemical terms (33).

Random forest

Random forest is another supervised learning algorithm that could be applied to classification and regression (34). In brief, it is a combination of decision tree predictors where each tree predicts based on a random independent vector derived from the feature vectors (35). Random forest has been widely used in different fields including drug discovery (Figure 2) (36).

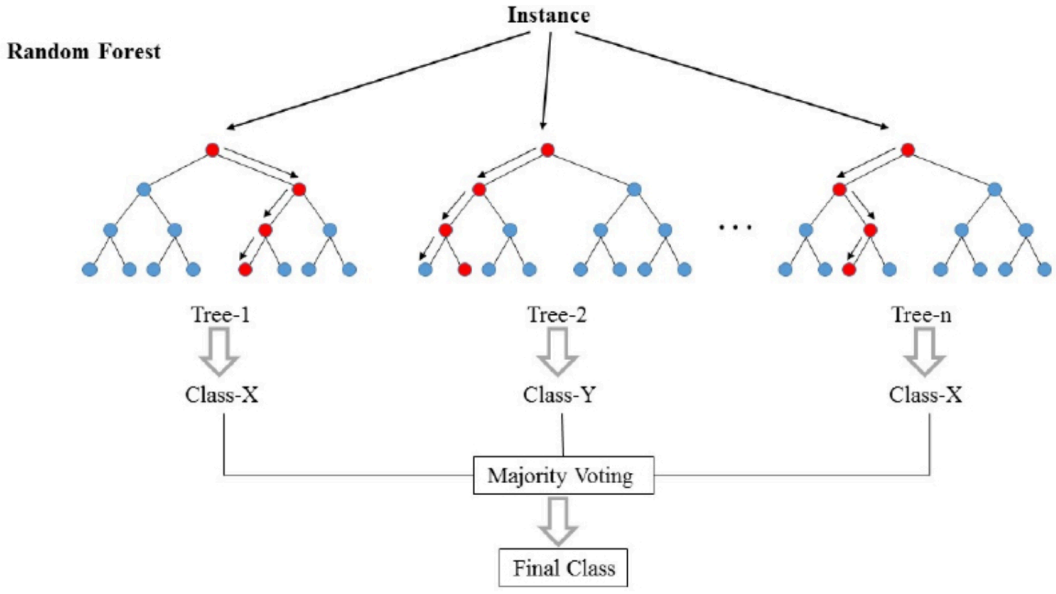

Figure 2. An illustration of random forest method.

Random forest is composed of B decision trees $\{T_1(X), \dots, T_B(X)\}$ where $X = \{x_1, \dots, x_m\}$, an m-dimension vector of features (molecular descriptors, fingerprints, or other quantitative properties). Then the forest outputs B independent predictions $\{\widehat{Y_1} = T_1(X), \dots, \widehat{Y_B} = T_B(X)\}$. Outputs of the forest are the aggregated prediction of all trees. In classification problems, the final output is produced by the majority of trees (voting); in regression problems, the final output is the average of individual tree predictions (37). The first step of the training procedure is drawing a bootstrap sample (i.e. random sampling, with replacement, *n* batches) from the training data. Then for each bootstrap batch, grow a decision tree based on a random subset of the whole feature vector. Here the maximum size of subsets is a tunable parameter. Trees are grown till the maximum size is reached (no splits are available) and leave without pruning. The training stops until B trees were successfully generated. If we use all features to grow each tree, the algorithm is then same as bagging (38). The reasons why random forest is efficient are: 1) the feature subset could be very small, thus each tree could be quickly split and grown; 2) there is no pruning for individual trees in random forest (39).

Boosting and the out-of-bag performance estimation

Boosting is another ensemble learning algorithm based on decision trees (40). In brief, boosting is a sequence of trees, and each tree is trained on all training data. In classification problems, data weight will be altered based on whether previous trees misclassified the data. In regression problems, trees were grown based on the residual of previous trees (41). The final prediction is given by weighted voting or average for classification or regression, respectively.

In practice, obtaining labeled data could be expensive and time-consuming. Thus people use different methods of cross-validation to improve the performance (42). Random forest performs cross-validation in a parallel manner with training using the Out-out-bag (OOB) samples (43). The OOB samples are generated from the sampling procedure, where bootstrapping samples were performed where part of the training data will not be selected to construct trees. As a result, each tree will have a collection of "left-out" data—the so-called OOB samples. We can then calculate the error rate (ER, for classification) or mean square error (MSE, for regression) from the ensemble prediction $\hat{Y}^{OOB}(X_i)$:

$$ER \approx ER^{OOB} = \frac{1}{n}\sum_{i=1}^{n} I(\hat{Y}^{OOB}(X_i) \neq Y_i)$$

$$MSE \approx MSE^{OOB} = \frac{1}{n}\sum_{i=1}^{n} \left(\hat{Y}^{OOB}(X_i) - Y_i\right)^2$$

It has been shown that the OOB estimation works reasonably well as k-fold cross-validation. As a result, random forest does not require additional cross-validation (44).

Supervised learning approaches in drug discovery

We have introduced the most commonly used supervised learning methods in previous sections. Here, we briefly introduce some of the state-of-the-art implementations of supervised machine learning algorithms in drug discovery.

Machine learning models have been heavily involved in the whole drug discovery pipelines including target identification and validation, compound screening and lead discovery, preclinical development as well as clinical development. Virtual screening (VS) is a key step in the process of drug development. Over the past decades, VS has evolved from traditional similarity searching to data mining and machine learning

approaches, which require large amount of training data. In the past few years, machine learning methods have been proved to boost the drug discovery techniques such as docking analysis. For example, Sato *et al.* showed SVM and RF models outperformed GlideScore when at least 5 crystal structures were used for model building (45). Abdo *et al.* proposed a similarity-based VS approach using Bayesian inference network (46). Most recently, with the wide availability of graphical processing units (GPUs) that greatly accelerate the parallel processing, more complex models, such as deep neural network models, were enabled and proved enormous increase in different types of tasks (47). Costa *et al.* built a tree-based classifier to predict genes associated with morbidity and druggability. The classifier is trained on protein topology network, metabolic and transcriptional interactions (48). In 2017, Pande *et al.* constructed a large benchmarking dataset name MoleculeNet, which contains properties of over 700,000 compounds, which has been widely used for benchmarking ML algorithms (49). Recently, researchers at AstraZeneca used generative RNNs to design compounds with optimal physiochemical properties, which greatly expanded the chemical space (49). In summary, there is a tendency to implementat machine learning models in drug-target interaction prediction, including inhibitors or substrates of ABC transporters.

CHAPTER 1

In this chapter, we mainly discussed our work in establishing a homology MRP7 protein model. Some essential background knowledge about homology modeling is introduced. The computational methods are described in detail. Overall, we built a MRP7 homology model and performed molecular docking to validate the structure. We also performed molecular dynamics simulation in order to get some insights on the protein structural dynamics and functions.

1.1 Introduction

ABCC10/MRP7 was first discovered in about 20 years ago from expressed sequence tag databases mining (13) and its transport properties were determined subsequently (16). MRP7 was proved to be able to transport multiple types of substrates including amphipathic anions such as 17β-estradiol 17-(β-D-glucuronide) ($E_2$17βG), natural product and derivatives including *vinca* alkaloids such as vincristine and taxanes such as paclitaxel (13,50). *In vitro* and *in vivo* studies have suggested that MRP7 was responsible for mediating MDR in cancer cells (55–57) and down-regulated MRP7 expression by targeting its gene expression could enhance cellular sensitivity to chemotherapeutic drugs (58). Besides, our group has discovered that MRP7 could be functionally regulated by tyrosine kinase inhibitors, phosphodiesterase inhibitors, Raf kinase inhibitors, fibroblast growth factor inhibitors and other small molecule drugs, leading to reversed MDR in resistant cancer cells (59–64).

Clinically, MRP7 has been reported to play important roles in acquired MDR and the prognosis of certain cancers (51,65). Additionally, MRP7 participates in FOXM-induced 5-FU resistance in colorectal cancer patients based on the strong correlation

between mRNA levels of MRP7 and FOXM in tumor tissues. Furthermore, MRP7 also contributes to alteration in intracellular permeation of nevirapine, a non-nucleoside reverse transcriptase inhibitor for HIV-1 (66). As a result, further understanding the structural features and transportation mechanisms of MRP7 is crucial in increasing the survival rate of patients with limited response to chemotherapy due to acquired MDR, as well as developing and discovering substrates/modulators to overcome MRP7-mediated MDR or decreasing unexpected synergistic toxicity in combinational chemotherapies. However, due to the difficulty and cost in obtaining crystal structure of membrane protein, no high-resolution structure of human MRP7 is available so far. Previously, the cryo-EM structure of bovine MRP1 was reported at 3.1-3.5 Å with inward- and outward-facing conformations (10,67). Although there are significant differences between MRP1 and MRP7 in length, size, amino acid sequence and transportation pattern, it still provides possibility to construct high-quality homology models of MRP7 via computational strategies. Here, we present the homology models of MRP7 combining current knowledge of the transporter and the homology modeling methods based on the cryo-EM structure of MRP1 in order to: 1) provide a functionally validated human MRP7 homology model; 2) assess the structural dynamics to identify potential conformational changes associated with efflux mechanism; 3) evaluate the behavior of reported substrates and modulators of MRP7 by analyzing ligand-protein interactions. Also, extra docking simulations were performed using template MRP1 and our homology model to further validate that the MRP7 model was not biased towards its templates. Our study will provide rational insights in the drug development or repurposing of MRP7 modulators.

1.2 Computational methods

Homology modeling of human MRP7 and structure refinement

Human MRP7 sequence (validated *in vitro*) was obtained from the publication by Hopper et al., where human MRP7 was first discovered and expressed (13). Before modeling, a BLAST (basic local alignment search tool) search was performed on PDB by using MRP7 protein sequence to find suitable templates. Bovine MRP1 proteins (5UJA) were selected as templates considering the identity and resolution.

A common homology modeling procedure include template alignment, alignment adjustment, backbone establishment, loop/side chain prediction and model refinement (68). In this study, we used the homology modeling tool Prime provided by Schrodinger Suite and visualized in Maestro 11 (Schrödinger, NY). The TMD0 region of MRP7 was eliminated before alignment. For each conformation, we created 50 initial models (totally 100) followed by loop refinement provided in Schrodinger Prime and subjected to quality assessment.

Protein structure assessment

Generated homology models were evaluated for structure integrity to select the one with best quality as judged by Ramachandran favored residues, main chain (M/c) bond lengths and bond angles (69), peptide bond planarity (70) and zDOPE (normalized Discrete Optimized Protein Energy) score (71). Models with zDOPE score closer to -1.0 have better quality. The Ramachandran plots, M/c bond lengths/angles and peptide bond planarity scores were calculated using PROCHECK (72). Furthermore, the QMEANBrane (73) function was applied to better assess transmembrane protein model quality. Moreover, QMEAN Z-score (74), ERRAT (75) and MolProbity (76) scores were

also calculated. In brief, 1) QMEAN Z-score evaluates how a protein model is in agreement with one would expect from experimental structures of similar size. The Z-score is an integration of global (QMEAN4) and local (QMEAN6) estimates of protein quality. Scores closer to zero indicates good structural quality (74). 2) ERRAT scores describe the overall quality of a protein model, and higher score indicates better quality. The normally accepted range for ERRAT score is > 50 (75). 3) MolProbity score is a combined protein quality score which indicates the expected resolution of a possible crystal structure of similar quality with tested protein model. Thus lower MolProbity score means better quality (76).

Membrane system and molecular dynamics simulations

Molecular dynamics simulation was set up and performed as previously described with modifications (77). MD simulation system was built using the system builder tool provided in Desmond (D.E. Shaw Research, NY). The membrane systems for inward-facing MRP7 were built separately. A POPC membrane with a predefined TIP3P solvent model was established for simulation run. Na^+ and Cl^- ions were added to neutralize the overall charge of the system. The MD simulation was performed in periodic boundary conditions (PBC). After a default relaxation protocol, the simulation was performed as *NpT* runs used Nose–Hoover thermostat (78) and Martyna–Tobias–Klein barostat (79) methods with isotropic coupling under temperature 300K and pressure 1 bar for 100 ns. All MD runs for substructure dynamics analysis were performed independently for 3 times with different random seeds. All simulations were performed in Ubuntu 18.04 system with an NVIDIA Tesla P100 GPU. In total 1000 frames were generated and subjected to a principal component analysis (PCA) for protein motion pattern prediction

using ProDy (80) with in-house python (3.6) scripts and visualized through the NMWiz plugin in VMD (81).

Binding sites identification

Inward-facing human MRP7 homology model was prepared for binding site search as previously described (82,83). In brief, the protein model was preprocessed using the Protein Preparation Wizard provided in Schrodinger Suite. Preprocessing steps including adding hydrogen atoms, assign bond orders and remove water molecules. Binding pockets were identified using SiteMap in Schrodinger Suite and visualized in Maestro 11 (Schrödinger, NY).

Molecular docking

Docking simulations were performed using AutoDock Vina (1.1.2) (84). The protein model and the ligands were modified by adding hydrogen atoms and partial charges in AutoDockTools (1.5.4). Docking grid center and size were determined according to the binding pocket surrounded by TMDs of MRP7 as well as MRP1 (MRP1 binding pocket was determined by co-crystalized ligand). Specifically, the docking grid was determined by the center coordinates of the predicted binding region. The size of the grid box is 30 Å • 30 Å • 30 Å. Each docking run generated 10 poses with the highest docking score. All other parameters were set as default. The ligands with highest affinity score were exported for visualization and further analysis. The 2D interaction diagram was generated by Maestro provided by Schrodinger. The 3D ligand-protein figure was generated using UCSF Chimera (v. 1.14). Protein surface was colored by electrostatic potential which was calculated by the Coulombic Surface Coloring module.

Binding pocket characterization

Volume of the MRP1 and MRP7 drug binding pockets were calculated using SiteMap provided by Schrodinger. For hydrophobicity, we randomly sampled 50-60 amino acids with docked/crystalized ligands in the center. We used Kyte-Doolittle amino acid hydrophobicity scale (KD hydrophobicity score) to calculate the overall hydrophobicity of the pockets. Weighted hydrophobicity scores were calculated by:

$$Weighted\ hydrophobicity = \frac{Number\ of\ selected\ residue}{Number\ of\ sampled\ residues} \times\ KD\ hydrophobicity\ score$$

Statistical analysis

In this study, we performed statistical analysis to evaluate the difference of 1) Molecular dynamics (MD) simulations for sub-structural dynamics analysis; 2) comparing the overall RMSD of MRP7 with or without linker 2; 3) Compare the hydrophobicity of MRP1 and MRP7 binding pockets. Only trajectories after equilibration (50 ns) were considered for statistical analysis. *In vitro* MTT assay in this study was generated from at least three independent triplicated experiments. Results were presented as mean ± SD. All pair-wise comparison were performed used one-way ANOVA followed by post hoc analysis.

1.3 Results

MRP7 homology modeling and structure refinement

A proper template is determined by multiple factors including sequence identity, resolution, functional similarity and sequence alignment, which are essential for identifying conserved regions, ligand binding sites as well as structural domains (85). Here, the bovine MRP1 (MRP1) with inward-facing (PDB ID: 5UJA) (10) conformations

was chosen as modeling template according to the high identity rate among top alignments shown in Table 2. The resolution of 5UJA is 3.34 Å.

Table. 2. Top alignments of MRP7

PDB ID	Title	Length	Identity (%)	Gaps	E value	Resolution (Å)
6BHU	Chain A, Multidrug resistance-associated protein 1 [Bos taurus]	1659	**34.80%**	9.13%	0.0	3.14
5UJA	Chain A, Multidrug resistance-associated protein 1 [Bos taurus]	1460	**34.88%**	9.13%	0.0	3.34
6C3O	Chain E, ATP-binding cassette sub-family C member 8 [Homo sapiens]	1581	28.88%	12.88%	0.0	3.90
5WUA	Chain E, SUR1 [Mesocricetus auratus]	1582	30.89%	11.89%	0.0	5.60
5YKE	Chain B, ATP-binding cassette sub-family C member 8 isoform X2 [Mesocricetus auratus]	1582	30.89%	11.89%	0.0	4.11
5TWV	Chain B, ATP-binding cassette sub-family C member 8 [Cricetus cricetus]	1590	30.74%	11.89%	0.0	6.30

The final model was shown in Figure 3A. In this study, TMD0 was not included in our homology model because the TMD0's in the templates were not completely resolved. Furthermore, previous studies have shown that removal of TMD0 did not affect the function of MRP1 protein (86). According to the sequence alignment, MRP1 and MRP7 share similar structural domains including transmembrane domains (TMDs), Lasso (L_0 linker) and nucleotide-binding domains (NBDs) (Figure 3B-F). The alignment contains conserved region of NBDs shared by multiple ABCC members including the Walker A, Signature and Walker B (13) (Figure 3D, F). The consensus ATPase sites are used for establishing the Mg-ATP system (10).

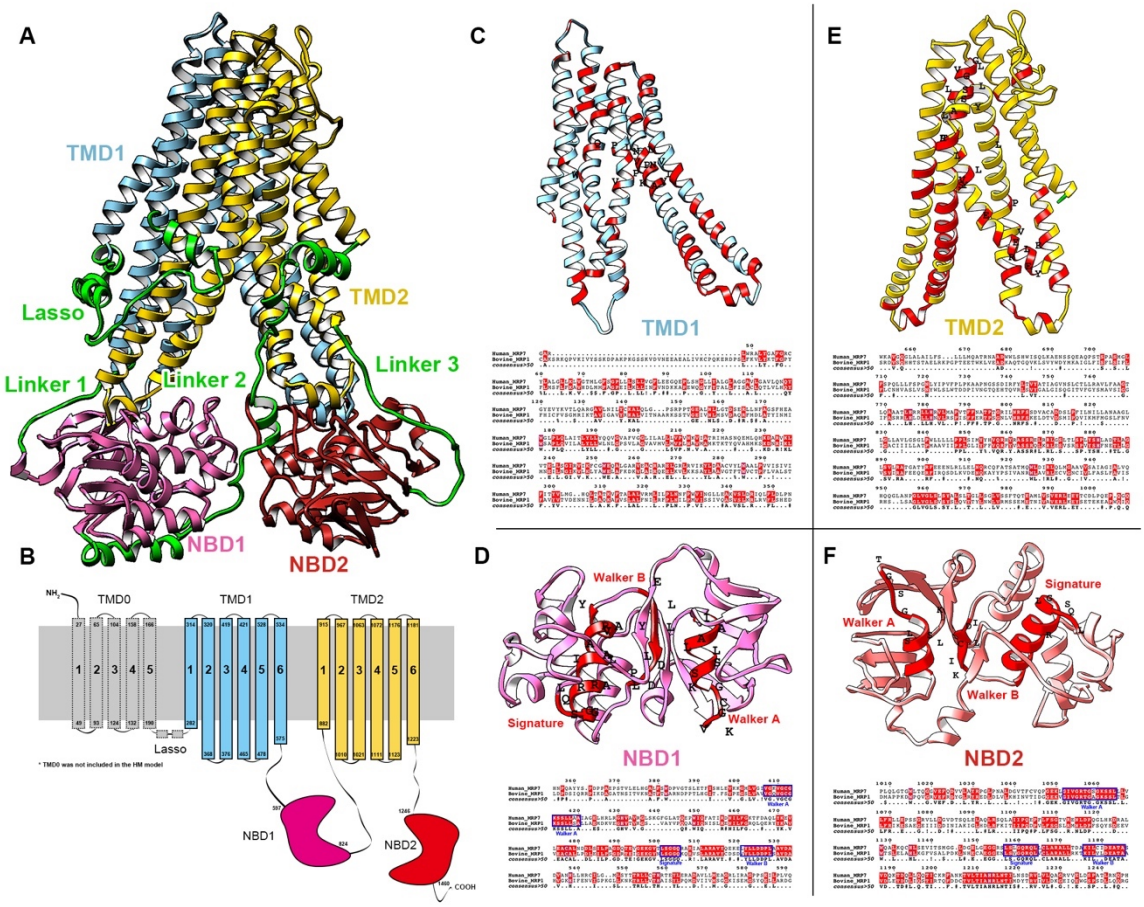

Figure 3. Sequence alignment of MRP1 and MRP7. A) Homology model of human MRP7. Key domains were colored as Lasso/Linker 1/Linker 2/Linker 3: green; TMD1: blue; TMD2: yellow; NBD1: pink; BND2: red. B) Topological structure of human MRP7. Key domains were colored and labeled. C-F) Top: Predicted TMD1 (C) / NBD1 (D) / TMD2 (E) / NBD2 (F) structures of human MRP7. Amino acids with high identity to template were colored red. Conserved region of NBDs including Walker A/B and signature were labelled. Bottom: Sequence alignment of human MRP7 and bovine MRP1. The alignment map was generated using ESPript server (87).

Initial models were subjected to a loop refinement procedure provided by Schrodinger Prime module. Refined MRP7 models were subjected to a series of structural assessment to determine the best model for further studies. Additionally, cryo-

EM structures of MRP1 were also evaluated with same functions. Top results were shown in Table 3. From the results, we found the homology model of MRP7 maintained high percentage of residues in Ramachandran favored regions (91.5% for pre-MD and 91.2% for post-MD). Also, the structures got the most favored main chain layouts indicated by the three PROCHECK scores (M/c bond lengths, bond angles and planar groups). For both pre-MD and post-MD, most of the residue main chain bond lengths (99.5% for pre-MD and 99.1% for post-MD), main chain bond angles (99.4% for pre-MD and 98.9% for post-MD) and planar groups (96.4% for pre-MD and 96.0% for post-MD) fall in reasonable range. Both crystal structures also got acceptable zDOPE, ERRAT, MolProbity and QMEAN Z-scores. The best models were selected and used for MD production runs.

Table 3. Structure assessment of top models

	Ramachandran favored [up to 100%]	M/c bond lengths [up to 100%] [1]	M/c bond angles [up to 100%] [2]	Planar groups [up to 100%][3]	zDOPE [down to -1]	ERRAT [up to 100]	MolProbity [down to 0]	QMEAN Z-score [up to 0]
Inward-facing models								
Pre-MD	91.5%	99.5%	99.4%	96.4%	-0.64	89.33	3.85	-1.65
Post-MD	91.2%	99.1%	98.9%	96.0%	-0.79	77.72	3.26	-1.96

[1]: percentage of main chain bonds within the allowed range
[2]: percentage of main chain angles within the allowed range
[3]: percentage of peptide bonds within the allowed planarity range

Domains of MRP7 were determined according to the secondary structure of homology models as well as previous reports (13). Although MRP7 belongs to the “long”

class of ABCC family, our model does not contain TMD0 domain due to the incompleteness of TMD0 structure in both templates (54). Similar to MRP1, TMD1 and TMD2 are the major transmembrane domains of MRP7 which forms the binding pocket for substrates as well as responsible for the transportation mediated by conformational change. The two cytosolic NBDs are responsible for ATP binding and triggering the conformational change of the protein.

When considering the final refined structure after 100 ns MD runs, the Ramachandran plots of MRP7 were shown in Figure 4. The overall structure of MRP7 is maintained with 91.2% (inward-facing) residues in most favored region (Figure 4). These results indicated that the final remained similar quality compared with the initial model after 100 ns MD run. The following results and discussion will be based on the MD-refined model unless otherwise stated.

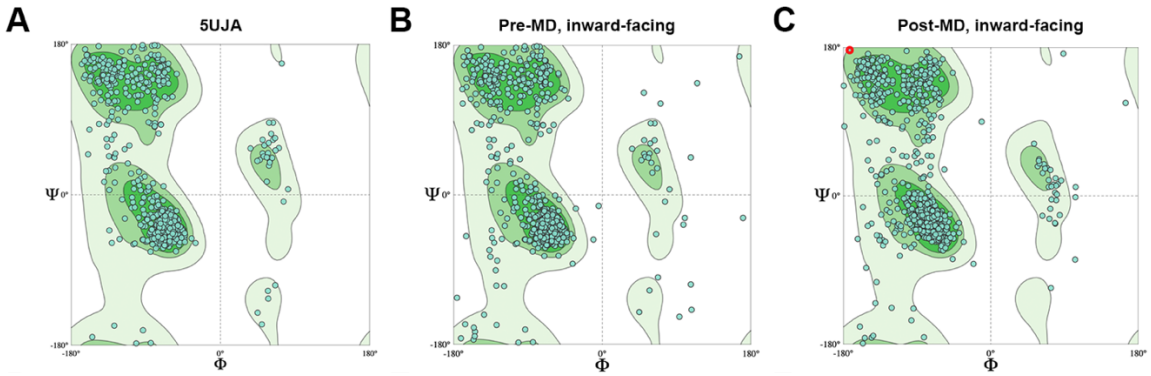

Figure 4. Ramachandran plots of template crystal structure 5UJA (A), initial model (B), MRP7 at the end of 100 ns MD run (C).

The structure deviation of each MRP7 domain was analyzed separately from the MD run using the root mean square deviation (RMSD). The results were displayed in Figure 5. Overall, RMSD value of the whole MRP7 model increased in the first 50 ns,

reaching a plateau of ~5 Å until the end of the simulation. For RMSDs of separate domains, we found that the linker regions (linker 1 between TMD1 and NBD1 and linker 2 between NBD1 and TMD2) are the major contributors to the total RMSD with final RMSD at around 6 Å and relatively higher variation compared to other substructures. Linker 3 (Between TMD2 and NBD2) also showed higher equilibrated RMSD compared to TMDs and NBDs, but significantly less than linker 1 and 2. TMDs and NBDs remained stable eventually at 2.5 – 3.0 Å.

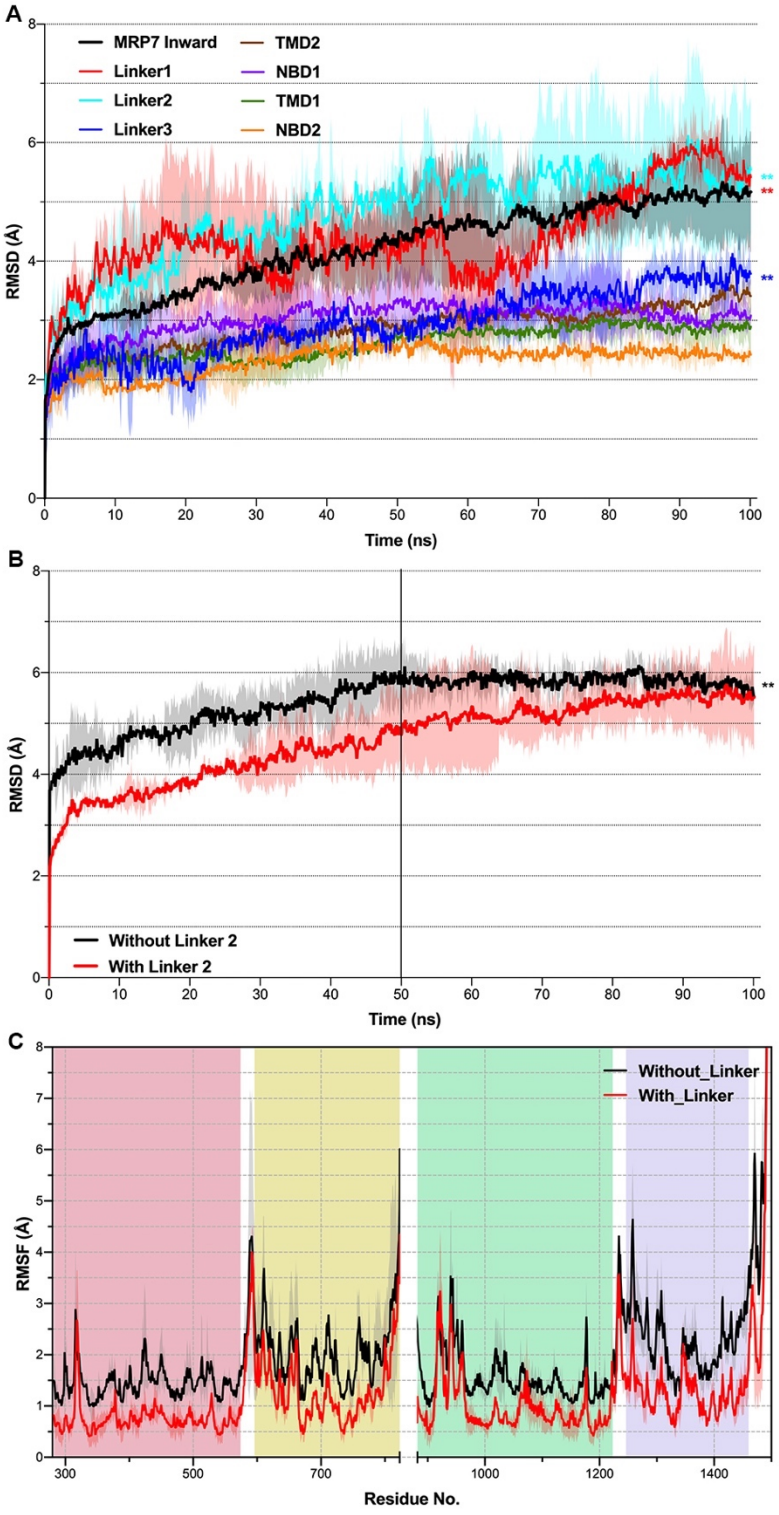

Figure 5. Structure deviation of MRP7 substructures in the 100 ns run. A) The RMSDs of MRP7 substructures were plotted against time (ns). B) RMSD of MRP7 with linker

(black) or without linker (red) in 100 ns MD run. C) RMSF of residues with linker (black) or without linker (red) in 100 ns MD run. Residue numbers were shown in x-axis and segmented by domains: Red: TMD1; yellow: NBD1; green: TMD2; purple: NBD2. Shadow regions indicate standard deviation of 3 independent MD runs. **$p < 0.01$ via one-way ANOVA test compared with non-linker structures.

The cryo-EM structure of MRP1 lacks the linker 2 structure between NBD1 and TMD2 probably due to its unstable conformation as well as flexibility. Here, we analyzed the role of the *de novo* linker 2 structure in MRP7. Results showed that linker 2 in MRP7 contributes positively to the overall stability of the protein (Figure 5B) since the equilibrated RMSD of MRP7 without linker 2 is significantly higher than the one with linker, although its structure showed intense fluctuation and flexibility according to our RMSD data (Figure 5A). Furthermore, in the full system containing POPC membrane, missing linker resulted in increased fluctuation of residues (Figure 5C).

Protein global motions

The protein global motion was analyzed by PCA function provided in ProDy (80). The major motion of protein backbone along specific directions was represented by eigenvectors derived from the covariance matrix calculated from consecutive MD trajectories (88). In inward-facing MRP7, the NBDs showed higher mobility and a pendular motion parallel to the cytoplasm plane and approach each other. Also, the linker 2 structure showed opposite motion direction in upper and lower segment. Specifically, the upper segment which connects to TMD2 moved to the same direction as NBD2, while the lower segment moved to the same direction as NBD1. Thus, we infer that the

linker absorbs forces generated in intensive movements and caused lagged equilibration and less residue fluctuation compared to when no linker 2 was present (Figure 6). The TMDs did not show as significant motions as NBDs, but slight oscillatory movements along with connected NBDs were observed. Although such movements of TMDs did not disturb the arrangement of transmembrane helices, such trend revealed the mechanism of initial motions before ATP-binding-triggered ligand affinity change. TMDs were connected to NBD1 and NBD2 by linker 1 and linker 3 respectively, which seemed to play a similar role in signal propagation between NBDs and TMDs as the SP domains in ABCG2 (53).

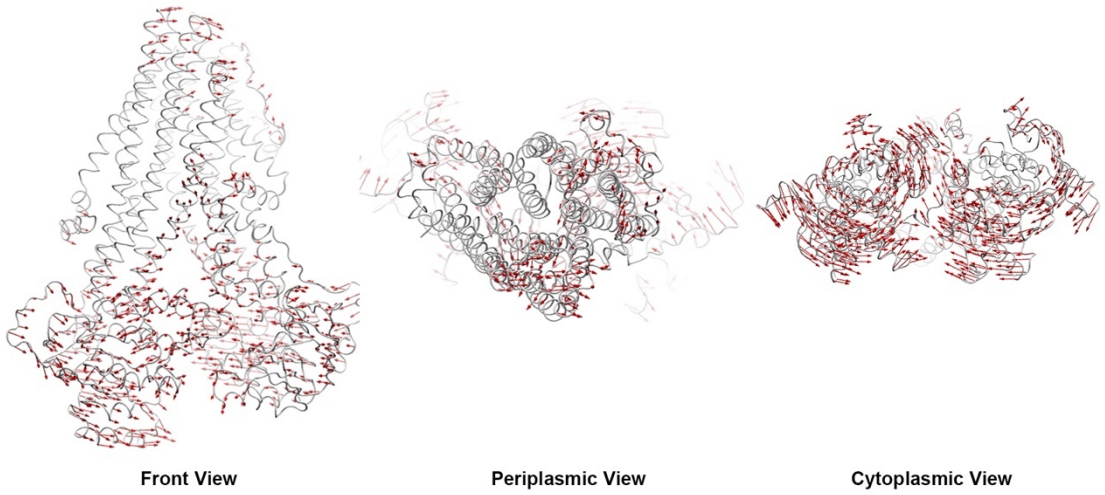

Figure 6. Global motion pattern of inward-facing MRP7. Red arrows indicate potential domain motion direction and distance by PCA analysis. Motions below 1.5 Å were hidden.

Binding pockets identification and validation

To validate the function of our MRP7 model, potential binding pockets were identified (Figure 7) for docking analysis (inward-facing). Five potential binding pockets

were identified. According to Figure 7A, the yellow pocket embedded in the TMDs was the one we are interested in, since its position is consistent with the general binding pockets of ABC transporters such as ABCB1 and ABCG2, which also have functional binding pockets buried in TMDs. Other binding pockets locate either in TMDs or around NBDs. Figure 7B and 7C showed the electrostatic potential of the binding pocket as well as the shape. The volume of this pocket is around 1170 $Å^3$, with the Leu549 stands out in the center and separates the pocket into two "chambers".

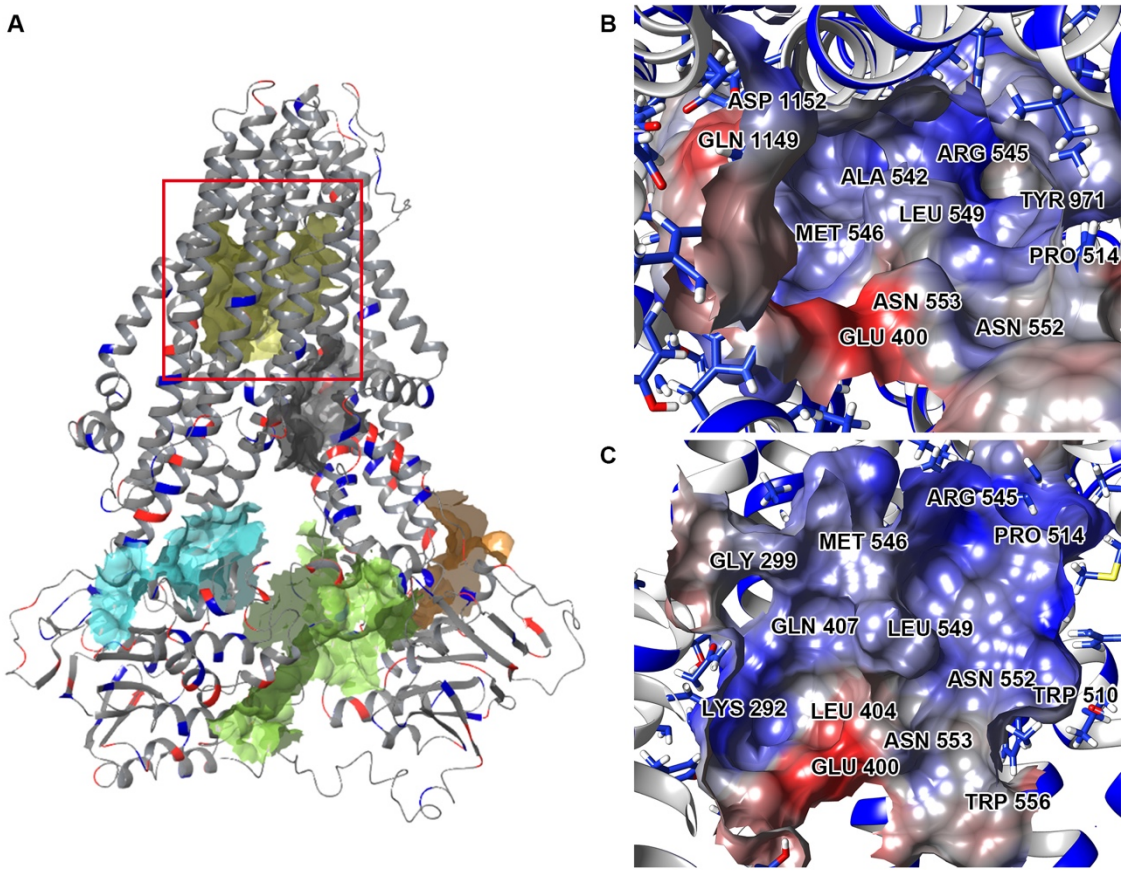

Figure 7. Predicted binding pockets of inward-facing MRP7. A) All predicted binding pockets were displayed with colored solid surface. The pocket marked by the red square was the selected binding pockets for docking analysis. B-C) Cytoplasmic (B) and front

(C) view of the marked binding pockets. Molecular surface was colored by residue electrostatic potential (red: negative; blue: positive).

Investigations of the transport properties of MRP7 revealed its ability to efflux conjugates such as 17β-estradiol-(β-D-glucuronide) ($E_2$17 β G) and leukotriene C_4 (LTC_4) (16). Also, MRP7 is responsible for mediating the efflux of structurally-distinct chemotherapeutic agents including doxorubicin, vincristine, docetaxel, paclitaxel, vinblastine (89) and vinorelbine (90). Moreover, our lab has previously discovered several small-molecule drugs being MRP7 modulators including nilotinib (61), lapatinib (62), cepharanthine (91), sildenafil (92), tariquidar (93), epothilone B and sulfinpyrazone (90), which could sensitize MRP7-overexpressing resistant cells to substrate anticancer drugs. We also included several drugs that does not show significant interaction with MRP7 such as cAMP (16), siphonellinol D (94), glucuronic acid (16), WHIP-154, SN-38, 6-MP, 6-TG, 5-FU (89), probenecid (16) and methotrexate (13). Thus, it is particularly interesting to investigate the interactions between MRP7 and those drugs. Figure 8A showed the docking results of known MRP7 substrates, inhibitors and those do not interact with MRP7. The results indicated that our model could reasonably distinguish MRP7 modulators (substrates/inhibitors) and non-modulators since the modulators (red and blue) have significantly stronger predicted affinity than non-modulators (grey).

As mentioned above, it would be important to understand the interaction between MRP7 and its modulators. Thus, we first analyzed the docking site by clustering all docked ligands. Four separate binding clefts were predicted via $EPOS^{BP}$ software using

the docked ligands and predicted binding sites. Mean hydrophobicity was calculated based on the residue properties (Figure 8B). The best docking poses of substrates and inhibitors formed two clusters which was roughly separated by the Leu549. As shown in Figure 8, MRP7 substrates (Figure 8D) tends to bind at the hydrophilic side (yellow cluster in Figure 8D) surrounded by Gly299, Gln341, Glu400, Gln407, Leu494, Arg545, Pro550, Asn552, Asn553, Arg985, Asp1152, Thr1195, Gln1156 and Gly1196. The exceptions were LTC_4 and doxorubicin, which have higher binding affinity in different sites. For LTC_4, the binding pattern is consistent with its bipartite characteristic. The polar GSH moiety was stabilized by hydrogen bonds formed with Arg545, Asn552, Asn553 and Arg985; while the hydrophobic tail was stabilized by non-polar interactions with Leu298, Pro303, Leu1192 and Gly1196 (data not shown). The binding pattern of LTC_4 with our homology model is similar to that in bovine MRP1, where LTC_4 was also stabilized in a bipartite pockets (PDB ID: 5UJA). After summarizing the docked ligands, we proposed the key amino acids of the binding pocket displayed in Figure 8C. These key residues played crucial rules in stabilizing multiple ligands. For example, Lys292 was responsible for forming hydrogen bonds with docetaxel, doxorubicin, vinorelbine, vincristine, $E_2$17bG and cepharanthine; Leu549 was involved in stabilizing all docked ligands via hydrophobic interactions. Additionally, we found that MRP7 inhibitors tend to occupy the hydrophobic cleft (Figure 8E). Among the modulators we analyzed, cepharanthine, an herbal extract from *Stephania cepharantha*, unlike other modulators, binds at the polar site. This could be explained by the similarity in the chemical structures of cepharanthine as *Vinca* alkaloid, such as vincristine, which also binds to the polar site.

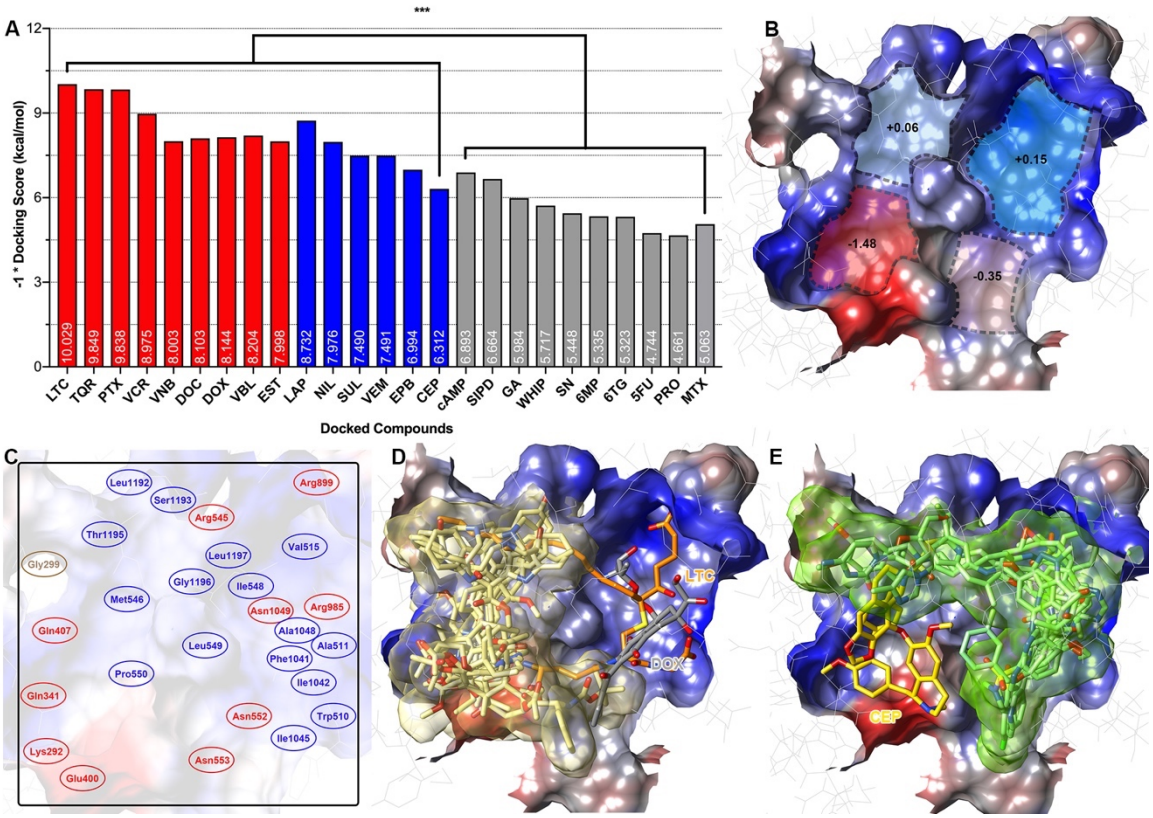

Figure 8. Functional validation of the MRP7 homology model by docking with experimentally validated drugs. A) Docking scores of substrates/inhibitors/non-modulators. Red columns indicate known MRP7 substrates; blue columns indicate known MRP7 inhibitors; grey columns indicate drugs that are not interacting with MRP7. *** $p < 0.005$ via one way ANOVA by comparing substrates/inhibitors and negative drugs. Docking scores × (-1) were labeled within columns. B) Properties of predicted MRP7 binding pocket. Blue indicates hydrophobic and red indicates polar. Numbers indicate mean hydrophobicity of predicted binding clefts. C) Key residues of predicted binding pocket were labeled. Red indicates polar amino acid, blue indicates hydrophobic amino acids. Glycine is colored yellow. D) Docked poses of MRP7 substrates in the binding pocket. LTC_4 and doxorubicin bind to different positions as other substrates. LTC_4 was colored orange; doxorubicin was colored grey. E) Docked poses of MRP7 inhibitors

(displayed as green sticks) in the binding pocket. Inhibitor cepharanthine was colored yellow. MRP7 protein surfaces were colored by electrostatic potential (red: negative; blue: positive). Abbreviations: LTC: LTC_4; TQR: tariquidar; PTX: paclitaxel; VCR: vincristine; VNB: vinorelbine; DOC: docetaxel; DOX: doxorubicin; VBL: vinblastine; EST: $E_2$17bG; LAP: lapatinib; NIL: nilotinib; SUL: sulfinpyrazone; VEM: vemurafenib; EPB: epothilone B; CEP: cepharanthine; SIPD: siphonellinol D; GA: glucuronic acid; WHIP: WHIP-154; SN: SN-38; PRO: probenecid; MTX: methotrexate.

Comparative analysis with bovine MRP1

Next, we performed a series of docking simulations to compare the ligand-binding patterns of MRP7 and MRP1. Multiple anticancer drugs have been identified as MRP1 substrates (such as vincristine and methotrexate) or inhibitors (such as probenecid and MK571). Previous studies have demonstrated that methotrexate is a substrate of MRP1 but not MRP7 (13,95). Similarly, paclitaxel is a good substrate of MRP7 but it cannot be transported by MRP1 (13,96). In this section, we firstly performed docking analysis using LTC_4-bound bovine MRP1 structure. Results were shown in Figure 9. In Figure 9A, we found that the drug binding pocket of MRP1 was also buried in TMDs. Details of the binding pocket were given in Figure 9C. Different from MRP7, MRP1 has a relatively smaller binding pockets with volume of around 743 $Å^3$. Figure 9B showed the results of docking simulations using known MRP1 substrates/inhibitors and non-modulators. The results are consistent with previous *in vitro* studies, with substrates and inhibitors showing higher scores than non-substrate paclitaxel.

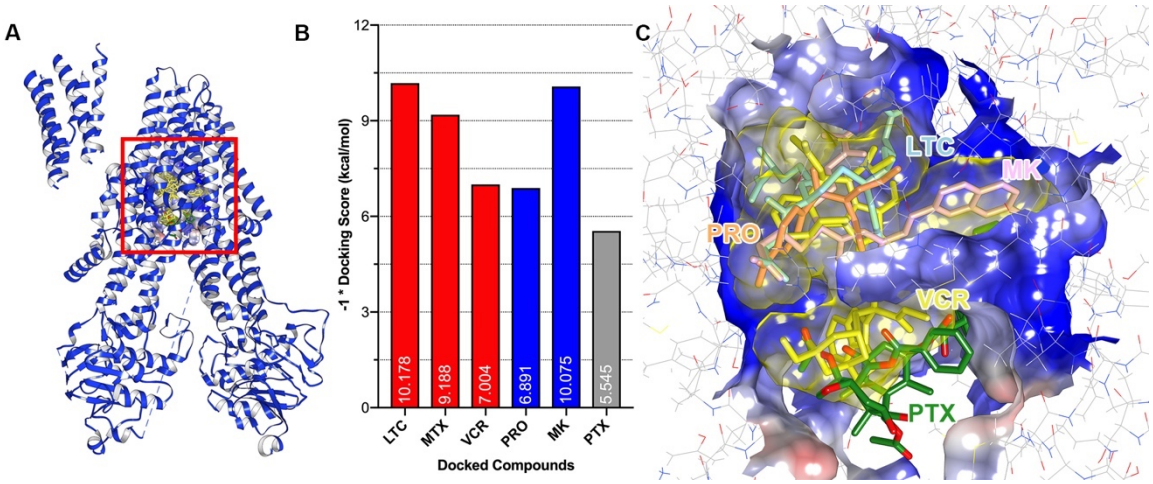

Figure 9. MRP1-substrate anticancer drugs and modulators docked into MRP1 binding pocket. A) Overview of the bovine MRP1 substrate binding pocket. B) Docking scores of known MRP1 substrates, inhibitors and negative control drugs. Docking scores × (-1) were labeled within columns. Column colors indicate different types (red: substrates; blue: inhibitors; grey: negative drugs). Abbreviations: LTC: LTC_4; PTX: paclitaxel; VCR: vincristine; MTX: methotrexate; PRO: probenecid; MK: MK571. C) Docked poses of MRP1 substrates LTC_4, vincristine, modulators probenecid, MK571 (yellow sticks). Non-substrate paclitaxel was displayed as green sticks. All surfaces were colored by electrostatic potential (red: negative; blue: positive).

From Figure 9C, we found that the best docked pose of paclitaxel was actually on the edge of the pocket and close to the open end form by TMDs of MRP1. Detailed docking complex was shown in Figure 10C and 7D. For MRP7, the paclitaxel was stabilized by both polar and hydrophobic interactions. From Figure 10B, we could see that 4 hydrogen bonds were formed between paclitaxel and Glu400, Gln407, Asn553, Gln1156. The benzene rings were stabilized via hydrophobic interactions with Ala334/338, Gly333/337, Gly1196 and Leu1197. For MRP1, in Figure 10D, we could

see that paclitaxel was stabilized via two hydrogen bonds with Gln1088 and Tyr440. No strong hydrophobic interaction in MRP1 was observed to stabilize the molecule. Thus, it is reasonable that paclitaxel has weak or no interaction with MRP1 in actual biological systems.

The predicted binding poses of methotrexate in MRP1/MRP7 binding pockets were shown in Figure 10. In Figure 10E and 7F, the best docking poses of methotrexate locates majorly in the two hydrophobic clefts of MRP7, thus less likely to form hydrogen bonds with polar residues to stabilize the carboxyl groups as in MRP1 (Figure 10G and 7H). According to the cryo-EM structure of bovine MRP1, its binding pocket is actually composed of a "P-pocket" (polar, formed majorly by Lys332, His335, Leu381, Arg1196, Arg1248, Asn1244 and aromatic residues Phe594, Tyr440, Phe385) and an "H-pocket" (hydrophobic, formed majorly by Trp1245, Trp553, Met1092, Thr550 and aromatic residue Tyr1242) based on the binding pattern of LTC_4 (10). Our docking results of methotrexate stays consistent with the proposed MRP1 binding pocket. Similar to LTC_4, methotrexate was stabilized by both polar and hydrophobic interactions. The carboxyl groups formed 3 hydrogen bonds with a salt bridge with Arg1196. Moreover, Trp1245 formed a pi-pi stacking interaction with the ring structure of methotrexate. Although several studies have confirmed methotrexate being a good substrate of MRP1 but not MRP7, we validated such conclusion in this study to further demonstrate the reliability of our homology model.

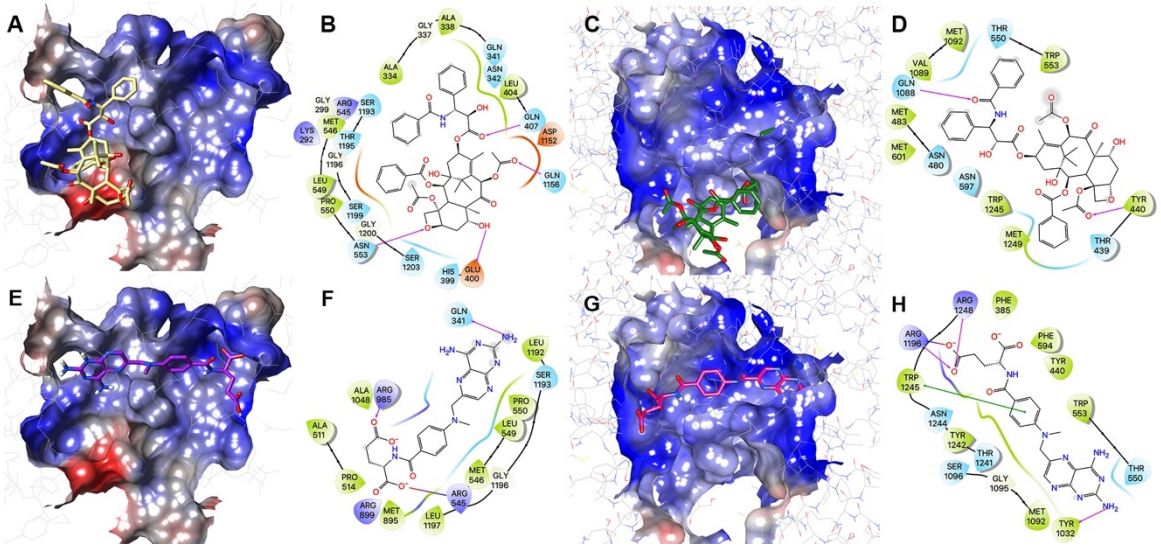

Figure 10. Paclitaxel/methotrexate docked with MRP7 and MRP1 binding pockets. A) Paclitaxel docked with the MRP7 binding pocket. Protein surface was colored by electrostatic potential. Paclitaxel was displayed as yellow sticks. B) 2-D diagram of paclitaxel-MRP7 interactions. Amino acids within 3 Å to paclitaxel were displayed as colored bubbles (cyan: polar; green: hydrophobic; red: negatively charged; blue: positively charged). Purple lines with arrow indicate hydrogen bonds. Grey circles indicate solvent exposure. C) Paclitaxel docked with the MRP1 binding pocket. D) 2-D diagram of paclitaxel-MRP1 interactions. E) Methotrexate docked with the MRP7 binding pocket. Protein surface was colored by electrostatic potential. Methotrexate was displayed as purple sticks. F) 2-D diagram of methotrexate-MRP7 interactions. G) Methotrexate docked with the MRP1 binding pocket. Methotrexate was displayed as magenta sticks H) 2-D diagram of methotrexate-MRP1 interactions. Purple solid lines with arrow indicate hydrogen bonds. Purple solid line without arrow indicates salt bridge. Green solid line without arrow indicates pi-pi interaction.

1.4 Discussion

Since functional modulation of the ABC transporters is considered a major solution in overcoming MDR in cancers (97), understanding the structure-function relationship is thus important in the development of novel ABC transporters modulators. Moreover, information in drug binding and recognition based on structural analysis is necessary in the discovery of potential ABC transporters substrates (98,99) which will provide valuable references for clinicians.

Considering the lack of MRP7 crystal structure, we constructed two conformations of human MRP7 models using homology modeling tools and equilibrated by a 100 ns MD run. Subsequently, the structural dynamics was analyzed based on the MD simulation, where we found that linker structures, especially linker 1 and linker 2, were the major contributors to the overall structural deviation. In the most recent crystal structures of ABC transporters these linker domains were unable to fully determined by crystallography (10,67,101), which is collaborated with the flexibility of these particular regions in our MD run.

The structure of the longest linker 2 which connects TMD2 and NBD1, often lacks accurate 3D structure in ABC transporter crystal structures. In this study, we constructed *de novo* linker structure and evaluated the role it plays in the structural dynamics in MRP7 via RMSD and RMSF analysis. Our results indicated that the linker structure stabilized the protein structure by connecting the two functional complex (TMD1-NBD1 and TMD2-NBD2) as a "spring" in order to maintain the protein structure and transmit domain motions. Similarly, in other ABC transporter structures such as ABCB1, the linker structure also lacks accurate crystal structure (102). The linker structure of ABCB1 was found by a homology modeling and MD simulation study to

stabilize the transporter in membrane system (103). The MD results in Figure 5A that TMD2 and NBD1 having higher equilibrated RMSD could be explained by direct connection with linker 2. The fluctuation of linker 2 will be transmitted to domains that are directly linked more easily. And with the distance to linker 2 increases, its influence in structural stability will become attenuated.

Being an ATP-dependent efflux pump, analysis of the potential motion pattern of MRP7 will boost the understanding of the transportation mechanism. The PCA analysis revealed the potential motions of MRP7 at substrate-binding or ATP-binding states. Several studies on other ABC transporters have described essential mechanism of action related to the NBD dimerization after substrates and ATP-binding (67,102,104). For MRP1, the cryo-EM structures of inward- and outward-facing indicate that the ATP-binding induces NBD closure which consequently triggers helices rotation and side chain movement as well as decreased substrate affinity (67).

Subsequently, we performed binding site search as well as docking analysis to characterize the binding pockets of MRP7, where the major drug binding pocket buried in TMDs was focused. The binding pockets of MRP1 and MRP7 were also compared and analyzed. Unlike ABCB1, where the binding sites are characterized by a large number of aromatic (M site) and polar (R/H site) residues (105), and ABCG2, where the binding sites are majorly composed of hydrophobic residues (53), both MRP7 and MRP1 showed bipartite binding pockets with the existence of both polar and non-polar region. Although sharing the similar components, MRP7 and MRP1 still have different substrate/inhibitor spectrum, for example, multiple studies have shown that MRP1 is not able to mediate the transportation of paclitaxel (106,107) which is a substrate of MRP7 (108). Or the case of

methotrexate, which is a substrate of MRP1 but not MRP7. Such difference could be explained by the characteristics of the pockets such as volume and hydrophobicity. We found that paclitaxel had lower binding affinity to MRP1 is possibly due to the size of the pocket and distribution of polar residues. As a result, paclitaxel could only find the best docking site on the edge of the pocket, which has polar residues and larger volume. It is worth noting that although the different physiochemical properties of amino acids which form the binding pocket of MRP7 and MRP1 are one of the key factors that determined the transport pattern of paclitaxel, paclitaxel sensitivity is also determined by other intracellular macro-factors as well as metabolism pathways.

Investigations of the transport properties of MRP7 revealed its ability to efflux conjugates such as $E_2$17βG and LTC_4, indicating the existence of bipartite substrate binding pocket for anionic and hydrophobic moieties. In this study, we identified 4 potential binding clefts with different hydrophobicity in MRP7 binding pockets, which were separated by a leucine in the center. The docking analysis of several previously validated MRP7 substrates provided more details of the binding pocket. More docking analysis was performed using more MRP7 substrates and modulators, from which we further confirmed the existence of binding clefts. Additionally, we found that MRP7 modulators tend to occupy the hydrophobic cleft while substrates tend to occupy the polar cleft. Among the modulators we analyzed, cepharanthine, an herbal extract from *Stephania cepharantha*, unlike other modulators, binds at the polar site. This could be explained by the similarity in the chemical structures of cepharanthine as *Vinca* alkaloid, such as vincristine, which also binds to the polar site.

In summary, we performed a series of structure-function analysis using MD simulations and docking on homology models built from MRP1 crystal structures. Our findings provide new and valuable information for better understanding the structural dynamics and transport mechanism of human MRP7, as well as the potential drug-binding sites within the TMDs of MRP7. Our model was also validated by docking analysis using known MRP7 substrates and inhibitors, as well as non-modulators. This MRP7 model could be a good starting point for future MRP7 studies regarding amino acid mutations in cancer patients to evaluate potential alterations of substrates/inhibitors binding pattern and pharmacokinetics. Moreover, our model would theoretically enable the development of MRP7 modulators as well as high-throughput virtual screening.

CHAPTER 2

The homology model of human MRP7 protein is critical in developing and understanding MRP7-mediated MDR in cancer cells. In this chapter, we majorly focused on the discovery of two synthesized compounds as potent MRP7 modulators where the homology model of human MRP7 was used in the docking simulations.

2.1 Introduction

Previously, a series of 1,2,3-triazole-pyrimidine hybrids and were synthesized. Among them, the compound CMP25 showed potent reversal activity against P-glycoprotein (P-gp/ABCB1)-mediated MDR, which is 7-fold more potent than verapamil (109). Additionally, in a previously synthesized series of 5-cyano-6-phenylpyrimidin derivatives, a compound named CP55 showed potent reversal activity against ABCB1-mediated MDR *in vitro* and in mouse xenograft models (110). However, their interactions with MRP7 was not tested. In this chapter, we investigated the characteristics of CMP25 and CP55 to reverse MRP7-mediated MDR. We found that both CMP25 and CP55 could significantly increase the cellular sensitivity to MRP7 substrates in MRP7-overexpressing cells by increasing the intracellular accumulation of MRP7-substrate chemotherapeutic drugs *in vitro*.

2.2 Materials and methods

Materials

The 5-cyano-6-phenylpyrimidin derivative CP55 and 1,2,3-triazole-pyrimidine hybrids CMP25 were synthesized as previously described (110). Cell culture: Dulbecco's

modified Eagle's Medium (DMEM), fetal bovine serum (FBS), penicillin/streptomycin and trypsin were purchased from Hyclone (Pittsburgh, PA).

Cell lines and cell culture

In this study we used HEK293/pcDNA3.1 and MRP7-transfected HEK293/MRP7 cells. HEK293pcDNA3.1 and HEK293/MRP7 was established by transfecting empty vector pcDNA3.1 or MRP7-expressing recombinant vector as previously described (100). Cells were maintained and cultured in DMEM with 10% FBS, 100 units/mL penicillin/streptomycin and 2 mg/mL G418. At least one week prior to experiment, we transfer cells to DMEM without G418.

Cytotoxicity assay

Cytotoxicity of CMP25 and CP55 in HEK293/pcDNA3.1 and HEK293/MRP7 cells was evaluated using MTT colorimetric assay as previously described (111). To be brief, the HEK293/pcDNA3.1 and HEK293/MRP7 cells were seeded in 96-well plates at 5,000-7,000 cells per well. Cells were cultured overnight before addition of 0 – 100 μM CMP25 and CP55 for toxicity assay. Different concentrations of MRP7 modulators cepharanthine or CMP25 and CP55 were preincubated with cells for 2 h before different concentrations of paclitaxel/vincristine/vinblastine/cisplatin were added, after which plates were cultured for 68 h. Then MTT was added to each well to a final concentration of 0.4 mg/ml and incubated for additional 4 h (72 h in total). Then medium was removed, and the formazan crystal was dissolved in DMSO. Absorbance at 570 nm was determined by a spectrophotometer. IC_{50} was calculated using modified Bliss method (112). Resistance fold (RF) was the ratio of IC_{50} in HEK293/MRP7 and HEK293/pcDNA3.1

cells. Cepharanthine was used as a positive reversal agent of MRP7. Cisplatin, a non-substrate of MRP7, was used as a negative control drug.

Western blotting

Western blotting was performed as previously described with modifications (113). Briefly, HEK293/pcDNA3.1 and HEK293/MRP7 cells were seeded in T-25 flasks with equal amount. For concentration-dependent study, CMP25 or CP55 was added to cells in different concentrations (1 or 3 μM) and incubated for 72 h. For time-dependent study, cells were incubated with the same concentration (3 μM) of CMP25 or CP55 for 0/24/48/72 h. On the day of cell lysis, cells were first rinsed with ice-cold PBS twice before adding lysis buffer. Cells were scraped down from flasks and lysates were incubated for 30 min on ice. Then cell lysate was centrifuged at 12,000 rpm at 4 °C for 20 min. Supernatant was collected for further analysis. Protein concentration was determined by bicinchoninic-acid-based protein assay (BCA). Subsequently, equal amount of total protein (20-30 μg) was separated by SDS-PAGE (sodium dodecyl sulfate polyacrylamide gel electrophoresis) and transferred onto PVDF (polyvinylidene difluoride) membranes. The membranes were incubated in blocking solution (5% skim milk in TBST) at room temperature for 2 h, followed by incubation with anti-MRP7 (1:1000) and anti-GAPDH (1:1000) primary antibody at 4 °C overnight. Afterwards, membranes were rinsed with TBST and incubated with HRP-conjugated secondary antibody (1:1000) at room temperature for 2 h. MRP7 and GAPDH protein was detected using enhanced photodope TM-HRP detection kit (Cell Signaling Technology) and exposed to films. The resulting protein bands were analyzed by grayscale value using Image J.

Immunofluorescence assay

Immunofluorescence was performed following the protocol described previously with slight modifications (114). Cells (1×10^5 per well) were seeded into 6-well plates. In order to prevent cells from detaching, poly-lysine-processed cover slips were set at the bottom of each well. For time-dependent study, cells were treated for 0/24/48/72 hours with 3 μM CMP25 or CP55; for concentration-dependent study, cells were treated 72 hours with 1 or 3 μM CMP25 or CP55. Next, cells were fixed with 4% formaldehyde in 37 °C for 15 min. Then 0.1% Triton X-100 was added for permeabilization and then 6% BSA for blocking for 2 h in 37 °C. Subsequently, cells were incubated with MRP7 monoclonal antibody (1:1000) at 4 °C overnight followed by incubation with Alexa Fluor 594 conjugated secondary antibody (1:1000) for 1 h at 37 °C. PI (propidium iodide) was used to dye the nuclei. Before imaging, cover slips were transferred to a microslide and mounted with glycerol. Images were taken using a fluorescence microscope.

[^{3}H]-labeled MRP7 substrate accumulation assay

[^{3}H]-paclitaxel and [^{3}H]-vincristine accumulation were determined as previously described with slight modifications (115).

[^{3}H]-labeled MRP7 substrate efflux assay

Efflux assay was performed as previously described with slight modification (116).

Docking analysis

The CMP25 or CP55 structure was prepared for docking simulation as previously described (77). Human MRP7 homology model bound with paclitaxel was established in

our lab (117). The protein model was inward-facing. Docking calculations were performed in AutoDock Vina (v 1.1.2) (118).

2.3 Results

Cytotoxicity of CMP25/CP55 in HEK293/pcDNA3.1 and HEK293/MRP7 cells

Cytotoxicity assay was performed for two goals: a) compare the cytotoxicity (IC_{50}) of CMP25 or CP55 in parental and MRP7-mediated resistant cells to determine whether CMP25 or CP55 is a potential MRP7 substrate; b) determine the non-toxic concentration (at least 80% cells survive) of CMP25 or CP55 for reversal study. The results of cytotoxicity assay were presented in Figure 11 (CMP25) and 12 (CP55). Results showed that there is no significant difference in the IC_{50}'s of CMP25 or CP55 in parental and MRP7-transfected cells. Therefore, we chose two non-toxic concentrations (1 and 3 μM) for reversal study.

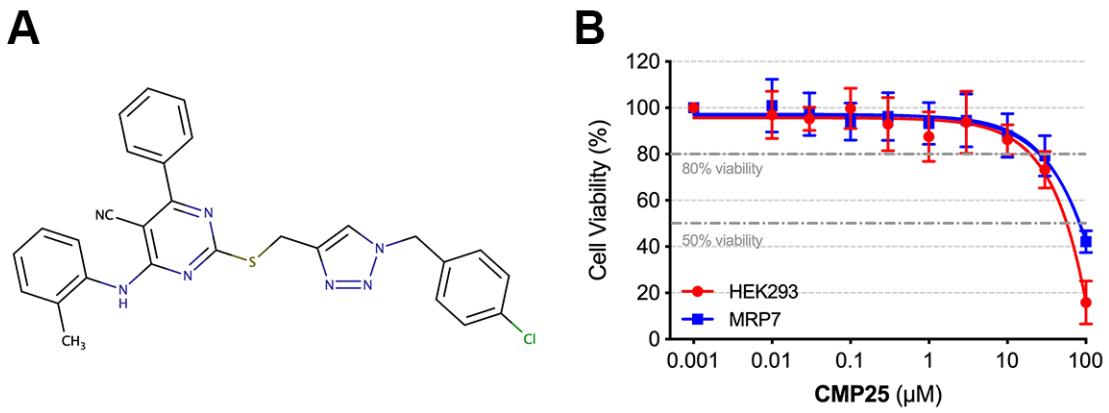

Figure 11. Chemical structure and cytotoxicity of CMP25. A) 2D chemical structure of CMP25. B) Cytotoxicity of CMP25 in HEK293/pcDNA3.1 and MRP7. 80% and 50% cell viability were marked by grey dash lines.

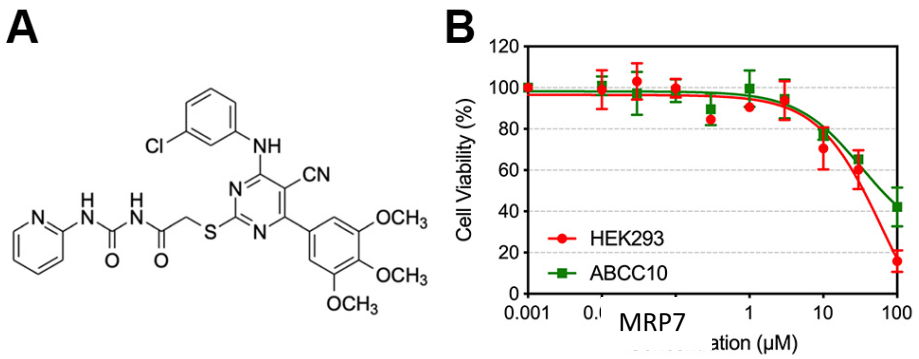

Figure 12. Chemical structure and cytotoxicity of CP55. A) 2D chemical structure of CP55. B) Cytotoxicity of CP55 in HEK293/pcDNA3.1 and HEK293/MRP7 cells.

Reversal effects of CMP25/CP55 in HEK293/MRP7 cells

Results of reversal study were shown in Figure 13 (CMP25) and 14 (CP55). In the reversal study, we used 1 and 3 μM of CMP25/CP55. The results showed that in both concentrations co-treatment with CMP25/CP55 significantly decreased the IC_{50} of MRP7-substrate antineoplastic drugs, while 3 μM of CMP25/CP55 showed stronger reversal effects than lower concentration. Results in Figure 13 and 14 showed that the HEK293/MRP7 concentration-viability curves of paclitaxel, vincristine and vinblastine shifted left when co-administered with CMP25/CP55 or cepharanthine compared with control group. For parental HEK293/pcDNA3.1 cell, no significant change was observed with CMP25/CP55 or cepharanthine. For cisplatin, which is not a substrate of MRP7, both MRP7-transfected and parental cells showed similar concentration-viability curves with similar IC_{50}.

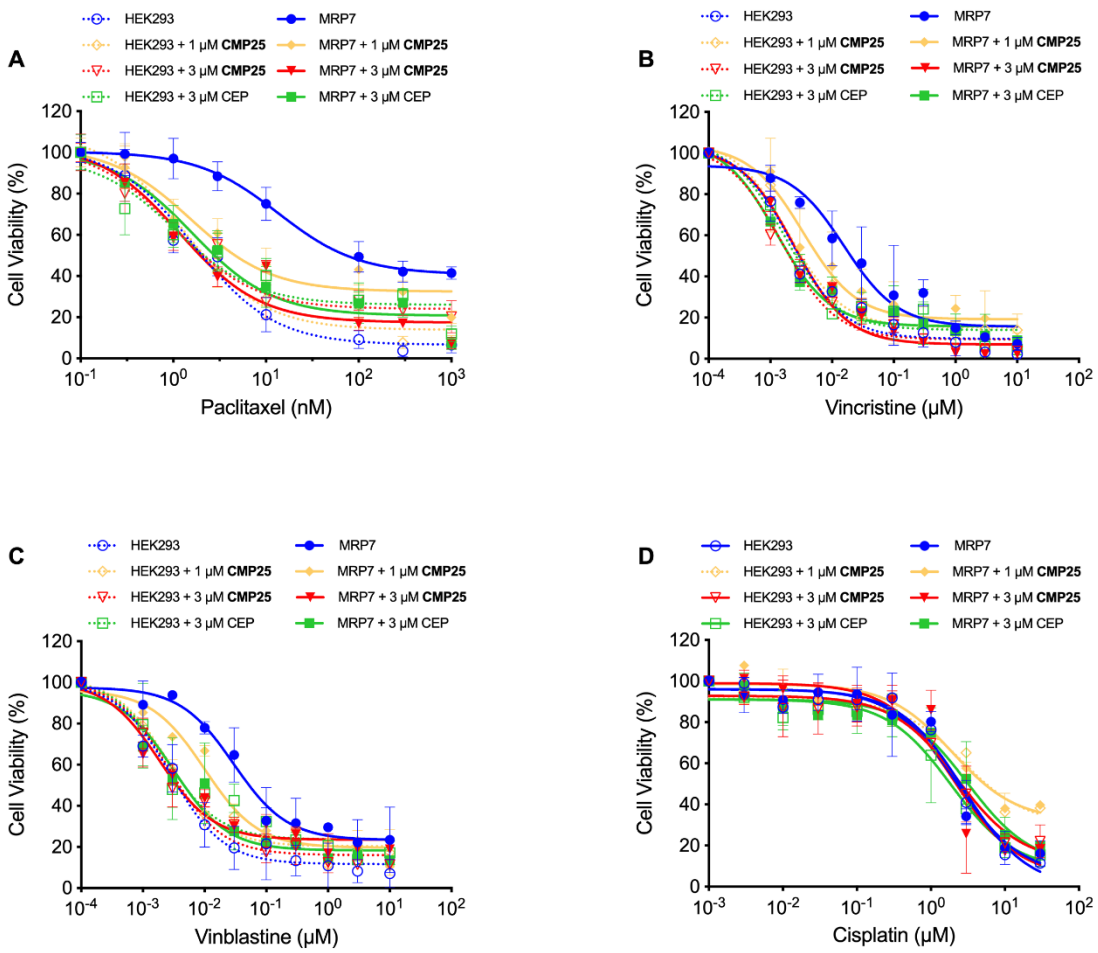

Figure 13. Reversal effects of CMP25 in MRP7-overexpressing cells. Concentration-viability curves of A) paclitaxel; B) vincristine; C) vinblastine; D) cisplatin. Results of parental cells HEK293/pcDNA3.1 were displayed as dash lines; HEK293/MRP7 were displayed as solid lines. Results were expressed as mean ± SD, representative of three independent experiments in triplicate.

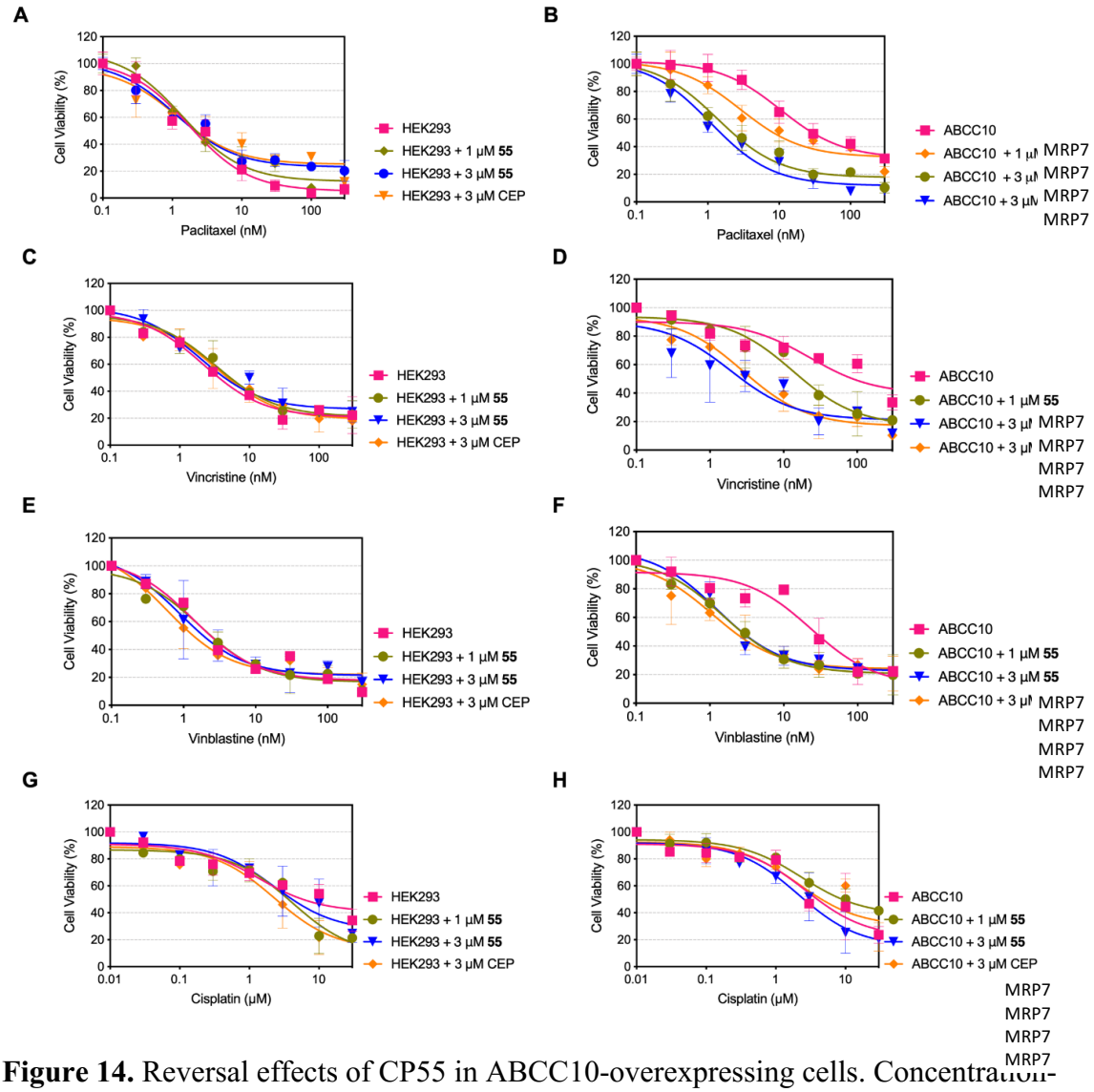

Figure 14. Reversal effects of CP55 in ABCC10-overexpressing cells. Concentration-viability curves of A-B) paclitaxel; C-D) vincristine; E-F) vinblastine; G-H) cisplatin. Results of parental cells HEK293/pcDNA3.1 were displayed in A, C, E and G; HEK293/ABCC10 were displayed in B, D, F and H. Data are expressed as mean ± SD, representative of three independent experiments in triplicate.

The effect of CMP25/CP55 on MRP7 protein expression

To verify whether the reversal effects was due to regulated MRP7 protein expression in HEK293/MRP7 cells, we treated both parental and resistant cells with CMP25/CP55 and determined the protein expression level via Western blot. First, we verified the expression of MRP7 in transfected cells. Specifically, cells were treated with a) 1 or 3 μM CMP25/CP55 for 72 h or b) 3 μM CMP25/CP55 for 0, 24, 48 or 72 h. Figure 15 and 16 confirmed the expression of MRP7 protein in transfected HEK293/MRP7 cells and no MRP7 was detected in parental HEK293/pcDNA3.1 cell. Figure 15 and 16 showed that treatment with CMP25/CP55 did not significantly alter the protein expression level of MRP7. Thus, we drew the conclusion that the reversal effects on MRP7 was not due to regulating the expression level of MRP7 protein.

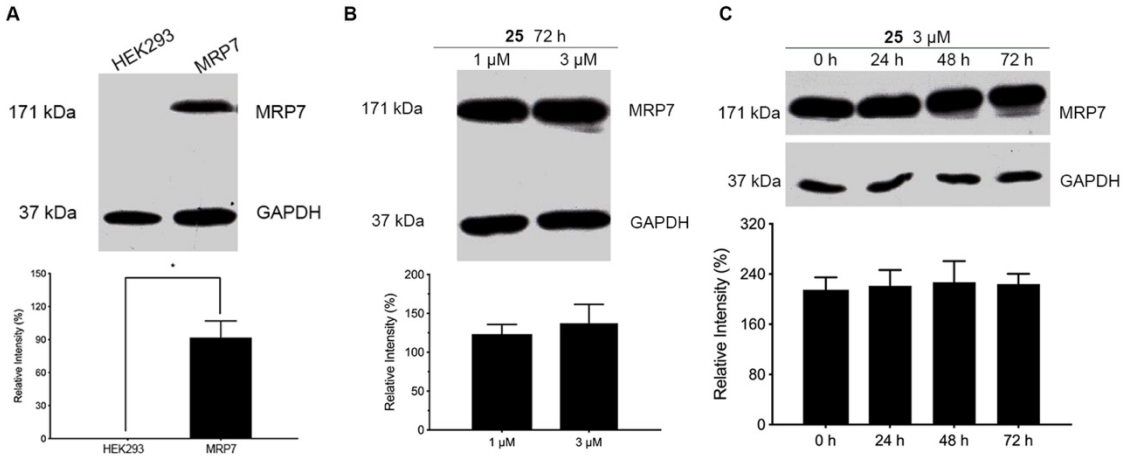

Figure 15. Effect of CMP25 on the MRP7 protein expression. (A) MRP7 expression in HEK293/pcDNA3.1 and HEK293/MRP7 cells. GAPDH was used as a loading control. (B) HEK293/MRP7 cells treated with 1 or 3 μM CMP25 for 72 h. (C) HEK293/MRP7 cells treated with 3 μM CMP25 for 0/24/48/72 h. Columns with error bars represent mean ± SD from 3 independent triplicate experiments. Asterisks (*) indicate $p < 0.05$ versus parental group (HEK293/pcDNA3.1).

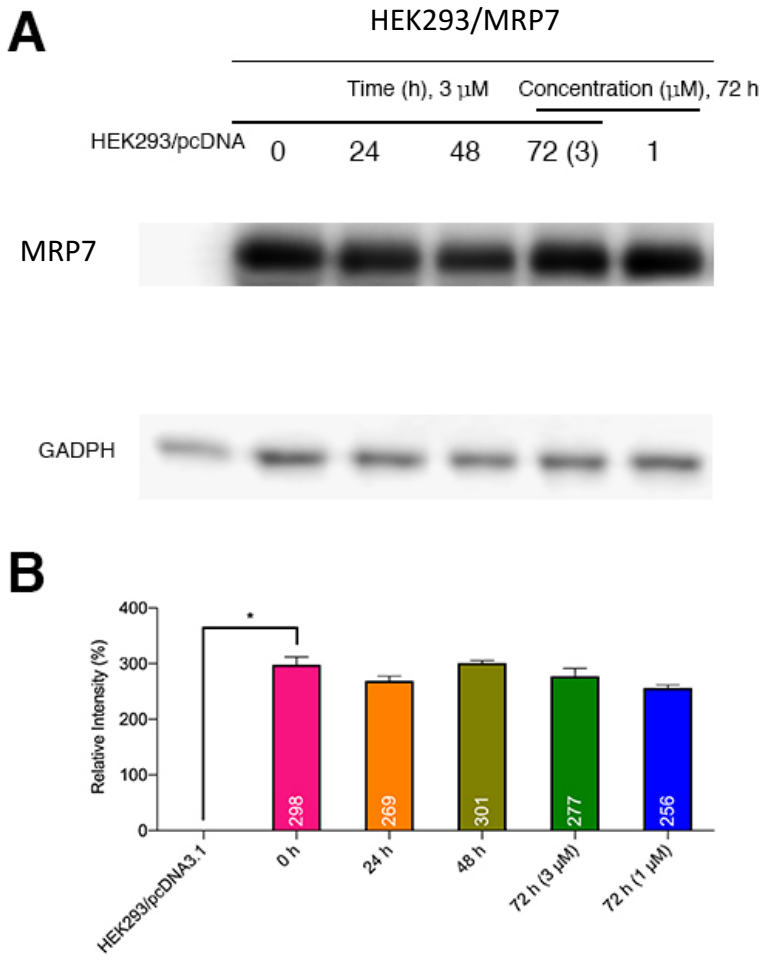

Figure 16. Effect of CP55 on the MRP7 protein expression. (A) MRP7 expression in HEK293/pcDNA3.1 and HEK293/MRP7 cells. GAPDH was used as a loading control. (B) Protein expression quantification. Columns with error bars represent mean ± SD from 3 independent triplicate experiments. Asteroid (*) indicate $p < 0.05$ versus parental group (HEK293/pcDNA3.1).

The effect of CMP25/CP55 on the intracellular accumulation of MRP7-substrate anticancer drugs

The above results demonstrated the reversal effect of CMP25/CP55 in HEK293/MRP7 cells, and such effect was not due to altered protein expression level. To

obtain more insight into the mechanism of action, intracellular MRP7 substrate accumulation was measured in parental and MRP7-overexpressing cell lines. As shown in Figure 17 and 18, CMP25/CP55 significantly increased the intracellular accumulation of [^{3}H]-paclitaxel in HEK293/MRP7 cells, without significant changes in parental HEK293/pcDNA3.1 cell. The intracellular accumulation in HEK293/MRP7 cells treated by CMP25/CP55 is comparable to that treated with positive modulator cepharanthine. Similar results were also observed in the accumulation of [^{3}H]-vincristine. Resistant cells treated with CMP25/CP55 showed higher intracellular accumulation level when comparing to control group without modulators.

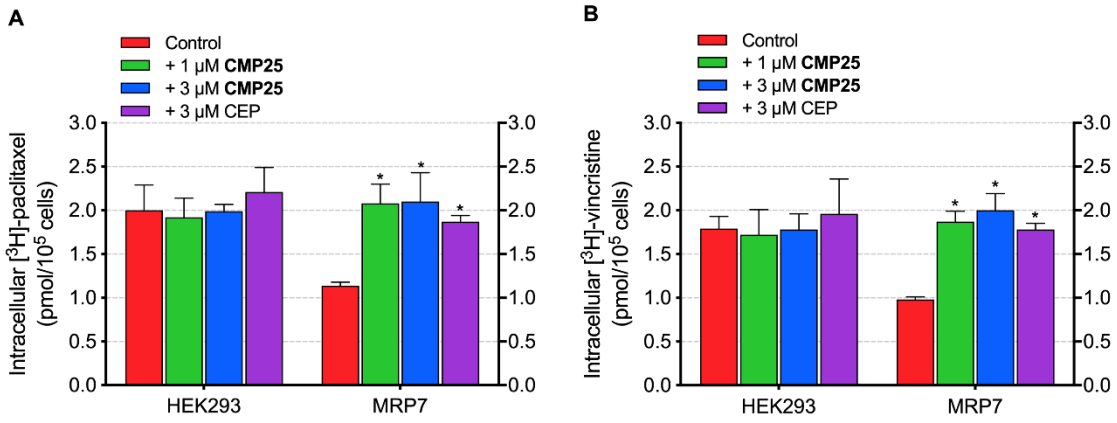

Figure 17. Effect of CMP25 on the intracellular accumulation of [^{3}H]-paclitaxel and [^{3}H]-vincristine in parental and MRP7-transfected cells. (A) Effect of CMP25 on [^{3}H]-paclitaxel accumulation in HEK293/pcDNA3.1 and HEK293/MRP7 cells. (B) Effect of CMP25 on [^{3}H]-vincristine accumulation in HEK293/pcDNA3.1 and HEK293/MRP7 cells. Columns with error bars represent mean ± SD from three independent duplicate experiments. Asterisks (*) indicate $p < 0.05$ versus control group (untreated resistant cells).

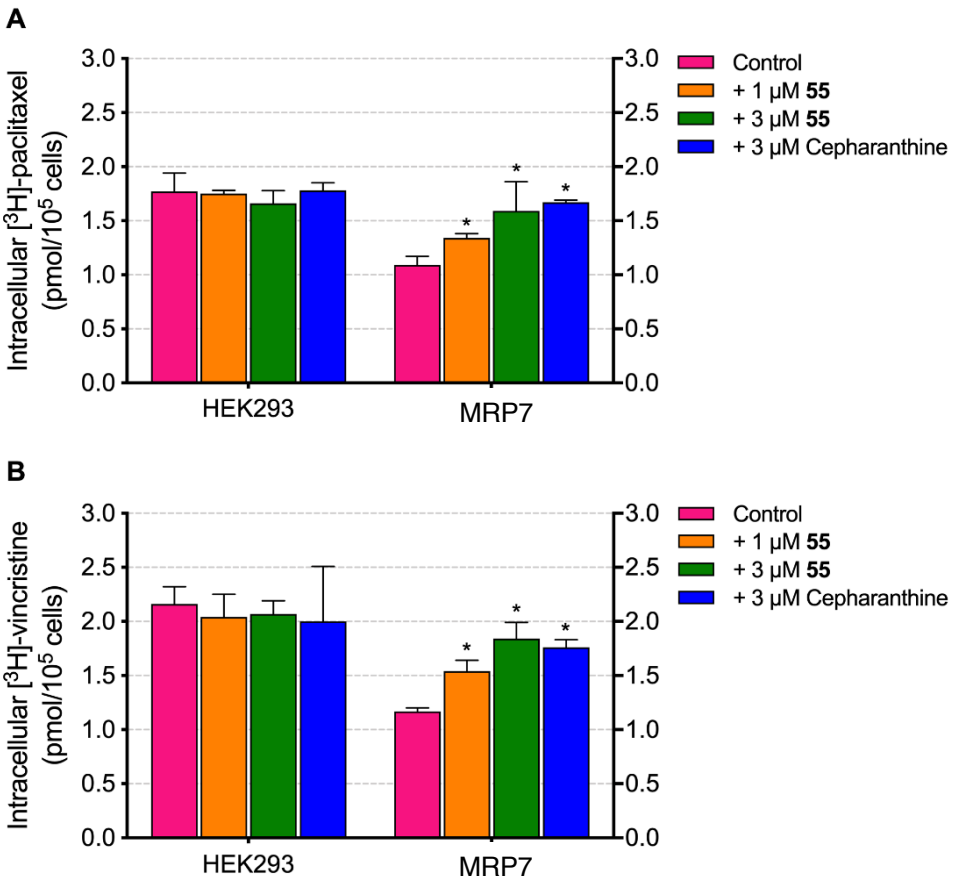

Figure 18. Effect of CP55 on the intracellular accumulation of [^{3}H]-paclitaxel and [^{3}H]-vincristine in parental and MRP7-transfected cells. (A) Effect of CP55 on [^{3}H]-paclitaxel accumulation in HEK293/pcDNA3.1 and HEK293/ MRP7 cells. (A) Effect of CP55 on [^{3}H]-vincristine accumulation in HEK293/pcDNA3.1 and HEK293/ MRP7 cells. Columns with error bars represent mean ± SD from three independent duplicate experiments. Asteroids (*) indicate $p < 0.05$ versus control group (untreated resistant cells).

The effect of CMP25/CP55 on efflux of MRP7-substrate anticancer drugs

To further confirm whether the elevated intracellular accumulation of paclitaxel or vincristine was due to the blockage of the MRP7 efflux function, we observed the

efflux of [^{3}H]-paclitaxel or [^{3}H]-vincristine in parental and resistant cells. In Figure 19 and 20, the remaining intracellular amount of [^{3}H]-paclitaxel or [^{3}H]-vincristine in MRP7-overexpresing cells was significantly lower than that of HEK293/pcDNA3.1 and in the absence of CMP25/CP55. Treatment with 3 μM CMP25/CP55 significantly decreased the efflux of [^{3}H]-paclitaxel or [^{3}H]-vincristine in MRP7-overexpressing cells. Furthermore, the results in HEK293/MRP7 were comparable to that of the positive control inhibitor cepharanthine.

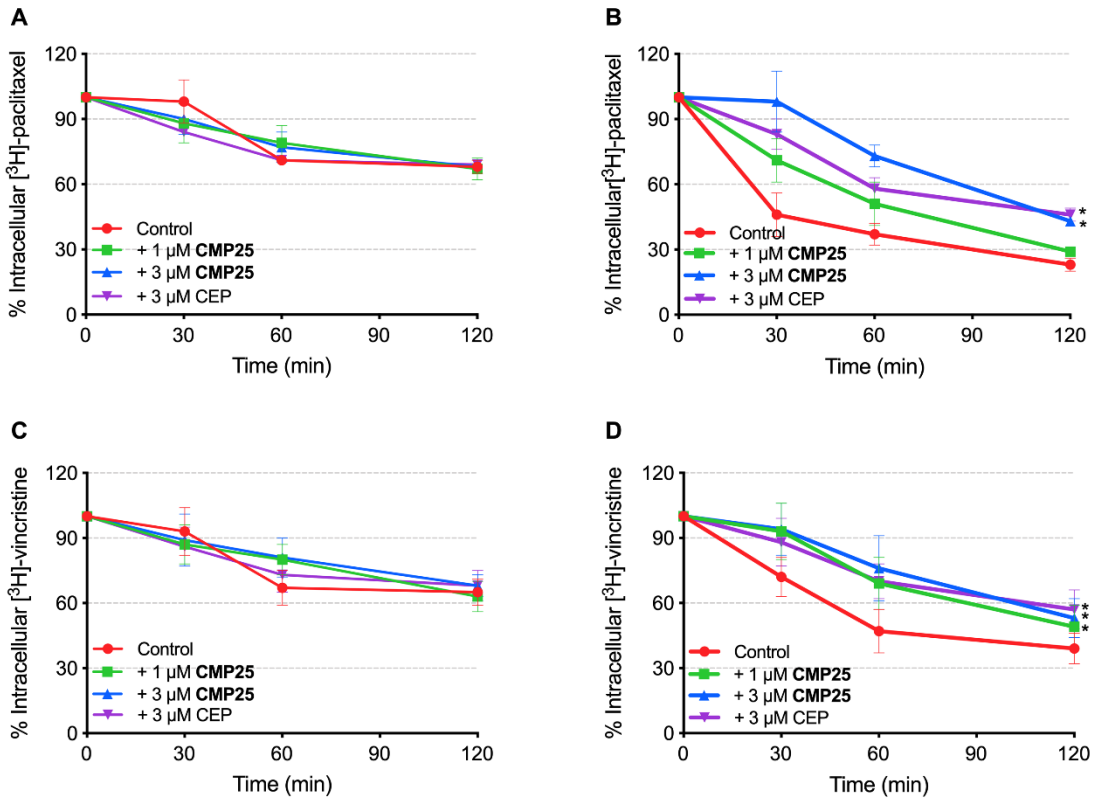

Figure 19. Effects of CMP25 on the efflux of [^{3}H]-paclitaxel and [^{3}H]-vincristine in parental and MRP7-transfected cells. X-axis represents time course (0/30/60/120 min). Y-axis represents the percentage of remaining intracellular of [^{3}H]-paclitaxel or [^{3}H]-vincristine. (A) [^{3}H]-paclitaxel efflux in HEK293/pcDNA3.1, (B) [^{3}H]-paclitaxel efflux in HEK293/MRP7, (C) [^{3}H]-vincristine efflux in HEK293/pcDNA3.1, (D) [^{3}H]-

vincristine efflux in HEK293/MRP7. Points with error bars represent mean ± SD from 3 independent duplicate experiments. Asterisks (*) indicate $p < 0.05$ versus control group (untreated resistant cells).

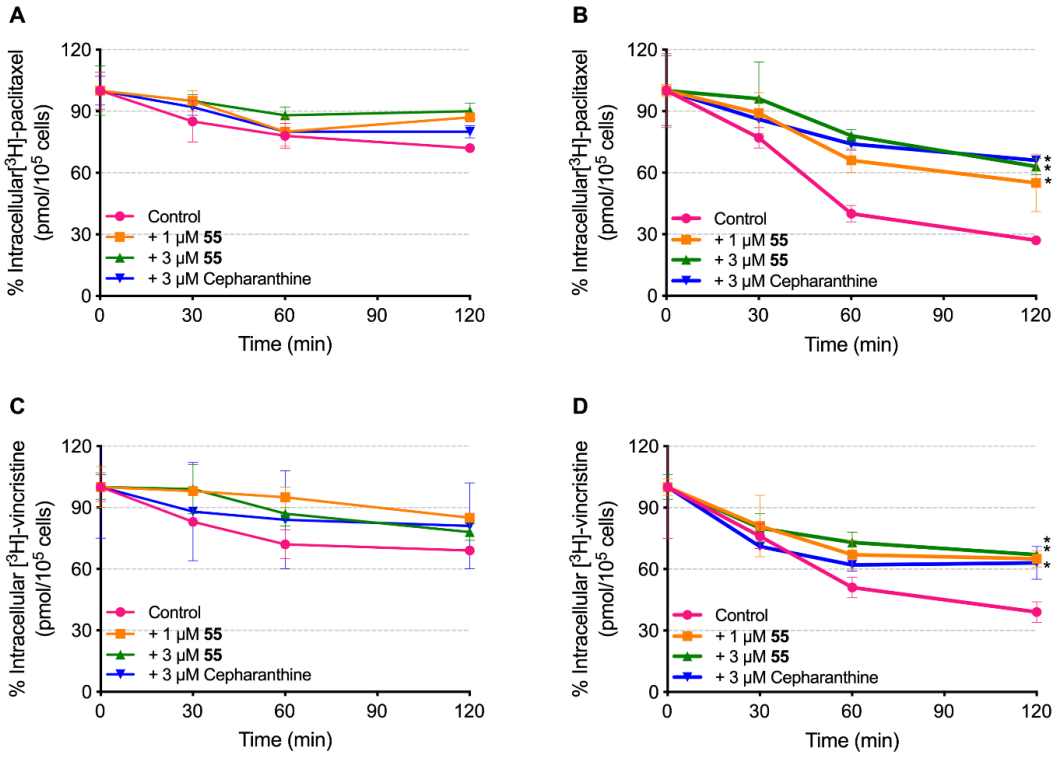

Figure 20. Effects of CP55 on the efflux of [^{3}H]-paclitaxel and [^{3}H]-vincristine in parental and MRP7-transfected cells. Time course versus the percentage of remaining intracellular of [^{3}H]-paclitaxel or [^{3}H]-vincristine was plotted to illustrate the effect of CP55 on [^{3}H]-paclitaxel efflux in (A) HEK293/pcDNA3.1, (B) HEK293/MRP7or [^{3}H]-paclitaxel efflux in (C) HEK293/pcDNA3.1, (D) HEK293/MRP7. Points with error bars represent mean ± SD from 3 independent duplicate experiments. Asterisks (*) indicate $p < 0.05$ versus control group (untreated resistant cells).

The effect of CMP25/CP55 on the subcellular localization of MRP7

Another potential mechanism of the antagonization of CMP25/CP55 on MRP7 is the alteration of sub-cellular localization. Thus, we performed immunofluorescence assay to determine whether CMP25/CP55 could alter the subcellular localization of MRP7 transporters. As shown in Figures 21 and 22, MRP7 located on the membrane of HEK293/MRP7 cells. After incubating for 24, 48, and 72 h, CMP25/CP55 did not significantly alter the localization of MRP7. Incubating with different concentrations of CMP25/CP55 also did not alter the localization of MRP7. Above results indicate CMP25/CP55 did not affect the subcellular localization of MRP7.

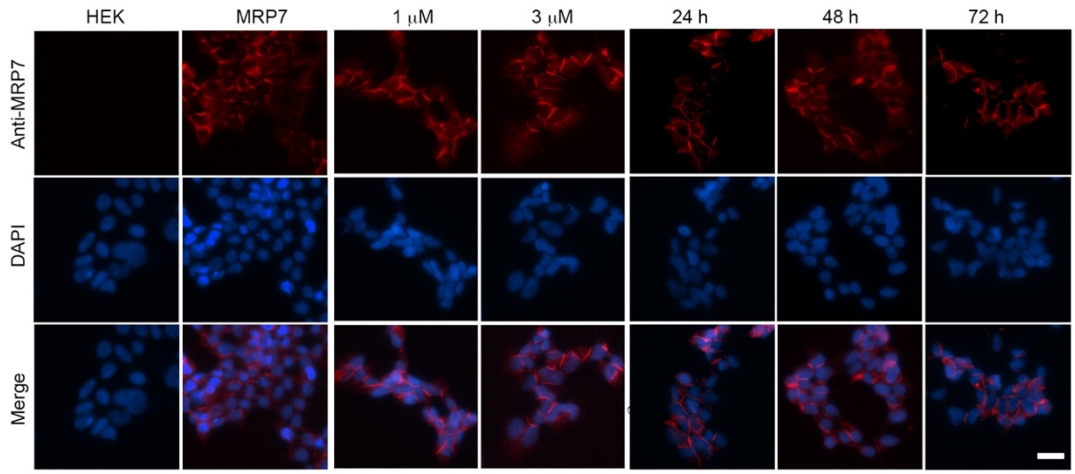

Figure 21. The effect of CMP25 on subcellular localization of MRP7 transporters. Left two columns: the expression and localization of MRP7 expression in HEK293/MRP7 cells (0 h). 3rd and 4th columns: sub-cellular localization of MRP7 expression in HEK293/MRP7 cells incubated with 1 or 3 μM of CMP25 for 72 h. 5th, 6th and 7th columns: Sub-cellular localization of MRP7 expression in HEK293/MRP7 cells incubated with 3 μM of CMP25 for 24, 48, and 72 h. Red: MRP7. Blue: DAPI counterstains the nuclei. Scale bar: 50 μM.

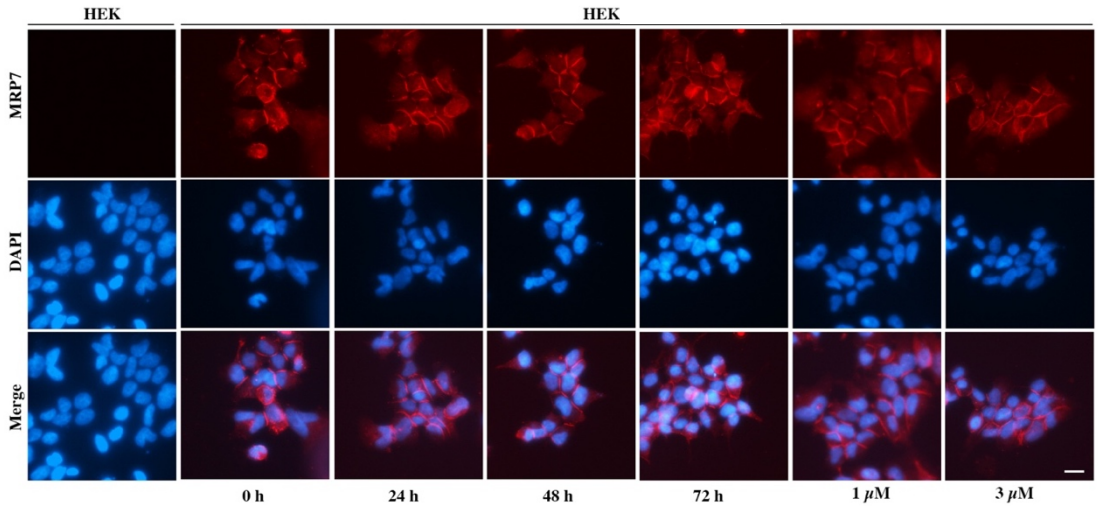

Figure 22. The effect of CP55 on subcellular localization of MRP7 transporters. Sub-cellular localization of MRP7 expression in HEK293/MRP7 cells incubated with 0.5, 1 or 3 μM of CP55 for 72 h; or 3 μM of CP55 for 0, 24, 48, and 72 h. Red: ABCC10. Blue: DAPI counterstains the nuclei. Scale bar: 50 μm.

Molecular docking and molecular dynamics simulation

To better understand the potential interaction between CMP25/CP55 and MRP7 protein, we performed molecular docking simulation and molecular dynamics simulation. Compound CMP25 has a high docking score of -8.974 kcal/mol in the predicted substrate binding pocket of MRP7. The docked complex showed that CMP25 was stabilized by both polar and hydrophobic interactions. The compound CMP25 was stabilized by a hydrogen bond, as well as a π-cation interaction with Arg985. Additionally, CMP25 was stabilized in the hydrophobic pocket formed by Ala542, Met546, Ile548, Leu549, Ile1045, Ala1048 and Asn1049. Docked complex with highest docking score was subjected to a 10 ns molecular dynamics simulation. The results in Figure 23 showed that the structures of both protein and ligand reached equilibrium after the first 5 ns. CMP25

had an overall displacement of 4 Å and MRP7 (protein) was stable with a root mean square deviation (RMSD) of around 6 Å, indicating only small internal fluctuation inside the drug-binding site of the protein. Compound CP55 has a high docking score of -9.023 kcal/mol in the predicted binding pocket of MRP7. The docked complex showed that CP55 was stabilized by both polar and hydrophobic interactions (Figure 24). The compound CP55 was stabilized by hydrogen bonds formed with residue Asn1049 and Leu1192, as well as a salt bridge interaction with Arg545. Additionally, CP55 was stabilized in the hydrophobic pocket formed by Trp510, Ala511, Pro514, Val515, Leu549, Met546, Leu1192, Ser1193, Thr1195, Gly1196, Leu1197 and Gly1200.

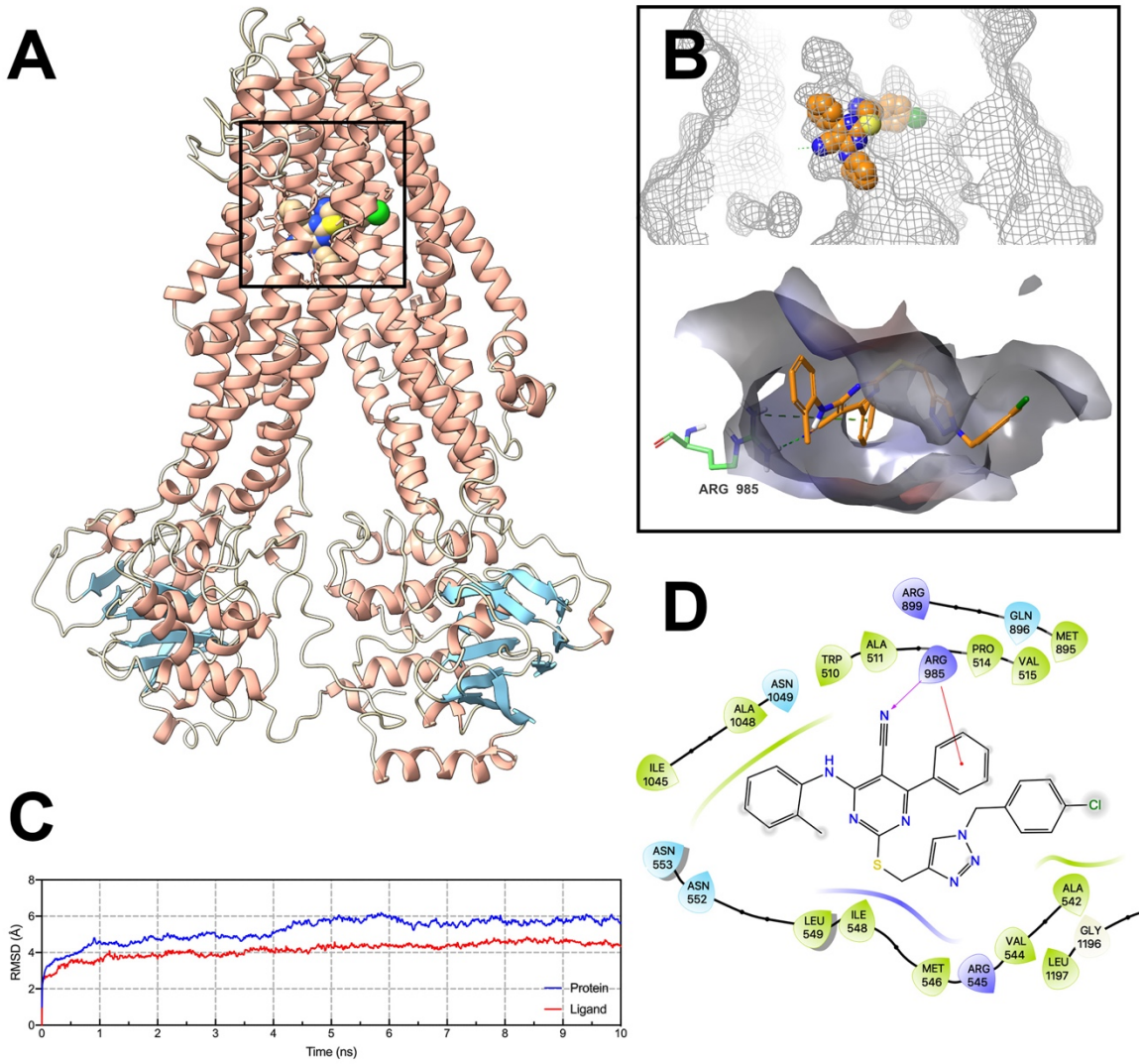

Figure 23. Interaction between CMP25 and MRP7 protein by docking simulation and molecular dynamics. A) An overview of the docked complex. Compound CMP25 molecule was displayed as balls marked by black square. B) Interaction between CMP25 and MRP7 protein. Top: MRP7 binding pocket was displayed as grey meshes. Down: Docked position of CMP25 within the binding pocket of MRP7. CMP25 was showed as colored sticks. Carbon: orange, nitrogen: blue, white: polar hydrogen, green: chloride, yellow: sulfur. C) Root mean square deviation (RMSD) of MRP7 (blue) and CMP25 (red) versus reference time (ns). D) 2D interaction diagram of CMP25-MRP7. The amino

acids within 3 Å are shown as colored bubbles, cyan indicates polar residues, and green indicates hydrophobic residues. The purple arrow indicates hydrogen bond and red line shows π-cation interaction.

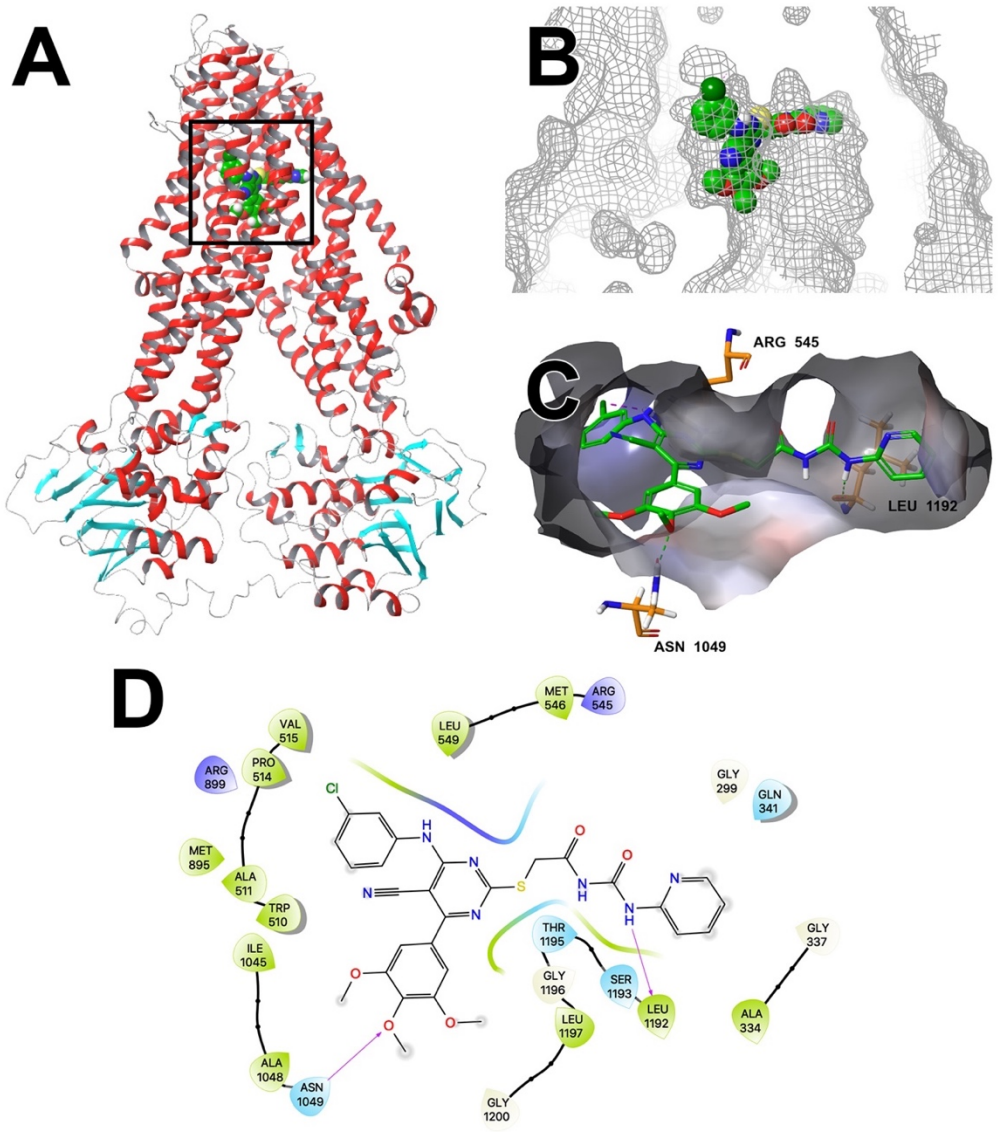

Figure 24. Interaction between CP55 and MRP7 protein by docking analysis. A) An overview of the docked complex. Compound CP55 molecule was displayed as balls marked by black square. B) Interaction between CP55 and MRP7 protein. MRP7 binding

pocket was displayed as grey meshes. C) Docked position of CP55 within the binding pocket of MRP7. CP55 was showed as colored sticks. Carbon: green, nitrogen: blue, white: polar hydrogen, dark green: chloride, yellow: sulfur, red: oxygen. D) 2D interaction diagram of CP55-MRP7. The amino acids within 3 Å are shown as colored bubbles, cyan indicates polar residues, and green indicates hydrophobic residues. The purple arrows indicate hydrogen bonds.

2.4 Discussion

Till now only a few studies reported MRP7 modulators since it's relatively new. Considering the important biological role that MRP7 plays in cancers, it is of great value to develop novel MRP7 inhibitors for both research and clinical purpose. Previously, we reported for the first time that CMP25 and CP55 potently reverse ABCB1-mediated MDR by inhibiting the efflux function of ABCB1 hence increasing the intracellular accumulation of chemotherapeutic agents such as paclitaxel *in vitro*. However, the effects of CMP25/CP55 on MRP7 was not determined yet. Here, we examined the potential inhibitory effects of CP55 and CMP25 on MRP7 by using HEK293/pcDNA3.1 and HEK293/ MRP7 cells.

Generally speaking, modulators of ABC transporters were composed of substrates, which are delivered by ABC transporters across membranes and usually stimulate the ATPase activity locates in the nucleotide binding domains, and inhibitors, which inhibits the transportation of substrates with different mechanisms (6). We first examined whether CMP25 or CP55 is a substrate of MRP7. The cytotoxicity assay showed that there is no significant difference in the IC_{50} values of parental and MRP7-

overexpressing cells for both drugs. Since MRP7 substrates will have higher IC_{50} due to the detoxification (efflux) function of MRP7, our results indicated that CMP25 or CP55 is not an MRP7 substrate. Meanwhile, we obtained the non-toxic concentration of CP55 and performed reversal study via MTT assay. Our results showed that CP55 at 1 or 3 μM significantly reversed the resistance of paclitaxel, vincristine and vinblastine in HEK293/MRP7 cells while not affecting their cytotoxicity in parental cells HEK293/pcDNA3.1. Also, there was no significant effect on the IC_{50} of cisplatin, which is not an MRP7 substrate. Altogether, our results indicate that CP55 antagonizes the MDR mediated by MRP7.

Altered MRP7 protein level could be one of the underlying mechanisms of reversed MRP7-mediated MDR. For example, the ABC transporter inhibitor poziotinib down-regulated the expression level of ABCG2 and conferred reversal effects on ABCG2-mediated MDR (116). The Western blotting results measured the protein expression level after treating cells with CMP25 and CP55. Our results confirmed that the MRP7 expression level was not significantly altered after treatment CMP25 or CP55. Thus, the reversal effect of CP55 on MRP7-mediated MDR was not due to alteration in MRP7 expression.

Functional MRP7 locates majorly on the cytoplasm membrane (119). As a membrane protein, altered subcellular localization of MRP7 could also lead to deteriorated transport function. Here, we determined the subcellular localization using immunofluorescence assay. The results showed that HEK293/MRP7 cells treated with CMP25 or CP55 did not show altered localization of MRP7.

The [^{3}H]-paclitaxel and [^{3}H]-vincristine accumulation assay showed that CP55 significantly enhanced the intracellular accumulation of paclitaxel and vincristine in HEK293/MRP7 cells. Subsequently, a time course of efflux study was performed to further confirm the accumulation results. Our results showed that the efflux of intracellular paclitaxel or vincristine was significantly inhibited by CMP25 or CP55 in the HEK293/MRP7 cells, while resistant cells without adding CMP25 or CP55 showed significantly lower intracellular accumulation. Besides, the blockage of efflux by CMP25 or CP55 is comparable to the known MRP7 inhibitor cepharanthine. Hence, the above results along with cytotoxicity data indicate that both CMP25 and CP55 are potent MRP7 inhibitors which block the efflux function of MRP7 protein.

Furthermore, we performed docking analysis using an MRP7 homology model (117). The docking score of both compounds in MRP7 binding pocket are high. Moreover, both compounds potentially bind at the predicted "inhibitor site" formed by amino acids Trp510, Ala511, Val515, Arg545, Leu549, Arg985, Ala1048 and Asn1049. Based on our study, molecules bound in the inhibitor site exhibit properties as MRP7 inhibitors such as efficiently reversing MRP7-mediated MDR.

Clinically, MRP7 has been reported to play important roles in acquired MDR and the prognosis of certain cancers (51,120). Also, MRP7 contributes to alteration in intracellular permeation of nevirapine, a non-nucleoside reverse transcriptase inhibitor for HIV-1 (121). Thus, development of MRP7 inhibitors is crucial in cancer treatment to overcome MRP7-mediated drug resistance. Here we reported two novel synthetic small molecules CMP25 and CP55 as potent MRP7 inhibitors, which could be potential adjuvant chemotherapeutic agents.

CHAPTER 3

In this chapter, we describe the establishment of an MRP7-overexpression ovarian cancer cell line.

3.1 Introduction

Here, we successfully established an MRP7-overexpressing SKOV3/MRP7 cell line by transfecting recombinant pcDNA3.1/MRP7 plasmids. The MRP7 expression and subcellular localization was confirmed by Western blotting and immunofluorescence assay respectively, indicating functional MRP7 transporter was produced. Moreover, the SKOV3/MRP7 cell line showed MDR to multiple chemotherapeutic drugs including paclitaxel, docetaxel, vincristine, vinorelbine, vinblastine but not to doxorubicin and cisplatin. Additionally, the MDR in SKOV3/MRP7 cells could be reversed by a known MRP7 inhibitor cepharanthine. In conclusion, overexpression of MRP7 in ovarian cancer could be an important factor in acquiring drug resistance to several commonly used chemotherapeutic drugs.

3.2 Materials and methods

Chemicals and reagents

Chemotherapeutic drugs and reagents used in this study were purchased from Sigma Chemical Co if otherwise stated (St. Louis, MO) including paclitaxel, docetaxel, vincristine, vinorelbine, vinblastine, doxorubicin, formaldehyde, Triton X-100, 3-(4, 5-dimethylthiazol-yl)-2, 5-diphenyltetrazolium bromide (MTT). Cisplatin, geneticin (G418) were purchased from Enzo Life Sciences (Farmingdale, NY). Recombinant MRP7 plasmid was prepared as previously described (122). Anti-MRP7 antibody (HPA041607)

produced in rabbit was purchased from Sigma-Aldrich, Inc. (St. Louis, MO). The [^{3}H]-paclitaxel was purchased from Moravek Biochemicals, Inc (Brea, CA). Fetal bovine serum (FBS), Dulbecco's modified Eagle's medium (DMEM), and 0.25% trypsin-EDTA were ordered from Corning Inc. (New York, NY). Phosphate buffer saline (PBS), dimethyl sulphoxide (DMSO), the Alexa Fluor 488-labeled secondary antibody (anti-mouse), 4,6-diamidino-2-phenylindole (DAPI) were ordered from Thermo Fisher Scientific Inc. (Rockford, IL).

Cell lines and cell culture

The human ovary adenocarcinoma cell line SKOV3 was purchased from ATCC (Manassas, VA). The HEK293 and HEK293/MRP7 cell lines were established and maintained as previously described (119). Both transfected cell lines were selected and cultured in DMEM with 10% FBS and 2 mg/mL G418 in a 5% CO_2 incubator at 37°C.

Recombinant MRP7 plasmid transfection

The recombinant expression vector of MRP7 was established based on pcDNA3.1 plasmid as previously described (122). Transfection of the empty or recombinant vector into SKOV3 was performed using Fugene6 transfection agent (Promega, Madison, WI) following the manufacturer's instructions. In brief, SKOV3 cells were seeded in 6-well plates with 100,000 to 200,000 cells per well with DMEM with 10% FBS. Then 100ml mixture of plasmid DNA and Fugene6 reagent (1:3 DNA:Fugene6 ratio) was prepared and incubated at room temperature for 30 min. Then the mixture was added into cell culture medium and incubated with cells for 2 days. When incubation ends, cell culture medium with transfection reagent was removed and transfected cells were rinsed with PBS. Selection medium (DMEM, 10% FBS and 2 mg/ml G418) was added and incubated

with cells for at least 14 days. Survived cells that formed single colonies were collected and cultured separately. The expression of MRP7 was further verified by Western blotting and immunofluorescence assay. In this paper, we use “SKOV3” to represent empty-vector-transfected “SKOV3/pcDNA3.1” unless otherwise stated.

Cell viability assay

The cell viability was measured by modified MTT assay as previously described with slight modifications (111). In brief, cells were seeded at a density of 6,000-8,000 cells/well in 96-well plates 24 h prior to adding drugs. Then cells were treated with different concentration of chemotherapeutic drugs for 72 h. For reversal study, MRP7 inhibitor cepharanthine were added to the 96-well plates 2 h before adding chemotherapeutic drugs. At the end of the treatment, cell viability was determined by MTT assay. Resistance fold was determined as fold relative to parental control groups. The half maximal inhibitory concentrations (IC_{50}) were calculated using the regression algorithm provided in GraphPad Prism 8.

Western blotting

Western blotting was performed as previously described with slight modifications (114). The previously established HEK293/MRP7 cell line was used as a positive control of MRP7. The whole protein in cell lysate was separated using SDS-polyacrylamide gel electrophoresis (SDS-PAGE) and electro-transferred to a polyvinylidene difluoride (PVDF) membrane. Then the membrane was blocked by 5% non-fat milk for 2 h at room temperature. The primary antibodies (1:1000 dilution) of MRP7 (HPA041607) and GAPDH were incubated with the blocked membrane at 4°C overnight. After rinsed with TBST for 3 times (15 min each), the membrane was incubated in the secondary HRP-

linked antibody (1:1,000 dilution) for 2 h at room temperature. Blotted protein bands were visualized using an enhanced ECL kit (Thermo Fisher Scientific Inc., Waltham, MA).

Immunofluorescence assay

In brief, SKOV3 and SKOV3/MRP7 cells were seeded in 24-well plates at a density of 50,000 cells/well and cultured overnight. Immunofluorescence assay was performed as previously described with slight modifications (99). In brief, cells were processed with 4% formaldehyde (37°C for 15 min) and 0.1% Triton X-100 (37°C for 15 min). Cells were rinsed with cold PBS between each step. Next, cells were incubated with primary anti-MRP7 (1:200) at 4°C overnight followed by incubation with Alexa Fluor 488 conjugated secondary antibody (1:1,000) for 2 h at 37 °C. DAPI was used to visualize the nuclei. Images were taken using a fluorescence microscope.

Accumulation and efflux assay

Accumulation and efflux assay were performed as previously described with slight modifications (123). In brief, Cell were seeded 10,000 cells/well into 24-well plates and cultured overnight. Then cells were incubated in culture medium containing 10 nM [^{3}H]-paclitaxel at 37°C for 2 h. After incubation, cells were rinsed with cold PBS and incubated in [^{3}H]-free medium for 0, 0.5, 1 and 2 h. At each time point, cells were detached and transferred into 5 ml scintillation fluid. The radioactivity was measured using a Tri-Carb liquid scintillation counter (Packard Instrument Inc., Chicago, IL). The [^{3}H]-paclitaxel level at 0 h was used to represent the intracellular accumulation within 2 h incubation. The change in [^{3}H]-paclitaxel levels at following time points were used to measure the efflux activity.

Statistical analysis

Comparison of differences among groups were performed using one-way ANOVA. The statistical criteria $p < 0.05$ was considered as statistically significant. All data were represented as mean ± SD from at least three independent experiments.

3.3 Results

Verification of the MRP7 expression and paclitaxel resistance in G418-selected SKOV3/MRP7 colonies

After culturing with selection medium containing 2 mg/ml G418 for 14 days, three colonies were collected and cultured for 1 week. Western blotting was performed when cells were 80% confluent. Results were shown in Figure 1. From the results in Figure 25, we can see that colony 1 exhibited the highest MRP7 expression. Moreover, it is worth noting that endogenous MRP7 expression was also detected in parental SKOV3 cells, even though the expression level was low. Furthermore, we examined the cytotoxicity of paclitaxel, a known substrate of MRP7, to see if the selected cell lines become resistant. Based on the results in Figure 25, only colony 1 showed significantly increased paclitaxel IC_{50}, indicating the acquired resistance from MRP7 overexpression. To further analyze the resistance profile of the new SKOV3/MRP7 cell line, we chose colony 1 for following steps.

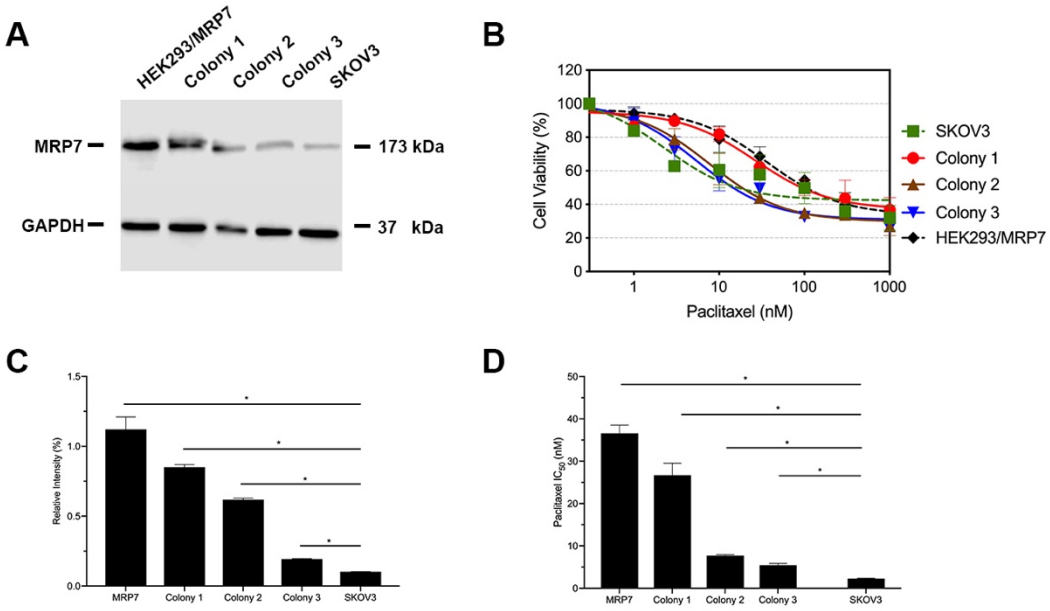

Figure 25. MRP7 expression and paclitaxel cytotoxicity in SKOV3/MRP7 cells. HEK293/MRP7 and SKOV3 were used as positive and negative controls, respectively. A) Western blotting results showing MRP7 expression of selected colonies and positive/negative controls. B) Cytotoxicity of paclitaxel in selected colonies and positive/negative controls. C) Qualitative analysis of MRP7 protein expression showed in A). D) Paclitaxel IC_{50} in selected colonies and positive/negative controls. * $p < 0.05$ versus the negative control group.

Subcellular localization of MRP7

Similar to other ABC transporters, MRP7 requires membrane localization for efflux function. Therefore, we examined the subcellular localization of SKOV3/MRP7 cells via immunofluorescence assay. In parental SKOV3 cells, no detectable green fluorescence was observed under the same parameters, which was consistent with the low expression level of endogenous MRP7 in SKOV3 cells. Strong green fluorescence was

observed on the membrane of SKOV3/MRP7 cells, suggesting that the overexpressed MRP7 transporter is localized on the cell membrane.

Intracellular accumulation of [^{3}H]-paclitaxel in SKOV3 and SKOV3/MRP7

We measured the intracellular accumulation of [^{3}H]-paclitaxel in SKOV3 and SKOV3/MRP7 after incubation in [^{3}H]-paclitaxel-containing culture medium for 2 h. The results in Figure 26 showed significant different levels of intracellular accumulation of paclitaxel in SKOV3 and SKOV3/MRP7 cells. Specifically, SKOV3/MRP7 showed lower intracellular accumulation of paclitaxel than SKOV3. Moreover, in SKOV3/MRP7, the reduced paclitaxel accumulation was significantly reversed by MRP7 inhibitor cepharanthine. Above findings are consistent with previous MTT results that SKOV3/MRP7 was less sensitive to paclitaxel due to the overexpression of MRP7 protein.

Efflux of [^{3}H]-paclitaxel in SKOV3 and SKOV3/MRP7

In the previous section, we found SKOV3/MRP7 cells showed lower paclitaxel intracellular accumulation, which could be significantly antagonized by MRP7 inhibitor cepharanthine. We then determined the efflux of paclitaxel by measuring the decreased intracellular amount at 0, 0.5, 1 and 2 h. Results in Figure 26 showed that by the end of the 2-hour incubation, the intracellular concentration of paclitaxel was decreased by approximately 15% in SKOV3 cells. While in SKOV3/MRP7, intracellular paclitaxel concentration was decreased by approximately 40%, indicating strong efflux of paclitaxel mediated by MRP7 transporter. The efflux function of MRP7 was inhibited by cepharanthine effectively as the final intracellular paclitaxel level was restored.

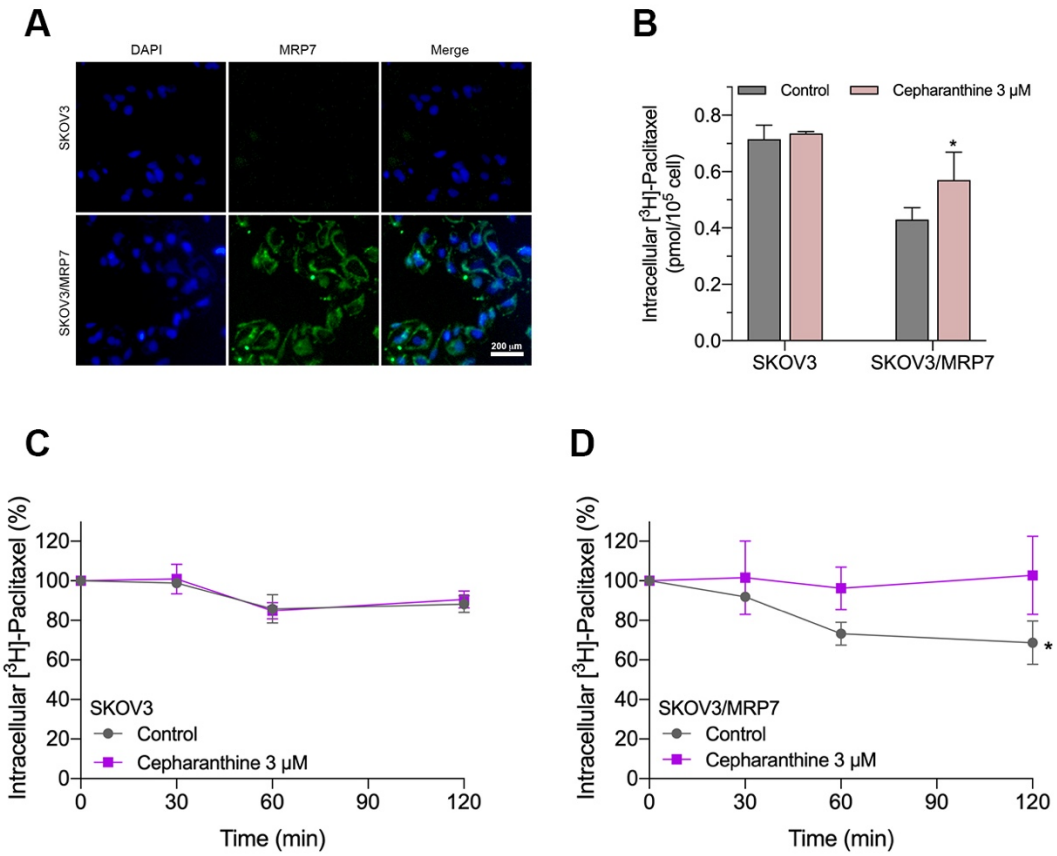

Figure 26. Immunofluorescence assay and accumulation-efflux assay. A) Subcellular localization of MRP7 transporter in SKOV3 and SKOV3/MRP7 cells. B) The intracellular accumulation of [^{3}H]-paclitaxel in SKOV3 and SKOV3/MRP7 cells. C) The efflux of [^{3}H]-paclitaxel in SKOV3 cells. D) The efflux of [^{3}H]-paclitaxel in SKOV3/MRP7 cells. Data in B-D are expressed as mean ± SD derived from three independent experiments. *$p < 0.05$ versus the control groups.

The drug resistance profile of MTP7-overexpressing ovarian cancer cell line

In previous sections, we have confirmed the successful establishment of an MRP7-overexpressing SKOV3 cell line. MTT assay and accumulation-efflux assay have confirmed the expression and biological function of the MRP7 protein. To further understand the drug resistance profile of the MRP7-overexpression ovarian cancer cell

line, we performed MTT assay to test the sensitivity to commonly used chemotherapeutic drugs. Results were displayed in Table 4. Specifically, SKOV3/MRP7 showed significant resistance to paclitaxel (10.43-fold resistance), docetaxel (3.82-fold resistance), vincristine (5.09-fold resistance), vinorelbine (6.86-fold resistance) and vinblastine (5.34-fold resistance). Moreover, SKOV3/MRP7 showed no significant resistance to P-gp/BCRP substrate doxorubicin. Also, SKOV3/MRP7 was not resistant to non-ABC-transporter-substrate cisplatin. Overall, the resistance profile of SKOV3/MRP7 was consistent with HEK293/MRP7 based on previous reports (90,119,124).

Table 4. The cytotoxicity of chemotherapeutic drugs in SKOV3 and SKOV3/MRP7 cell lines

Drugs	**IC_{50} value ± SD (nM)**		
	SKOV3	**SKOV3/MRP7**	Resistance fold [a]
Paclitaxel	4.483 ± 0.163	46.76 ± 4.565	10.43*
Docetaxel	3.645 ± 0.201	13.92 ± 1.715	3.82*
Vincristine	3.355 ± 0.527	17.08 ± 2.033	5.09*
Vinorelbine	5.272 ± 0.523	36.16 ± 5.558	6.86*
Vinblastine	2.640 ± 0.463	14.12 ± 2.847	5.34*
Doxorubicin	0.184 ± 0.012 (μM)	0.169 ± 0.012 (μM)	0.92
Cisplatin	4.342 ± 1.014 (μM)	5.200 ± 0.918 (μM)	1.20

[a] Resistance fold was calculated by dividing the IC_{50} values of the SKOV3/MRP7 cells by the IC_{50} of SKOV3 cells

* $p < 0.05$ versus the control group

MRP7 inhibitor cepharanthine antagonizes the drug resistance phenotype of SKOV3/MRP7 cells

To further confirm that the overexpression of MRP7 is the major contributing factor of drug resistance, we performed MTT assay with co-treatment of chemotherapeutic drugs and MRP7 inhibitor cepharanthine. As shown in Figure 27, cell viability curves of SKOV3/MRP7 showed left-shifting when adding cepharanthine, indicating resistance to known MRP7-substrate drugs were reversed in SKOV3/MRP7 by cepharanthine. Specifically, significant changes were observed in the IC_{50} of paclitaxel (from 33.76 nM to 7.61 nM), docetaxel (18.92 nM to 7.00 nM), vincristine (17.01 nM to 6.10 nM), vinblastine (14.12 nM to 4.23 nM) and vinorelbine (30.24 nM to 10.39 nM). The cell viability of parental SKOV3 cells were not significantly affected by cepharanthine. Cisplatin was used as a negative control since it is not a substrate of major ABC transporters. Cell viability of both SKOV3 and SKOV3/MRP7 cells were not altered.

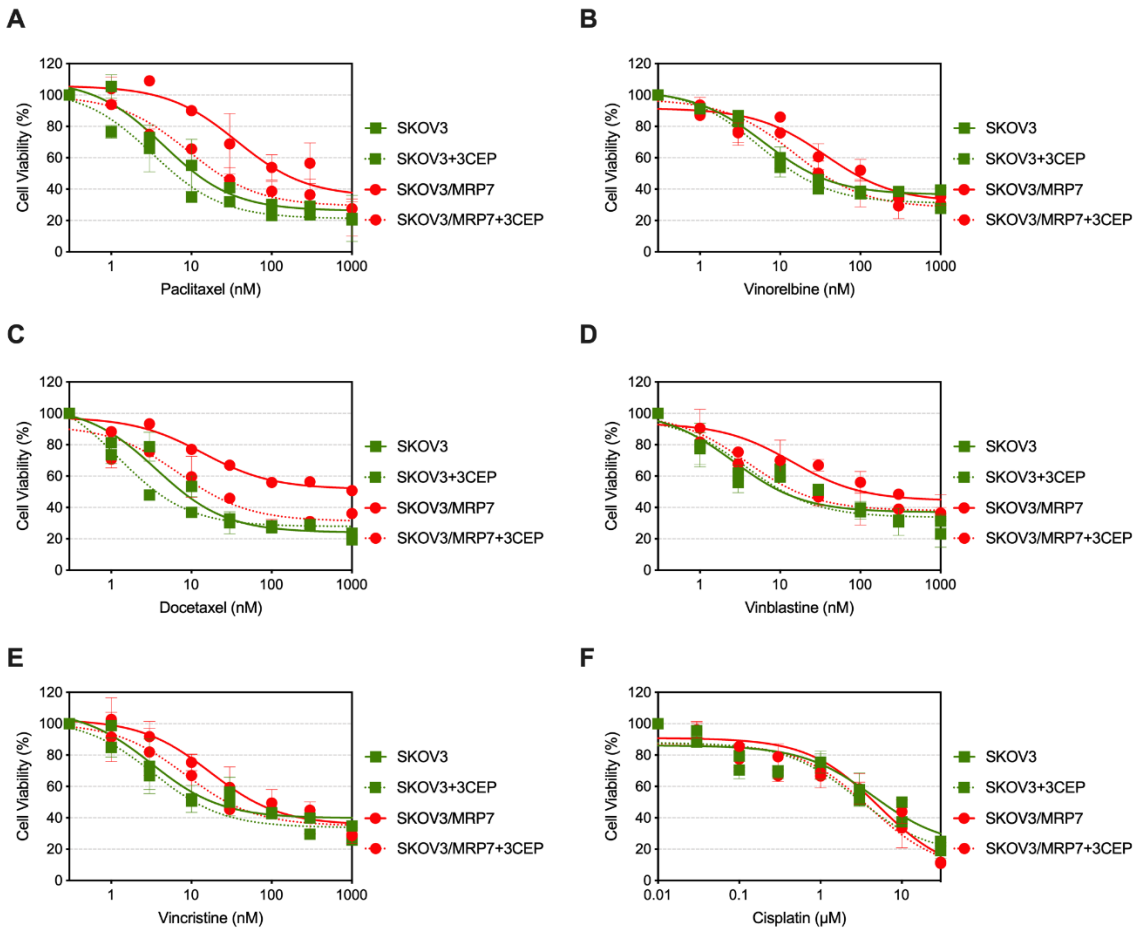

Figure 27. Reversal of MRP7-mediated drug resistance using cepharanthine in SKOV3 and SKOV3/MRP7 cells. Chemotherapeutic drug versus cell viability was plotted. A) paclitaxel; B) vinorelbine; C) docetaxel; D) vinblastine; E) vincristine; F) cisplatin. Green solid lines represent SKOV3, green dashed lines represent SKOV3 + 3 μM cepharanthine, red solid lines represent SKOV3/MRP7, red dashed lines represent SKOV3/MRP7 + 3 μM cepharanthine. CEP: cepharanthine. Data are expressed as mean ± SD derived from three independent experiments.

3.4 Discussion

Overall, our results suggest that overexpression of MRP7 could be a critical factor of acquired MDR in ovarian cancer cells. We first selected three transfected cell colonies which survived from G418 medium for at least 14 days. Then, we performed Western blotting and MTT assay to verify the MRP7 expression and paclitaxel resistance mediated by MRP7, respectively. Results showed that colony 1 exhibited the highest MRP7 expression level, which was comparable to the positive control HEK293/MRP7 cells. MTT assay further demonstrated that colony 1 was resistant to paclitaxel treatment compared to SKOV3 cells. As a membrane transporter, subcellular localization of MRP7 is crucial for its biological function (125). Thus, we performed immunofluorescence assay to determine the subcellular localization of MRP7 in SKOV3/MRP7 cells. Results showed that the MRP7 protein was mainly localized on cell membrane, which indicate functional MRP7 transporters (106). Subsequently, we performed accumulation-efflux assay to further verify the MRP7 efflux function in SKOV3/MRP7 cells. The results showed that intracellular paclitaxel concentration was significantly decreased in SKOV3/MRP7 cells and restored by MRP7 inhibitor cepharanthine (126).

In summary, here we for the first time showed that overexpression of MRP7 may be an important mechanism in acquired resistance to paclitaxel and other chemotherapeutic agents in ovarian cancer. Although the MDR mechanism in ovarian cancer might be more complex, our finding emphasized the importance of MRP7 in the development of ovarian cancer drug resistance. Therefore, MRP7 level could potentially serve as a biomarker for MDR during chemotherapy. Additionally, establishment of this MRP7-overexpressing ovarian cancer cell line may facilitate the discovery of novel

modulators to overcome acquired MDR in ovarian cancer and improve the therapeutic efficacy in cancer patients.

CHAPTER 4

4.1 Introduction

Here, we present *Mrp7Pred*, an online MRP7 substrate and MRP7 inhibitor prediction server based on machine learning techniques, which is freely available at http://www.mrp7pred.com. The web application has a friendly user interface and is very easy to use even if the user has no computational chemistry background. Therefore, *Mrp7Pred* can be used for virtual drug screening in order to discover novel MRP7 substrates and/or inhibitors.

4.2 Materials and methods

Dataset establishment and curation

The training and validation data used in this task is a manually curated non-redundant MRP7 substrate/inhibitor/non-interactor dataset composed of experimentally validated substrates and inhibitors (54) and non-interactors (64). The size of our dataset is small due to the limited available studies regarding MRP7. Due to the fact that various experimental methods were used to identify MRP7 substrates or inhibitors *in vitro*. As a result, we need to determine the criteria to clearly define positive or negative data in this project. Here, we defined several rules to determine if a drug is an MRP7 substrate, an inhibitor or a non-interactor. Substrates will show reduced cytotoxicity in MRP7 overexpressing cells, which can be reversed by MRP7 inhibitors. Examples are paclitaxel, vincristine and docetaxel. Inhibitors could potently reverse MRP7-mediated drug resistance, while not showing significant difference in IC_{50} values in parental and MRP7-overexpressing cells. Given some studies did not focus on chemotherapeutic drugs

but some biomolecules like LTC_4, inhibiting the transportation of such molecules via MRP7 is also an evidence of an inhibitor, although ambiguous since substrates may also interfere the transportation of other substrates. For non-interactors, we chose molecules that do not exhibit any of the above evidence *in vitro*. Part of the MRP7 substrates data were extracted from (127). The original dataset contains 1429 anticancer drugs tested against 49 ABC transporters. Drug properties were represented by the correlation between ABC transporter mRNA expression level and sensitivity in respective cells. As shown in Figure 28, negative r value indicates the substrate property because the cells became less sensitive if there are more ABC transporter expression. The MRP7 substrates were then selected by $r < -0.25$ following a previous study (128).

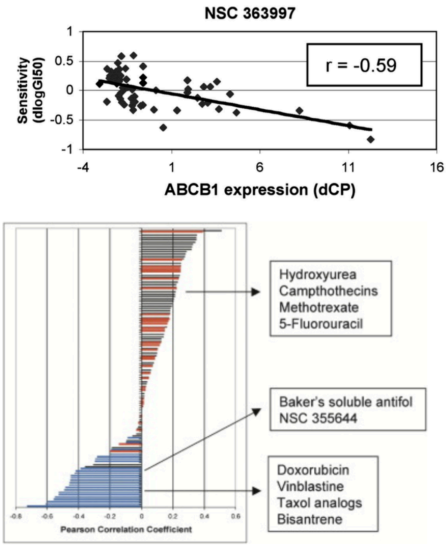

Figure 28. Sample data snippet for ABCB1 from Szakács et al., 2004.

Model training and validation

The best model was trained via an automated pipeline composed of featurization, feature selection and parameter grid search. The compounds were represented as SMILE strings which were standardized by python package RDKit. Features include 1D and 2D

features generated by RDKit and ChemoPy (129). 1D features include constitutional descriptors such as molecular weight and atom counts. 2D features include connectivity descriptors, topology descriptors, Basak descriptors, Kappa descriptors, Burden descriptors, E-state descriptors, Moran autocorrelation descriptors, Geary autocorrelation descriptors, Moreau-Broto autocorrelation descriptors and MOE-type descriptors (129). Features were selected in a filter-based method. Specifically, feature pairs with high Pearson's correlation were removed (Figure 29).

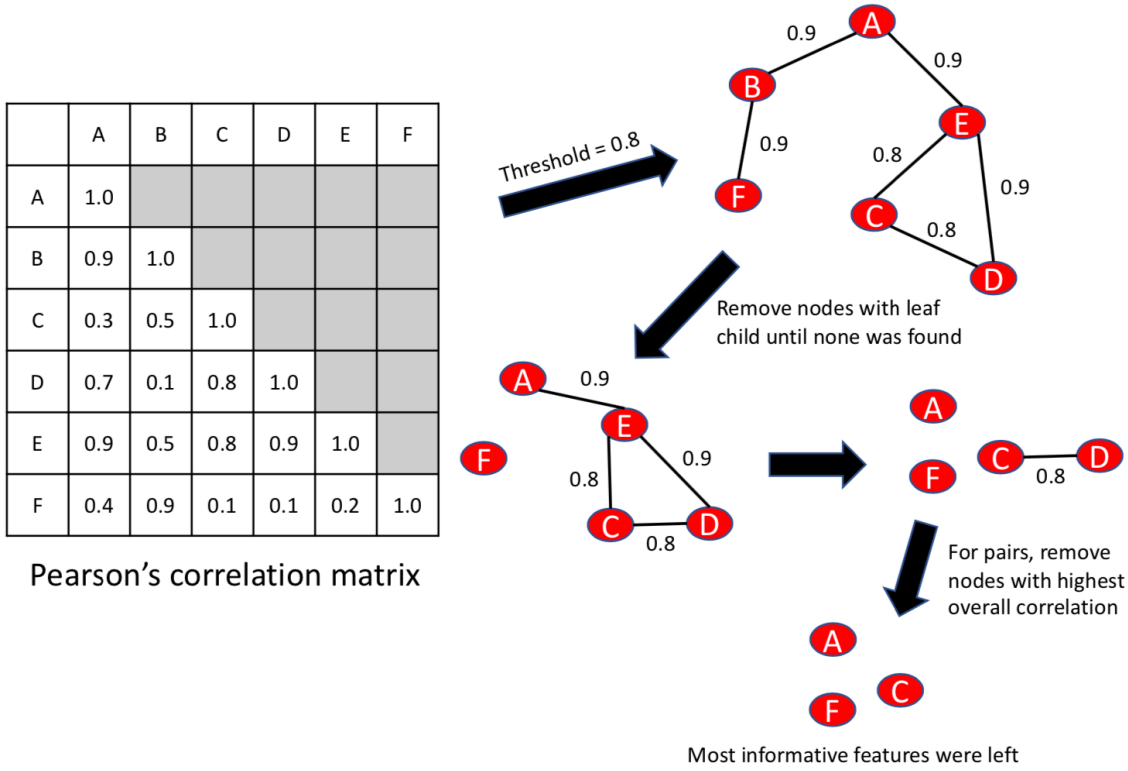

	A	B	C	D	E	F
A	1.0					
B	0.9	1.0				
C	0.3	0.5	1.0			
D	0.7	0.1	0.8	1.0		
E	0.9	0.5	0.8	0.9	1.0	
F	0.4	0.9	0.1	0.1	0.2	1.0

Figure 29. Pairwise feature selection. Features with high correlation (i.e. Pearson's correlation) provides similar information of the input data. Features were first converted into a correlation matrix then an undirected graph to remove highly correlated pairs.

The validated model was then benchmarked against docking using our homology model. Docking results were represented in a binary pattern by setting different thresholds to separate interactors and non-interactors. Common metrics including precision, recall, F1, accuracy and ROC-AUC were then applied to compare the machine learning model and docking analysis results.

***In silico* and *in vitro* validation of FDA-approved drugs as MRP7 substrates or modulators**

We collected 70 FDA-approved drugs (except 17 pre-clinical drugs) under clinical trial or on market. Both Mrp7Pred and docking analysis were implemented for the initial prediction. Candidates with high scores were subjected to *in vitro* validation using MTT cell viability assay in HEK293, HEK293/MRP7, SKOV3 and SKOV3/MRP7 cells.

Setting up online server for Mrp7Pred

The online web application for Mrp7Pred was deployed based on Python, Flask and Nginx. The backend was hosted and setup on a Digital Ocean droplet. The web server is freely accessible for academic use at http://www.mrp7pred.com. Currently the function is only available for internal use due to the pending publications.

4.3 Results

Model training and validation

The pairwise feature selection results were shown in Figure 30. Dark red and green indicate strong feature correlation. The results showed that features with high correlation have been effectively removed.

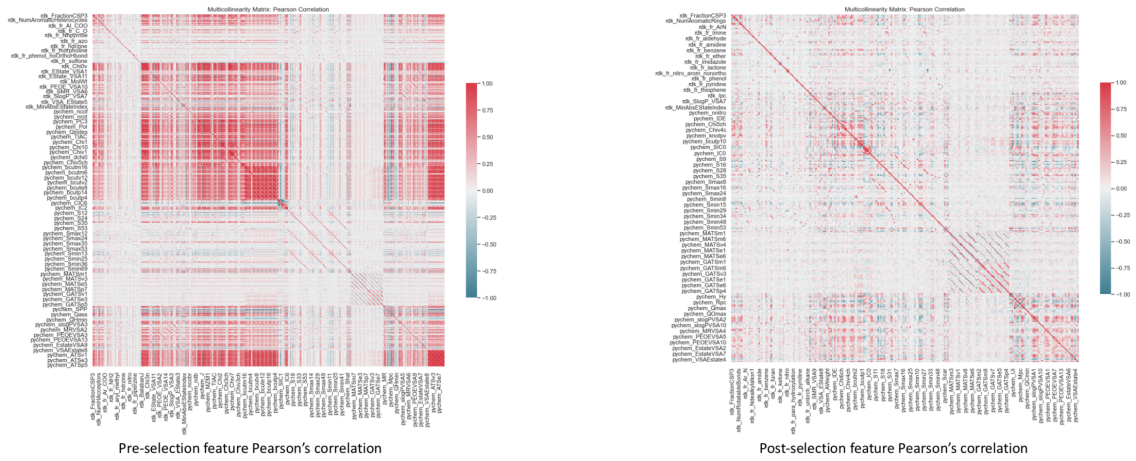

Figure 30. Feature selection results. Left: Pearson's correlation of all features before selection. Right: Pearson's correlation of all features after selection. Red: Pearson's correlation larger than zero. Green: Pearson's correlation smaller than zero.

Best models were then obtained by a linear grid search over all combinations of model parameters. We use ROC-AUC as the major matric to determine model performance. Eventually, one MRP7 inhibitor prediction model and one MRP7 substrate prediction model was successfully established. The model performance was also compared with docking analysis. Results were given in Figure 31. According to the results, docking simulation achieved the best performance when the threshold was set to -7.0 kcal/mol, which means if the compound got docking energy lower than -7.0 kcal/mol, we will consider it being an MRP7 interactor. In out held-oust test dataset, 14 interactor sand 21 non-interactors. Overall, both modes got reasonable results, while machine learning models generally need lower execution time and computational resources. Moreover, for the performance metrics, our Mrp7Pred model showed higher recall, F1

and ROC-AUC. Overall, the Mrp7Pred model showed good prediction accuracy in held-out test data.

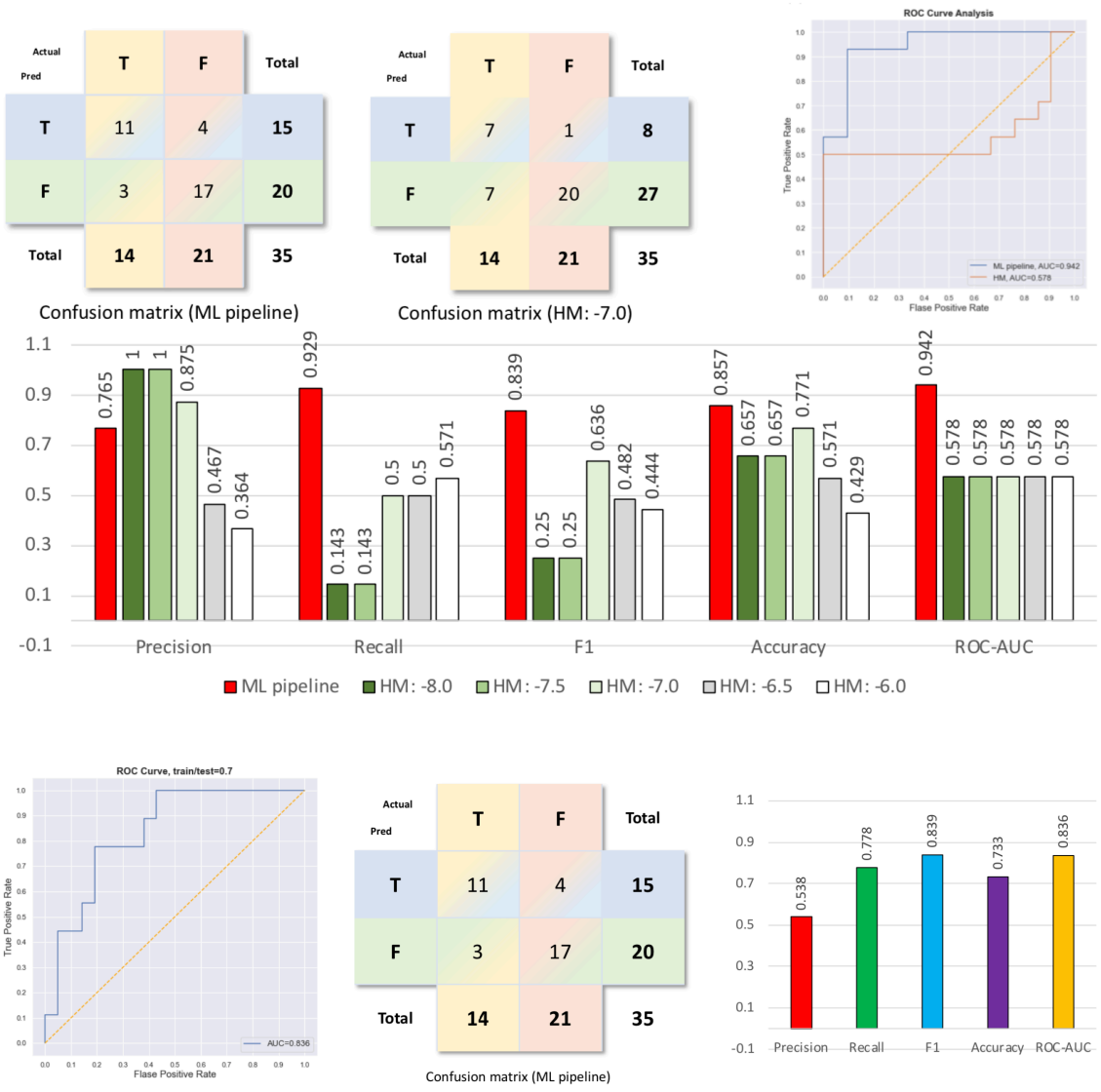

Figure 31. Model performance and benchmark with docking analysis. Confusion matrix, ROC-AUC, precision, recall, F1 score and accuracy were displayed. In the middle bar graph, docking results were represented as dark green, green, light green, grey and white columns for affinity score threshold -8.0 kcal/mol, -7.5 kcal/mol, -7.0 kcal/mol, -6.5 kcal/mol, -6.0 kcal/mol, respectively.

Implement Mrp7Pred to FDA-approved drugs for MRP7 interactor discovery

Next, we implement Mrp7Pred to a series of FDA-approved anticancer drugs, in order to see if we could identify novel MRP7 substrates or inhibitors. We used Mrp7Pred for pre-screen on 70 drugs. In the end, we found 10 drugs with high substrate score and 27 drugs with high inhibitor score (Table 5). In the subsequent *in vitro* test, 2 out of 10 drugs were identified as MRP7 substrates and 4 out of 27 were identified as MRP7 inhibitors (Figure 32, 33). MTT results of non-substrates and non-inhibitors were not shown here. The overall hit rate is 17.5%.

Table 5. Drugs with high substrate score or inhibitor score.

Drug Name	**Substrate Score**
Disulfiram	0.869
Ixazomib Citrate	0.960
Drug Name	**Inhibitor Score**
Selonsertib	0.557
Berzosertib	0.610
IWR-1-endo	0.581
Vatalanib	0.531

Figure 32 showed the MTT results of disulfiram and ixazomib citrate in two MRP7-overexpression cell lines as well as their parental cell lines. Results showed that

both disulfiram and ixazomib citrate showed higher IC_{50} in MRP7-overexpressing cells than in parental cells. Specifically, disulfiram had resistance fold of 1.92 in HEK cells and 2.44 in SKOV3 cells, while ixazomib citrate had resistance fold of 8.35 in HEK cells and 9.64 in SKOV3 cells. Additionally, the resistance in MRP7-overexpressing cells could be at least partially reversed by a known MRP7 inhibitor tariquidar at 0.3 μM. In summary, we successfully identified two MRP7 substrates, disulfiram and ixazomib citrate, using Mrp7Pred.

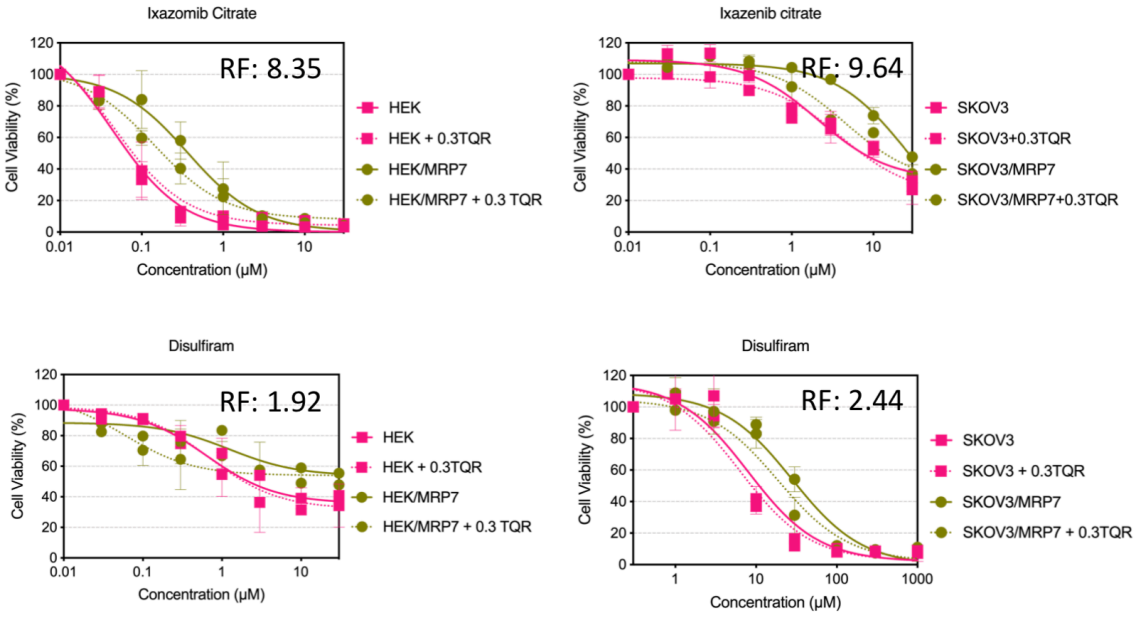

Figure 32. Cell viability assay results of disulfiram and ixazomib citrate in HEK, HEK/MRP7, SKOV3 and SKOV3/MRP7 cells. Solid red lines: parental cells only, red dashed lines: parental cells + TQR, solid green lines: MRP7-overexpressing cells only, green dashed lines: MRP7-overexpressing cells + TQR. RF: resistance fold, calculated by the IC_{50} in resistant cells divided by IC_{50} in parental cells. TQR: tariquidar. Data are expressed as mean ± SD derived from three independent experiments.

Figure 33 showed the MTT results of predicted MRP7 inhibitors in SKOV3 and SKOV3/MRP7 cells. To validate predicted inhibitors, we treated cells with a combination of one of the four predicted drugs and paclitaxel. Based on Figure 33, the four predicted inhibitors could at least partially reverse MRP7-mediated paclitaxel-resistance in SKOV3/MRP7 cells. Specifically, 10 μM selonsertib reduced the resistance fold from 8.8 to 3.7, vatalinib reduced the resistance fold from 8.8 to 3.9, IWR-1-endo reduced the resistance fold from 8.8 to 5.7, berzosertib reduced the resistance fold from 8.8 to 5.7. Till now, we have confirmed the predictability of our Mrp7Pred model.

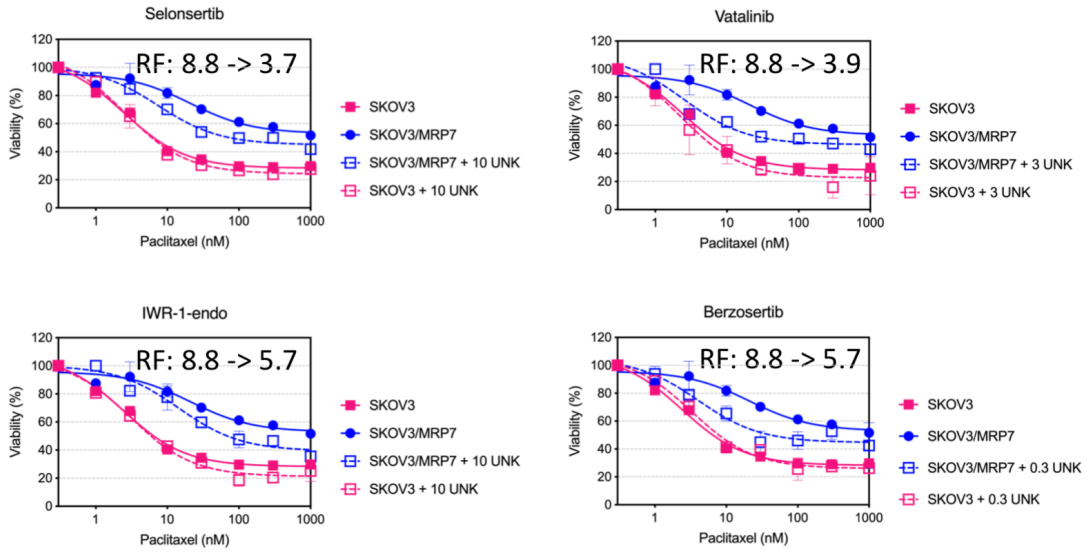

Figure 33. Validating predicted MRP7 inhibitors. Cell viability was represented in percentage. Red solid line: SKOV3, blue solid line: SKOV3/MRP7, red dashed line: SKOV3 + predicted inhibitor, blue dashed line: SKOV3/MRP7 + predicted inhibitor. RF: resistance fold, calculated by the IC_{50} in resistant cells divided by IC_{50} in parental cells. Data are expressed as mean ± SD derived from three independent experiments.

Mrp7Pred online web server

To extend the usability of our Mrp7Pred model, we deployed the substrate and inhibitor model to a web server for users, which is freely available at http://www.mrp7pred.com. Figure 34 displayed an overview workflow of the web server. In brief, the user could upload their own compound dataset which was formatted based on our instruction.

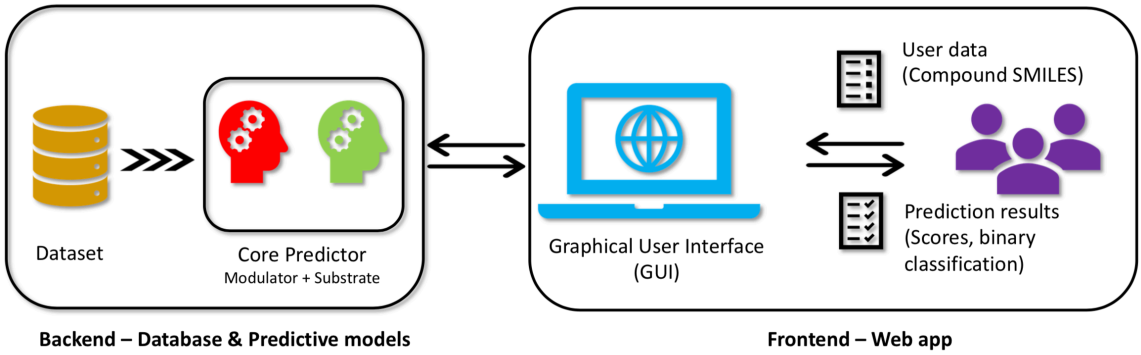

Figure 34. An overview of the workflow of the Mrp7Pred web server.

The graphic user interface is straightforward and easy to use. There are 5 sections, and we will be briefly introducing each section here.

Figure 35 showed the title page and side navigation bar. From here, user could be directly guided to the prediction section or to view other sections. Figure 36 showed the section where basic information of MRP7 was introduced to the users. Figure 37 showed the instruction page, where users can find guidance in data preparation, model implementation and result interpretation. Figure 38 showed the section of sample data, where users can download our sample data to test the server. Figure 39 showed the section where users can upload their prepared data and run the prediction. Once the users click “run”, a waiting page will pop up and models start running. The model will first

featurize all compounds then make prediction. The execution time varies depend on the complexity of chemical structures and data size. On average, the execution time is 10-15 seconds per compound. Once the prediction finishes, the users will see a result page similar to Figure 41. The compound name, 2D chemical structure, SMILES string, molecular weight, substrate score and inhibitor score will be displayed. Compounds failed in featurization will not appear in the report. Users can then click “Save as PDF” to download the PDF version of the report.

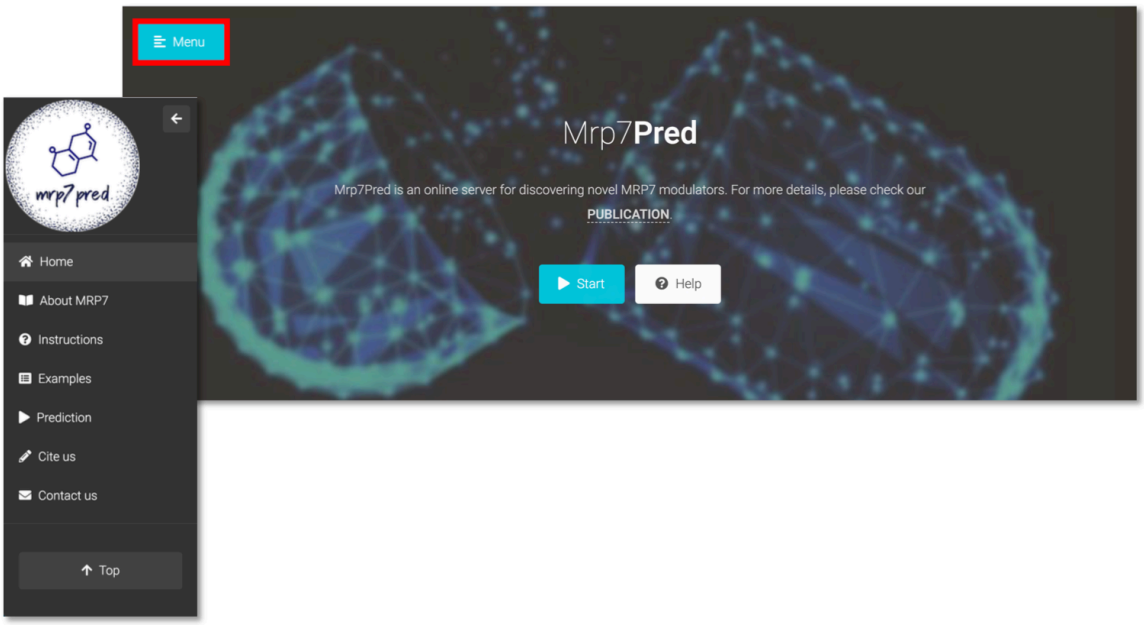

Figure 35. Section 1: the title section of Mrp7Pred web server and the side navigation bar.

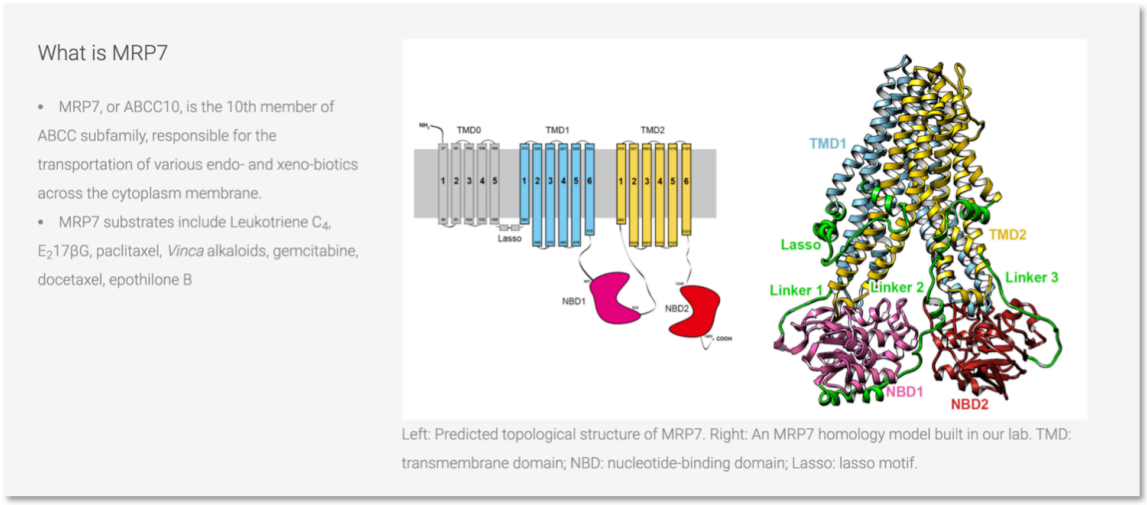

Figure 36. Section 2:basic information of MRP7.

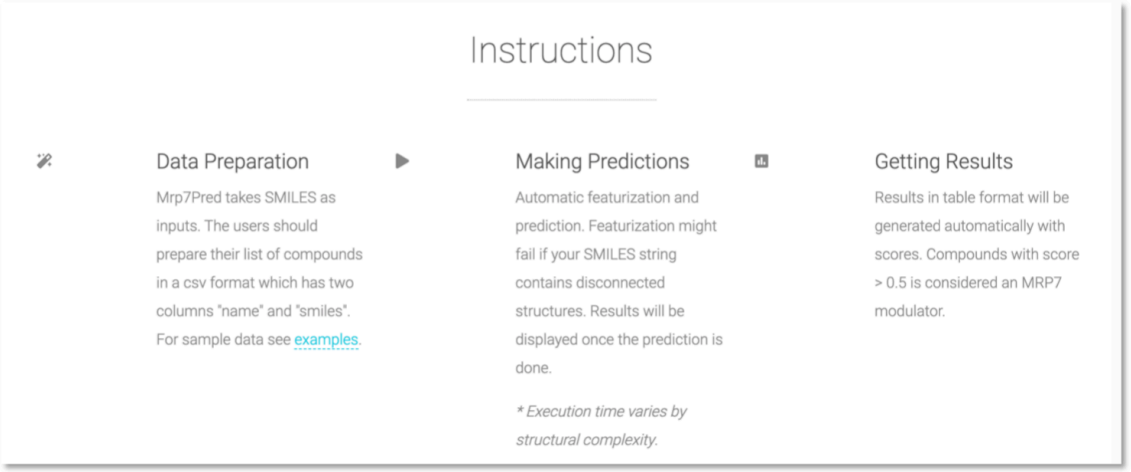

Figure 37. Section 3: user instruction for data preparation, model implementation and results interpretation.

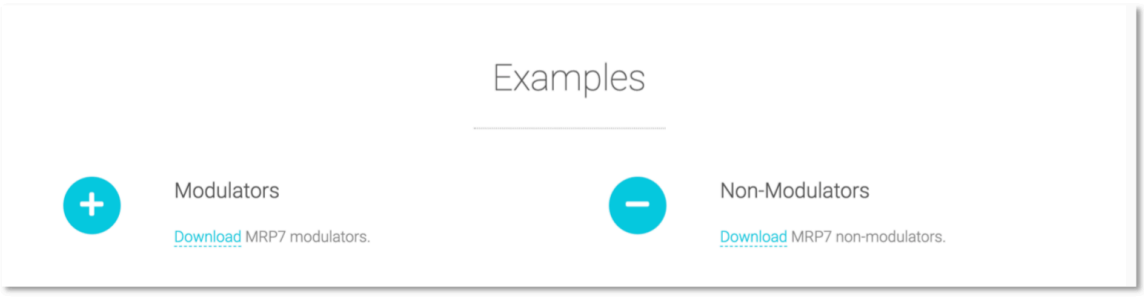

Figure 38. Section 4: sample data. Modulator and non-modulator sample data were provided.

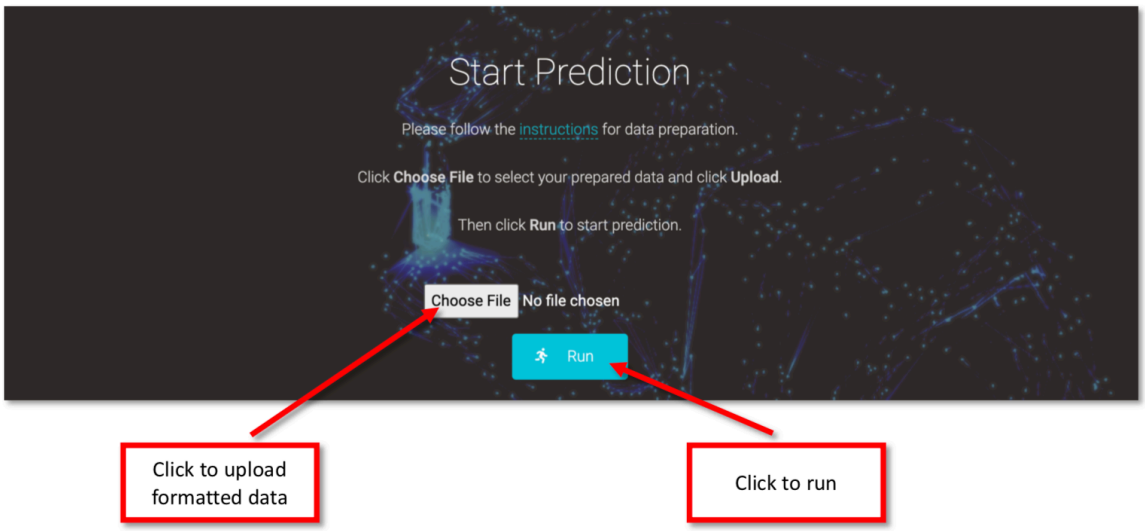

Figure 39. Section 5: start prediction.

Frontend

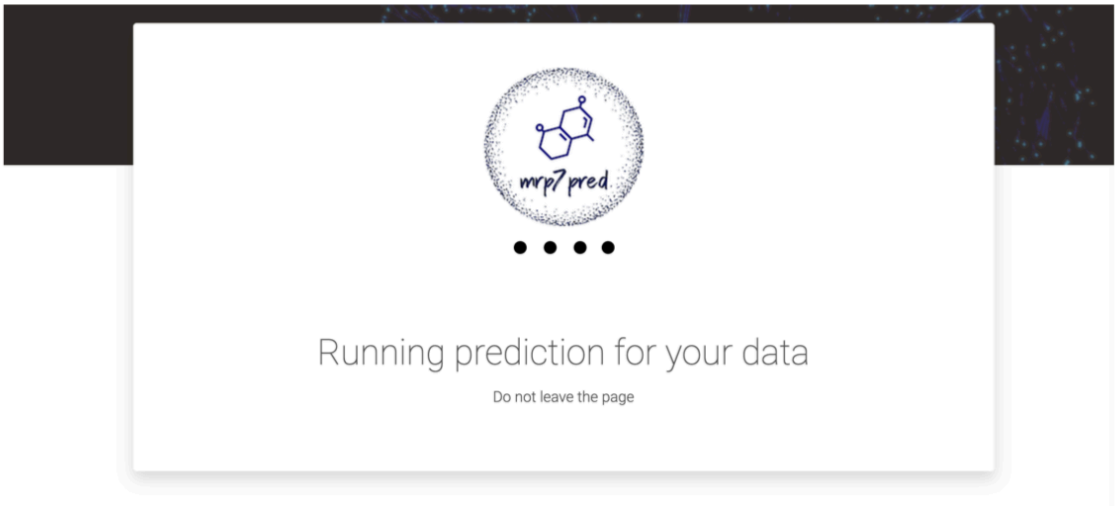

Backend

```
127.0.0.1 - - [12/Mar/2021 12:45:23] "GET / HTTP/1.1" 200 -
Loading trained model ... Done!
Generating features ...
Featurized 1. cAMP
SMILES: Nc1ncnc2c1ncn2C1OC2COP(=O)(O)OC2C1O
Time cost: 1.524s

Featurized 2. paclitaxel
SMILES: CC(=O)OC1C(=O)C2(C)C(O)CC3OCC3(OC(C)=O)C2C(OC(=O)c2ccccc2)C2(O)CC(OC(=O)C(O)C(NC(=O)c3ccccc3)c3ccccc3)C(C)=C1C2(C)C
Time cost: 5.168s

Featurized 3. vincristine
SMILES: CCC1(O)CC2CN(CCc3c([nH]c4ccccc34)C(C(=O)OC)(c3cc4c(cc3OC)N(C=O)C3C(O)(C(=O)OC)C(OC(C)=O)C5(CC)C=CCN6CCC43C65)C2)C1
Time cost: 5.927s

Featurized 4. E217bG
SMILES: CC12CCC3c4ccc(O)cc4CCC3C1CCC2OC1OC(C(=O)O)C(O)C(O)C1O
Time cost: 2.181s

Featurized 5. epothiloneB
SMILES: CC(=Cc1csc(C)n1)C1CC2OC2(C)CCCC(C)C(O)C(C)C(=O)C(C)(C)C(O)CC(=O)O1
Time cost: 1.91s

Featurized 6. vinblastine
SMILES: CCC1(O)CC2CN(CCc3c([nH]c4ccccc34)C(C(=O)OC)(c3cc4c(cc3OC)N(C)C3C(O)(C(=O)OC)C(OC(C)=O)C5(CC)C=CCN6CCC43C65)C2)C1
```

Figure 40. Waiting page and backend information.

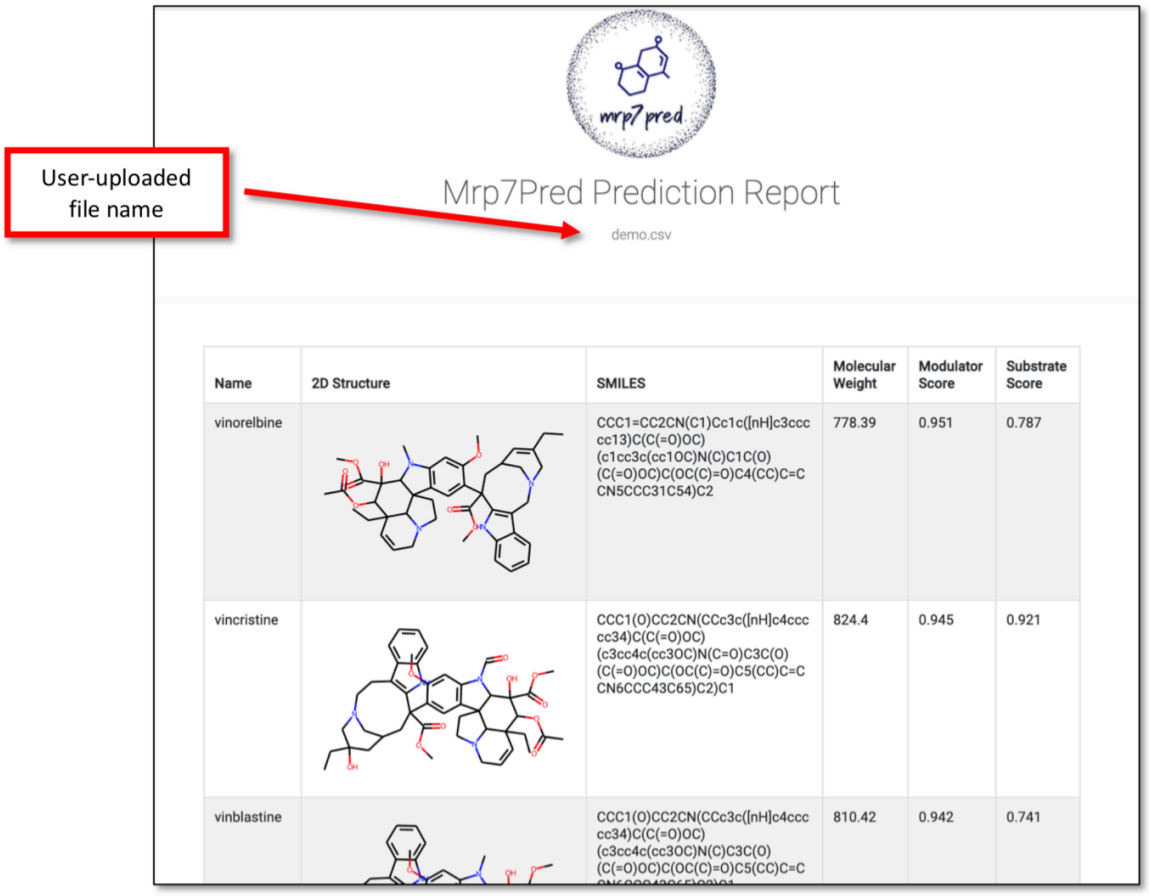

Figure 41. Prediction report.

4.4 Discussion

Here, we for the first time established a machine learning model for MRP7 substrate and inhibitor prediction, which we believe will be beneficial to the field of cancer drug resistance. By using Mrp7Pred, researchers could accelerate the progress of MRP7 inhibitor discovery and lower the cost. It is worth noting that although the machine learning model could quickly provide predictions for MRP7 inhibitors and substrates, the interpretability of this model still needs improvement. Unlike docking analysis, where the potential molecular interactions that may contribute to the binding are

clearly illustrated, our model cannot provide information regarding factors that may contribute to a positive prediction. Although we can use more complex model, such as attention-based sequential models to show important groups or structures, it is more feasible to deploy a simpler model as an online server considering the computational resources.

LIMITATIONS

Identifying drug target interactions greatly reduced the candidates for the search of potential medications (130). As a result, drug-target interaction screening is always the first step in drug discovery (131). Based on the "no free lunch theorem", a successful machine learning model needs reasonable data to make reasonable predictions (132). Moreover, in drug-target interaction prediction, the acquisition of negative data can be challenging since it is hard to determine if a drug is not interacting with the protein of interest. Currently, a large number of supervised models regard unlabeled data or those without experimental results as negative, which could be erroneous (133). In this study, we carefully picked our negative data. Instead of using those without clear results, we chose compounds that particularly tested for MRP7 interaction but got negative results. For example, a negative compound would have similar cytotoxicity in both parental and resistant cell lines. Additionally, negative compounds will not significantly alter the drug resistance profile of resistant cells. Our negative data is more reliable than simply unlabeled data, however, considering the complexity of cell system, there might be multiple pathways including MRP7 overexpression that affect the drug resistance (134). Moreover, researchers from different research groups may have different criteria in defining MDR in cancer cells, which could lead to inconsistency in drug-target

interactions. As a result, it is necessary to unify the criteria for defining the multidrug resistance in cancer cells so that more meaningful discoveries could be obtained via *in silico*, *in vitro* or *in vivo* approaches.

Since MRP7 was first discovered in 2001 and is one of the most recent discovered ABC transporters. Due to the limitation of proper cell models, not so many studies are available regarding the modulation of MRP7-mediated drug resistance. As a result, we are not able to obtain much data to train a machine learning model. Since the performance of a machine learning model heavily relies on the quality of data, less data may cause the model to underfit all of the parameters which will deteriorate the prediction accuracy (135). This is also an important factor when selecting proper models. In this study, we decided to use simpler models with fewer parameters given the limited amount of data. Finally, small size data may lead to bias since we cannot guarantee that our training data accurately represent the population. Thus, it is crucial to expand the dataset size.

Currently, our online webserver performs featurization and prediction once received the input data prepared by users. However, the featurization is time-consuming. To accelerate the whole process, it is important for us to further optimize the algorithm to improve the prediction efficiency. We do provide users with an alternative: by using the local version which needs users to build the Mrp7Pred from scratch. The local version avoids Internet traffic and the limitation in computational resources of the web server. In the future, we could implement the model using compound embeddings which could be accelerated by pre-training (136).

FUTURE PERSPECTIVES

Since the discovery of P-glycoprotein and its role in cancer drug resistance, extensive studies have been made to design potent reversal agents in order to overcome drug resistance and increase the therapeutic efficacy (137). However, after the failure of several ABC transporter inhibitors in clinical trials, such as tariquidar, researchers are now turning to different directions in this field (20) including developing high-throughput methods to reduce the cost of pre-screening so that we could find candidates from a larger pool (138). Computational models were boosted thanks to the bloom of modern machine learning techniques. Nowadays, researchers have more and more choice in performed computational compound screening such as traditional structure-based or ligand-based pharmacophore screening (139), probability-based Bayesian models (140), conventional supervised models (28) or more complex neural network-based deep learning models (141). In this work, we focused more on traditional supervised learning models including SVM, random forest, gradient boost or simply neural networks. In future works, more complex and interpretable models could be implemented in order to expand the predictability of our model as well as extend the use cases (142).

Cancer is still one of the worldwide leading cause of death, and the drug resistance in recurring cancer further reduced the patients' survival rate (143). As a result, it is still of great importance to develop potent and selective inhibitors to overcome cancer drug resistance by targeting ABC transporters especially MRP7, which has been found to mediate the resistance of taxanes and vinca alkaloids. Our work not only expand our understanding in MRP7-mediated cancer drug resistance, but also provided an accessible method to predict novel MRP7 substrates or inhibitors, which could then be

validated in our ovarian cancer MRP7 cell line. In summary, this work greatly extends the study regarding MRP7-mediated cancer drug resistance, and hopefully could provide valuable insights in overcoming cancer drug resistance in the future.

REFERENCES

1. Juliano RL, Ling V. A surface glycoprotein modulating drug permeability in Chinese hamster ovary cell mutants. *Biochimica et Biophysica Acta (BBA) - Biomembranes*. 1976 Nov;455(1):152–62.

2. Fletcher JI, Haber M, Henderson MJ, Norris MD. ABC transporters in cancer: more than just drug efflux pumps. *Nat Rev Cancer*. 2010;10(2):147–56.

3. Cui Q, Yang Y, Ji N, Wang J-Q, Ren L, Yang D-H, et al. Gaseous signaling molecules and their application in resistant cancer treatment: from invisible to visible. *Future Med Chem*. 2019 Feb;11(4):323–36.

4. Kadioglu O, Saeed MEM, Munder M, Spuller A, Greten HJ, Efferth T. Effect of ABC transporter expression and mutational status on survival rates of cancer patients. *Biomedicine & Pharmacotherapy*. 2020 Nov;131:110718.

5. Dvorak P, Pesta M, Soucek P. ABC gene expression profiles have clinical importance and possibly form a new hallmark of cancer. *Tumour biology : the journal of the International Society for Oncodevelopmental Biology and Medicine*. 2017 May;39(5):1010428317699800.

6. Chen X-Y, Wang J-Q, Yang Y, Li J, Chen Z-S. Natural Product as Substrates of ABC Transporters: A Review. *Recent Pat Anticancer Drug Discov*. 2021 Feb 18;

7. Borst P, Elferink RO. Mammalian ABC Transporters in Health and Disease. *Annual Review of Biochemistry*. 2002 Jun;71(1):537–92.

8. Kruh GD, Zeng H, Rea PA, Liu G, Chen ZS, Lee K, et al. MRP subfamily transporters and resistance to anticancer agents. *Journal of bioenergetics and biomembranes*. 2001 Dec;33(6):493–501.

9. Cole SPC. Targeting Multidrug Resistance Protein 1 (MRP1, *ABCC1*): Past, Present, and Future. *Annual Review of Pharmacology and Toxicology*. 2014 Jan 6;54(1):95–117.

10. Johnson ZL, Chen J. Structural Basis of Substrate Recognition by the Multidrug Resistance Protein MRP1. *Cell*. 2017 Mar;168(6):1075-1085.e9.

11. Arana MR, Altenberg GA. ATP-binding Cassette Exporters: Structure and Mechanism with a Focus on P-glycoprotein and MRP1. *Current medicinal chemistry*. 2019;26(7):1062–78.

12. Higgins CF, Gottesman MM. Is the multidrug transporter a flippase? *Trends in Biochemical Sciences*. 1992 Jan;17(1):18–21.

13. Hopper E, Belinsky MG, Zeng H, Tosolini A, Testa JR, Kruh GD. Analysis of the structure and expression pattern of MRP7 (ABCC10), a new member of the MRP subfamily. *Cancer Lett*. 2001 Jan 26;162(2):181–91.

14. Hopper E, Belinsky MG, Zeng H, Tosolini A, Testa JR, Kruh GD. Analysis of the structure and expression pattern of MRP7 (ABCC10), a new member of the MRP subfamily. *Cancer Letters*. 2001;162(2):181–91.

15. Kathawala RJ, Wang YJ, Ashby CR, Chen ZS. Recent advances regarding the role of ABC subfamily C member 10 (ABCC10) in the efflux of antitumor drugs. *Chinese Journal of Cancer*. 2014;33(5):223–30.

16. Chen Z-S, Hopper-Borge E, Belinsky MG, Shchaveleva I, Kotova E, Kruh GD. Characterization of the transport properties of human multidrug resistance protein 7 (MRP7, ABCC10). *Mol Pharmacol*. 2003 Feb;63(2):351–8.

17. Hopper-Borge EA, Churchill T, Paulose C, Nicolas E, Jacobs JD, Ngo O, et al. Contribution of Abcc10 (Mrp7) to in vivo paclitaxel resistance as assessed in Abcc10-/- mice. *Cancer Research*. 2011;71(10):3649–57.

18. Hopper-Borge E, Chen ZS, Shchaveleva I, Belinsky MG, Kruh GD. Analysis of the drug resistance profile of multidrug resistance protein 7 (ABCC10): Resistance to docetaxel. *Cancer Research*. 2004;64(14):4927–30.

19. Bessho Y, Oguri T, Ozasa H, Uemura T, Sakamoto H, Miyazaki M, et al. ABCC10/MRP7 is associated with vinorelbine resistance in non-small cell lung cancer. *Oncology reports*. 2009 Jan;21(1):263–8.

20. Zhang YK, Wang YJ, Gupta P, Chen ZS. Multidrug Resistance Proteins (MRPs) and Cancer Therapy. *AAPS Journal*. 2015;17(4):802–12.

21. Hopper-Borge E, Xu X, Shen T, Shi Z, Chen Z-S, Kruh GD. Human multidrug resistance protein 7 (ABCC10) is a resistance factor for nucleoside analogues and epothilone B. *Cancer research*. 2009 Jan 1;69(1):178–84.

22. Domanitskaya N, Wangari-Talbot J, Jacobs J, Peiffer E, Mahdaviyeh Y, Paulose C, et al. Abcc10 status affects mammary tumour growth, metastasis, and docetaxel treatment response. *British Journal of Cancer*. 2014;111(4):696–707.

23. Krizkova V, Dubova M, Susova S, Vycital O, Bruha J, Skala M, et al. Protein expression of ATP-binding cassette transporters ABCC10 and ABCC11 associates with survival of colorectal cancer patients. *Cancer Chemotherapy and Pharmacology*. 2016;78(3):595–603.

24. Mao X, He Z, Zhou F, Huang Y, Zhu G. Prognostic significance and molecular mechanisms of adenosine triphosphate-binding cassette subfamily C members in gastric cancer. *Medicine (United States)*. 2019;98(50).

25. Oguri T, Ozasa H, Uemura T, Bessho Y, Miyazaki M, Maeno K, et al. MRP7/ABCC10 expression is a predictive biomarker for the resistance to paclitaxel in non-small cell lung cancer. *Molecular Cancer Therapeutics*. 2008;7(5):1150–5.

26. Dabrowska M, Sirotnak FM. E2F site in the essential promoter region does not confer S phase-specific transcription of the ABCC10 gene in human prostate cancer cells. *Acta biochimica Polonica*. 2017;64(2):371–4.

27. Kharangarh S, Sandhu H, Tangadpalliwar S, Garg P. Predicting Inhibitors for Multidrug Resistance Associated Protein-2 Transporter by Machine Learning Approach. *Comb Chem High Throughput Screen*. 2018;21(8):557–66.

28. Jayaraj PB, Jain S. Ligand based virtual screening using SVM on GPU. *Computational Biology and Chemistry*. 2019 Dec;83:107143.

29. Huang S, Cai N, Pacheco PP, Narrandes S, Wang Y, Xu W. Applications of Support Vector Machine (SVM) Learning in Cancer Genomics. *Cancer Genomics Proteomics*. 2018 Feb;15(1):41–51.

30. Sanz H, Reverter F, Valim C. Enhancing SVM for survival data using local invariances and weighting. *BMC Bioinformatics*. 2020 May 19;21(1):193.

31. Heikamp K, Bajorath J. Support vector machines for drug discovery. *Expert Opinion on Drug Discovery*. 2014 Jan;9(1):93–104.

32. Hu B, Zhou X, Mohutsky MA, Desai PV. Structure-Property Relationships and Machine Learning Models for Addressing CYP3A4-Mediated Victim Drug-Drug Interaction Risk in Drug Discovery. *Mol Pharm*. 2020 Sep 8;17(9):3600–8.

33. Hussain W, Rasool N, Khan YD. Insights into Machine Learning-based approaches for Virtual Screening in Drug Discovery: Existing strategies and streamlining through FP-CADD. *Curr Drug Discov Technol*. 2020 Aug 6;

34. Lima AN, Philot EA, Trossini GHG, Scott LPB, Maltarollo VG, Honorio KM. Use of machine learning approaches for novel drug discovery. *Expert Opin Drug Discov*. 2016;11(3):225–39.

35. Carpenter KA, Huang X. Machine Learning-based Virtual Screening and Its Applications to Alzheimer's Drug Discovery: A Review. *Curr Pharm Des*. 2018;24(28):3347–58.

36. Gao K, Nguyen DD, Sresht V, Mathiowetz AM, Tu M, Wei G-W. Are 2D fingerprints still valuable for drug discovery? *Phys Chem Chem Phys*. 2020 Apr 29;22(16):8373–90.

37. Mogensen UB, Gerds TA. A random forest approach for competing risks based on pseudo-values. *Stat Med*. 2013 Aug 15;32(18):3102–14.

38. Zhang H, Wang M. Search for the smallest random forest. *Stat Interface*. 2009 Jan 1;2(3):381.

39. Zhang M, Su Q, Lu Y, Zhao M, Niu B. Application of Machine Learning Approaches for Protein-protein Interactions Prediction. *Med Chem*. 2017;13(6):506–14.

40. Curtis C, Liu C, Bollerman TJ, Pianykh OS. Machine Learning for Predicting Patient Wait Times and Appointment Delays. *J Am Coll Radiol*. 2018 Sep;15(9):1310–6.

41. Mahajan SM, Ghani R. Using Ensemble Machine Learning Methods for Predicting Risk of Readmission for Heart Failure. *Stud Health Technol Inform*. 2019 Aug 21;264:243–7.

42. Jiang T, Gradus JL, Rosellini AJ. Supervised Machine Learning: A Brief Primer. *Behav Ther*. 2020 Sep;51(5):675–87.

43. Gorczyca MT, Toscano NC, Cheng JD. The trauma severity model: An ensemble machine learning approach to risk prediction. *Comput Biol Med*. 2019 May;108:9–19.

44. Svetnik V, Liaw A, Tong C, Culberson JC, Sheridan RP, Feuston BP. Random forest: a classification and regression tool for compound classification and QSAR modeling. *J Chem Inf Comput Sci*. 2003 Dec;43(6):1947–58.

45. Sato T, Honma T, Yokoyama S. Combining machine learning and pharmacophore-based interaction fingerprint for in silico screening. *J Chem Inf Model*. 2010 Jan;50(1):170–85.

46. Abdo A, Salim N. Similarity-based virtual screening with a bayesian inference network. *ChemMedChem*. 2009 Feb;4(2):210–8.

47. Vamathevan J, Clark D, Czodrowski P, Dunham I, Ferran E, Lee G, et al. Applications of machine learning in drug discovery and development. *Nat Rev Drug Discov*. 2019 Jun;18(6):463–77.

48. Costa PR, Acencio ML, Lemke N. A machine learning approach for genome-wide prediction of morbid and druggable human genes based on systems-level data. *BMC Genomics*. 2010 Dec 22;11 Suppl 5:S9.

49. Wu Z, Ramsundar B, Feinberg EN, Gomes J, Geniesse C, Pappu AS, et al. MoleculeNet: a benchmark for molecular machine learning. *Chem Sci*. 2018 Jan 14;9(2):513–30.

50. Robles-Fernandez I, Rodriguez-Serrano F, Alvarez P, Ortiz R, Rama A, Prados J, et al. Antitumor Properties of Natural Compounds and Related Molecules. *Recent Pat Anticancer Drug Discov*. 2013 Jun 1;8(3):203–15.

51. Sone K, Oguri T, Uemura T, Takeuchi A, Fukuda S, Takakuwa O, et al. Genetic variation in the ATP binding cassette transporter ABCC10 is associated with neutropenia for docetaxel in Japanese lung cancer patients cohort. *BMC Cancer* [Internet]. 2019 Dec [cited 2020 Apr 30];19(1). Available from: https://bmccancer.biomedcentral.com/articles/10.1186/s12885-019-5438-2

52. Daood M, Tsai C, Ahdab-Barmada M, Watchko JF. ABC transporter (P-gp/ABCB1, MRP1/ABCC1, BCRP/ABCG2) expression in the developing human CNS. *Neuropediatrics*. 2008 Aug;39(4):211–8.

53. Ferreira RJ, Bonito CA, Cordeiro MNDS, Ferreira M-JU, dos Santos DJVA. Structure-function relationships in ABCG2: insights from molecular dynamics simulations and molecular docking studies. *Scientific Reports* [Internet]. 2017 Dec [cited 2020 May 15];7(1). Available from: http://www.nature.com/articles/s41598-017-15452-z

54. Cole SPC. Multidrug Resistance Protein 1 (MRP1, ABCC1), a "Multitasking" ATP-binding Cassette (ABC) Transporter. *Journal of Biological Chemistry*. 2014 Nov 7;289(45):30880–8.

55. Zhao H, Huang Y, Shi J, Dai Y, Wu L, Zhou H. ABCC10 Plays a Significant Role in the Transport of Gefitinib and Contributes to Acquired Resistance to Gefitinib in NSCLC. *Frontiers in Pharmacology* [Internet]. 2018 Nov 20 [cited 2020 May 1];9. Available from: https://www.frontiersin.org/article/10.3389/fphar.2018.01312/full

56. Oguri. ABCC10/MRP7 is associated with vinorelbine resistance in non-small cell lung cancer. *Oncology Reports* [Internet]. 1994 [cited 2020 May 1]; Available from: http://www.spandidos-publications.com/or/article.jsp?article_id=or_21_1_263

57. Hopper-Borge E, Xu X, Shen T, Shi Z, Chen Z-S, Kruh GD. Human Multidrug Resistance Protein 7 (ABCC10) Is a Resistance Factor for Nucleoside Analogues and Epothilone B. *Cancer Research*. 2009 Jan 1;69(1):178–84.

58. Wu K, Yang Y, Zhao J, Zhao S. BAG3-mediated miRNA let-7g and let-7i inhibit proliferation and enhance apoptosis of human esophageal carcinoma cells by targeting the drug transporter ABCC10. *Cancer Letters*. 2016 Feb;371(1):125–33.

59. Kathawala RJ, Wei L, Anreddy N, Chen K, Patel A, Alqahtani S, et al. The small molecule tyrosine kinase inhibitor NVP-BHG712 antagonizes ABCC10-mediated paclitaxel resistance: a preclinical and pharmacokinetic study. *Oncotarget* [Internet]. 2015 Jan 1 [cited 2020 May 1];6(1). Available from: http://www.oncotarget.com/fulltext/2638

60. Anreddy N, Patel A, Sodani K, Kathawala RJ, Chen EP, Wurpel JND, et al. PD173074, a selective FGFR inhibitor, reverses MRP7 (ABCC10)-mediated MDR. *Acta Pharmaceutica Sinica B*. 2014 Jun;4(3):202–7.

61. Tiwari AK, Sodani K, Dai C, Abuznait AH, Singh S, Xiao Z-J, et al. Nilotinib potentiates anticancer drug sensitivity in murine ABCB1-, ABCG2-, and ABCC10-multidrug resistance xenograft models. *Cancer Letters*. 2013 Jan;328(2):307–17.

62. Kuang Y-H, Shen T, Chen X, Sodani K, Hopper-Borge E, Tiwari AK, et al. Lapatinib and erlotinib are potent reversal agents for MRP7 (ABCC10)-mediated multidrug resistance. *Biochemical Pharmacology*. 2010 Jan;79(2):154–61.

63. Deng W, Dai C-L, Chen J-J, Kathawala RJ, Sun Y-L, Chen H-F, et al. Tandutinib (MLN518) reverses multidrug resistance by inhibiting the efflux activity of the multidrug resistance protein 7 (ABCC10). *Oncology Reports*. 2013 Jun;29(6):2479–85.

64. Narayanan S, Teng Q-X, Koya J, Wang J, Assaraf YG, Ashby CR, et al. Poly (ADP-ribose) polymerase (PARP) inhibitors as chemosensitizing compounds for the treatment of drug resistant cancers. *J Mol Clinic Med*. 2019 Sep;2(3):55–67.

65. Krizkova V, Dubova M, Susova S, Vycital O, Bruha J, Skala M, et al. Protein expression of ATP-binding cassette transporters ABCC10 and ABCC11 associates with survival of colorectal cancer patients. *Cancer Chemotherapy and Pharmacology*. 2016 Sep;78(3):595–603.

66. Liptrott NJ, Pushpakom S, Wyen C, Fätkenheuer G, Hoffmann C, Mauss S, et al. Association of ABCC10 polymorphisms with nevirapine plasma concentrations in the German Competence Network for HIV/AIDS: *Pharmacogenetics and Genomics*. 2012 Jan;22(1):10–9.

67. Johnson ZL, Chen J. ATP Binding Enables Substrate Release from Multidrug Resistance Protein 1. *Cell*. 2018 Jan;172(1–2):81-89.e10.

68. Cavasotto CN, Phatak SS. Homology modeling in drug discovery: current trends and applications. *Drug Discov Today*. 2009 Jul;14(13–14):676–83.

69. Engh RA, Huber R. Accurate bond and angle parameters for X-ray protein structure refinement. *Acta Crystallographica Section A Foundations of Crystallography*. 1991 Jul 1;47(4):392–400.

70. Morris AL, MacArthur MW, Hutchinson EG, Thornton JM. Stereochemical quality of protein structure coordinates. *Proteins: Structure, Function, and Genetics*. 1992 Apr;12(4):345–64.

71. Shen M-Y, Sali A. Statistical potential for assessment and prediction of protein structures. *Protein Sci*. 2006 Nov;15(11):2507–24.

72. Laskowski RA, MacArthur MW, Moss DS, Thornton JM. PROCHECK: a program to check the stereochemical quality of protein structures. *Journal of Applied Crystallography*. 1993 Apr 1;26(2):283–91.

73. Studer G, Biasini M, Schwede T. Assessing the local structural quality of transmembrane protein models using statistical potentials (QMEANBrane). *Bioinformatics*. 2014 Sep 1;30(17):i505-511.

74. Benkert P, Biasini M, Schwede T. Toward the estimation of the absolute quality of individual protein structure models. *Bioinformatics*. 2011 Feb 1;27(3):343–50.

75. Colovos C, Yeates TO. Verification of protein structures: patterns of nonbonded atomic interactions. *Protein Sci*. 1993 Sep;2(9):1511–9.

76. Chen VB, Arendall WB, Headd JJ, Keedy DA, Immormino RM, Kapral GJ, et al. MolProbity: all-atom structure validation for macromolecular crystallography. *Acta Crystallogr D Biol Crystallogr*. 2010 Jan;66(Pt 1):12–21.

77. Wang J-Q, Li JY, Teng Q-X, Lei Z-N, Ji N, Cui Q, et al. Venetoclax, a BCL-2 Inhibitor, Enhances the Efficacy of Chemotherapeutic Agents in Wild-Type ABCG2-Overexpression-Mediated MDR Cancer Cells. *Cancers*. 2020 Feb 18;12(2):466.

78. Evans DJ, Holian BL. The Nose–Hoover thermostat. *The Journal of Chemical Physics*. 1985 Oct 15;83(8):4069–74.

79. Martyna GJ, Tobias DJ, Klein ML. Constant pressure molecular dynamics algorithms. *The Journal of Chemical Physics*. 1994 Sep;101(5):4177–89.

80. Bakan A, Meireles LM, Bahar I. ProDy: Protein Dynamics Inferred from Theory and Experiments. *Bioinformatics*. 2011 Jun 1;27(11):1575–7.

81. Humphrey W, Dalke A, Schulten K. VMD: Visual molecular dynamics. *Journal of Molecular Graphics*. 1996 Feb;14(1):33–8.

82. Ji N, Yang Y, Cai C-Y, Lei Z-N, Wang J-Q, Gupta P, et al. VS-4718 Antagonizes Multidrug Resistance in ABCB1- and ABCG2-Overexpressing Cancer Cells by Inhibiting the Efflux Function of ABC Transporters. *Frontiers in Pharmacology* [Internet]. 2018 Oct 30 [cited 2018 Dec 29];9. Available from: https://www.frontiersin.org/article/10.3389/fphar.2018.01236/full

83. Zhang W, Fan Y-F, Cai C-Y, Wang J-Q, Teng Q-X, Lei Z-N, et al. Olmutinib (BI1482694/HM61713), a Novel Epidermal Growth Factor Receptor Tyrosine Kinase Inhibitor, Reverses ABCG2-Mediated Multidrug Resistance in Cancer Cells. *Frontiers in Pharmacology* [Internet]. 2018 Oct 9 [cited 2018 Dec 29];9. Available from: https://www.frontiersin.org/article/10.3389/fphar.2018.01097/full

84. Trott O, Olson AJ. AutoDock Vina: Improving the speed and accuracy of docking with a new scoring function, efficient optimization, and multithreading. *Journal of Computational Chemistry*. 2009;NA-NA.

85. Zhang Y, Sham YY, Rajamani R, Gao J, Portoghese PS. Homology Modeling and Molecular Dynamics Simulations of the Mu Opioid Receptor in a Membrane-Aqueous System. *ChemBioChem*. 2005 May 6;6(5):853–9.

86. Bakos E, Evers R, Szakács G, Tusnády GE, Welker E, Szabó K, et al. Functional multidrug resistance protein (MRP1) lacking the N-terminal transmembrane domain. *The Journal of biological chemistry*. 1998 Nov 27;273(48):32167–75.

87. Robert X, Gouet P. Deciphering key features in protein structures with the new ENDscript server. *Nucleic Acids Research*. 2014 Jul 1;42(W1):W320–4.

88. Bakan A, Dutta A, Mao W, Liu Y, Chennubhotla C, Lezon TR, et al. Evol and ProDy for bridging protein sequence evolution and structural dynamics. *Bioinformatics*. 2014 Sep 15;30(18):2681–3.

89. Hopper-Borge E, Chen Z-S, Shchaveleva I, Belinsky MG, Kruh GD. Analysis of the Drug Resistance Profile of Multidrug Resistance Protein 7 (ABCC10): Resistance to Docetaxel. *Cancer Research*. 2004 Jul 15;64(14):4927–30.

90. Bessho Y, Oguri T, Ozasa H, Uemura T, Sakamoto H, Miyazaki M, et al. ABCC10/MRP7 is associated with vinorelbine resistance in non-small cell lung cancer. *Oncol Rep*. 2009 Jan;21(1):263–8.

91. Zhou Y, Hopper-Borge E, Shen T, Huang X-C, Shi Z, Kuang Y-H, et al. Cepharanthine is a potent reversal agent for MRP7(ABCC10)-mediated multidrug resistance. *Biochemical Pharmacology*. 2009 Mar;77(6):993–1001.

92. Chen J-J, Sun Y-L, Tiwari AK, Xiao Z-J, Sodani K, Yang D-H, et al. PDE5 inhibitors, sildenafil and vardenafil, reverse multidrug resistance by inhibiting the efflux function of multidrug resistance protein 7 (ATP-binding Cassette C10) transporter. *Cancer Science*. 2012 Aug;103(8):1531–7.

93. Sun Y-L, Chen J-J, Kumar P, Chen K, Sodani K, Patel A, et al. Reversal of MRP7 (ABCC10)-mediated multidrug resistance by tariquidar. *PLoS ONE*. 2013;8(2):e55576.

94. Abraham I, Jain S, Wu C-P, Khanfar MA, Kuang Y, Dai C-L, et al. Marine sponge-derived sipholane triterpenoids reverse P-glycoprotein (ABCB1)-mediated multidrug resistance in cancer cells. *Biochemical Pharmacology*. 2010 Nov;80(10):1497–506.

95. Zeng H, Chen ZS, Belinsky MG, Rea PA, Kruh GD. Transport of methotrexate (MTX) and folates by multidrug resistance protein (MRP) 3 and MRP1: effect of polyglutamylation on MTX transport. *Cancer Res*. 2001 Oct 1;61(19):7225–32.

96. Norman BH. Inhibitors of MRP1-mediated multidrug resistance. *Drugs of the Future*. 1998;23(9):1001.

97. Kathawala RJ, Gupta P, Ashby CR, Chen Z-S. The modulation of ABC transporter-mediated multidrug resistance in cancer: A review of the past decade. *Drug Resistance Updates*. 2015 Jan;18:1–17.

98. Ferreira RJ, Ferreira M-JU, Dos Santos DJVA. Assessing the Stabilization of P-Glycoprotein's Nucleotide-Binding Domains by the Linker, Using Molecular Dynamics. *Mol Inform*. 2013 Jun;32(5–6):529–40.

99. Wu Z-X, Peng Z, Yang Y, Wang J-Q, Teng Q-X, Lei Z-N, et al. M3814, a DNA-PK Inhibitor, Modulates ABCG2-Mediated Multidrug Resistance in Lung Cancer Cells. *Front Oncol* [Internet]. 2020 May 12 [cited 2020 May 12];10. Available from: https://www.frontiersin.org/article/10.3389/fonc.2020.00674/full

100. Wu Z-X, Yang Y, Teng Q-X, Wang J-Q, Lei Z-N, Wang J-Q, et al. Tivantinib, A c-Met Inhibitor in Clinical Trials, Is Susceptible to ABCG2-Mediated Drug Resistance. *Cancers*. 2020 Jan 12;12(1):186.

101. Lee KPK, Chen J, MacKinnon R. Molecular structure of human KATP in complex with ATP and ADP. *eLife* [Internet]. 2017 Dec 29 [cited 2020 May 15];6. Available from: https://elifesciences.org/articles/32481

102. Kim Y, Chen J. Molecular structure of human P-glycoprotein in the ATP-bound, outward-facing conformation. *Science*. 2018 Feb 23;359(6378):915–9.

103. Ferreira RJ, Ferreira M-JU, dos Santos DJVA. Insights on P-Glycoprotein's Efflux Mechanism Obtained by Molecular Dynamics Simulations. *Journal of Chemical Theory and Computation*. 2012 Jun 12;8(6):1853–64.

104. Manolaridis I, Jackson SM, Taylor NMI, Kowal J, Stahlberg H, Locher KP. Cryo-EM structures of a human ABCG2 mutant trapped in ATP-bound and substrate-bound states. *Nature*. 2018 Nov;563(7731):426–30.

105. Ferreira RJ, Ferreira M-JU, dos Santos DJVA. Molecular docking characterizes substrate-binding sites and efflux modulation mechanisms within P-glycoprotein. *J Chem Inf Model*. 2013 Jul 22;53(7):1747–60.

106. Ji N, Yang Y, Cai C-Y, Lei Z-N, Wang J-Q, Gupta P, et al. Selonsertib (GS-4997), an ASK1 inhibitor, antagonizes multidrug resistance in ABCB1- and ABCG2-overexpressing cancer cells. *Cancer Lett*. 2019 Jan;440–441:82–93.

107. Ji N, Yang Y, Lei Z-N, Cai C-Y, Wang J-Q, Gupta P, et al. Ulixertinib (BVD-523) antagonizes ABCB1- and ABCG2-mediated chemotherapeutic drug resistance. *Biochem Pharmacol*. 2018 Dec;158:274–85.

108. Wang J-Q, Lei Z-N, Teng Q-X, Wang B, Ma L-Y, Liu H-M, et al. Abstract 2983: A synthetic derivative of 1,2,3-triazole-pyrimidine hybrid reverses multidrug resistance mediated by MRP7. In: Experimental and Molecular Therapeutics [Internet]. American Association for Cancer Research; 2020 [cited 2020 Sep 10].

p. 2983–2983. Available from: http://cancerres.aacrjournals.org/lookup/doi/10.1158/1538-7445.AM2020-2983

109. Wang B, Zhao B, Chen Z-S, Pang L-P, Zhao Y-D, Guo Q, et al. Exploration of 1,2,3-triazole-pyrimidine hybrids as potent reversal agents against ABCB1-mediated multidrug resistance. *Eur J Med Chem*. 2018 Jan 1;143:1535–42.

110. Wang B, Ma L-Y, Wang J-Q, Lei Z-N, Gupta P, Zhao Y-D, et al. Discovery of 5-Cyano-6-phenylpyrimidin Derivatives Containing an Acylurea Moiety as Orally Bioavailable Reversal Agents against P-Glycoprotein-Mediated Mutidrug Resistance. *J Med Chem*. 2018 Jul 26;61(14):5988–6001.

111. Wang J, Yang D-H, Yang Y, Wang J-Q, Cai C-Y, Lei Z-N, et al. Overexpression of ABCB1 Transporter Confers Resistance to mTOR Inhibitor WYE-354 in Cancer Cells. *Int J Mol Sci*. 2020 Feb 19;21(4):1387.

112. Wu Z, Yang Y, Wang G, Wang J, Teng Q, Sun L, et al. Dual TTK/CLK2 inhibitor, CC-671, selectively antagonizes ABCG2-mediated multidrug resistance in lung cancer cells. *Cancer Sci*. 2020 Aug;111(8):2872–82.

113. Ji N, Yang Y, Cai C-Y, Lei Z-N, Wang J-Q, Gupta P, et al. VS-4718 Antagonizes Multidrug Resistance in ABCB1- and ABCG2-Overexpressing Cancer Cells by Inhibiting the Efflux Function of ABC Transporters. *Front Pharmacol* [Internet]. 2018 Oct 30 [cited 2018 Dec 29];9. Available from: https://www.frontiersin.org/article/10.3389/fphar.2018.01236/full

114. Yang Y, Ji N, Teng Q-X, Cai C-Y, Wang J-Q, Wu Z-X, et al. Sitravatinib, a Tyrosine Kinase Inhibitor, Inhibits the Transport Function of ABCG2 and Restores Sensitivity to Chemotherapy-Resistant Cancer Cells in vitro. *Front Oncol* [Internet]. 2020 May 12 [cited 2020 May 12];10. Available from: https://www.frontiersin.org/article/10.3389/fonc.2020.00700/full

115. Luo X, Teng Q-X, Dong J-Y, Yang D-H, Wang M, Dessie W, et al. Antimicrobial Peptide Reverses ABCB1-Mediated Chemotherapeutic Drug Resistance. *Front Pharmacol* [Internet]. 2020 Aug 7 [cited 2020 Aug 31];11. Available from: https://www.frontiersin.org/article/10.3389/fphar.2020.01208/full

116. Zhang Y, Wu Z-X, Yang Y, Wang J-Q, Li J, Sun Z, et al. Poziotinib Inhibits the Efflux Activity of the ABCB1 and ABCG2 Transporters and the Expression of the ABCG2 Transporter Protein in Multidrug Resistant Colon Cancer Cells. *Cancers*. 2020 Nov 4;12(11):3249.

117. Wang, J-Q, Cui Q, Lei Z-N, Teng Q-X, Ji N, Lin L, et al. Insights on the structure–function relationship of human multidrug resistance protein 7 (MRP7/ABCC10) from molecular dynamics simulations and docking studies. *MedComm*. 2021;1:1–15.

118. Trott O, Olson AJ. AutoDock Vina: Improving the speed and accuracy of docking with a new scoring function, efficient optimization, and multithreading. *J Comput Chem*. 2009;NA-NA.

119. Anreddy N, Patel A, Sodani K, Kathawala RJ, Chen EP, Wurpel JND, et al. PD173074, a selective FGFR inhibitor, reverses MRP7 (ABCC10)-mediated MDR. *Acta Pharm Sin B*. 2014 Jun;4(3):202–7.

120. Krizkova V, Dubova M, Susova S, Vycital O, Bruha J, Skala M, et al. Protein expression of ATP-binding cassette transporters ABCC10 and ABCC11 associates with survival of colorectal cancer patients. *Cancer Chemother Pharmacol*. 2016 Sep;78(3):595–603.

121. Liptrott NJ, Pushpakom S, Wyen C, Fätkenheuer G, Hoffmann C, Mauss S, et al. Association of ABCC10 polymorphisms with nevirapine plasma concentrations in the German Competence Network for HIV/AIDS: *Pharmacogenet Genomics*. 2012 Jan;22(1):10–9.

122. Hopper E, Belinsky MG, Zeng H, Tosolini A, Testa JR, Kruh GD. Analysis of the structure and expression pattern of MRP7 (ABCC10), a new member of the MRP subfamily. *Cancer Lett*. 2001 Jan;162(2):181–91.

123. Cui Q, Cai C-Y, Wang J-Q, Zhang S, Gupta P, Ji N, et al. Chk1 Inhibitor MK-8776 Restores the Sensitivity of Chemotherapeutics in P-glycoprotein Overexpressing Cancer Cells. *Int J Mol Sci*. 2019 Aug 22;20(17):4095.

124. Shen T, Kuang Y-H, Ashby CR, Lei Y, Chen A, Zhou Y, et al. Imatinib and Nilotinib Reverse Multidrug Resistance in Cancer Cells by Inhibiting the Efflux Activity of the MRP7 (ABCC10). Fox D, editor. *PLoS ONE*. 2009 Oct 20;4(10):e7520.

125. Wang, Cui Q, Lei Z-N, Teng Q-X, Ji N, Lin L, et al. Insights on the structure–function relationship of human multidrug resistance protein 7 (MRP7/ABCC10) from molecular dynamics simulations and docking studies. *MedComm*. 2021;1:1–15.

126. Zhou Y, Hopper-Borge E, Shen T, Huang X-C, Shi Z, Kuang Y-H, et al. Cepharanthine is a potent reversal agent for MRP7(ABCC10)-mediated multidrug resistance. *Biochem Pharmacol*. 2009 Mar;77(6):993–1001.

127. Szakács G, Annereau JP, Lababidi S, Shankavaram U, Arciello A, Bussey KJ, et al. Predicting drug sensitivity and resistance: profiling ABC transporter genes in cancer cells. *Cancer cell*. 2004 Aug;6(2):129–37.

128. Pinto M, Trauner M, Ecker GF. An In Silico Classification Model for Putative ABCC2 Substrates. *Mol Inf*. 2012 Aug;31(8):547–53.

129. Cao D-S, Xu Q-S, Hu Q-N, Liang Y-Z. ChemoPy: freely available python package for computational biology and chemoinformatics. *Bioinformatics*. 2013 Apr 15;29(8):1092–4.

130. Chen R, Liu X, Jin S, Lin J, Liu J. Machine Learning for Drug-Target Interaction Prediction. *Molecules*. 2018 Aug 31;23(9):2208.

131. Paul SM, Mytelka DS, Dunwiddie CT, Persinger CC, Munos BH, Lindborg SR, et al. How to improve R&D productivity: the pharmaceutical industry's grand challenge. *Nat Rev Drug Discov*. 2010 Mar;9(3):203–14.

132. Wolpert DH, Macready WG. No free lunch theorems for optimization. *IEEE Trans Evol Computat*. 1997 Apr;1(1):67–82.

133. Ezzat A, Wu M, Li X-L, Kwoh C-K. Computational prediction of drug-target interactions using chemogenomic approaches: an empirical survey. *Brief Bioinform*. 2019 Jul 19;20(4):1337–57.

134. Cui Q, Wang J-Q, Assaraf YG, Ren L, Gupta P, Wei L, et al. Modulating ROS to overcome multidrug resistance in cancer. *Drug Resist Updat*. 2018 Nov;41:1–25.

135. Zhang L, Tan J, Han D, Zhu H. From machine learning to deep learning: progress in machine intelligence for rational drug discovery. *Drug Discov Today*. 2017 Nov;22(11):1680–5.

136. Zhao D, Wang J, Sang S, Lin H, Wen J, Yang C. Relation path feature embedding based convolutional neural network method for drug discovery. *BMC Med Inform Decis Mak*. 2019 Apr 9;19(Suppl 2):59.

137. Agarwal R, Kaye SB. Ovarian cancer: strategies for overcoming resistance to chemotherapy. *Nat Rev Cancer*. 2003 Jul;3(7):502–16.

138. Cheung L, Flemming CL, Watt F, Masada N, Yu DMT, Huynh T, et al. High-throughput screening identifies Ceefourin 1 and Ceefourin 2 as highly selective inhibitors of multidrug resistance protein 4 (MRP4). *Biochemical Pharmacology*. 2014 Sep;91(1):97–108.

139. Choudhury C, Priyakumar UD, Sastry GN. Dynamics based pharmacophore models for screening potential inhibitors of mycobacterial cyclopropane synthase. *J Chem Inf Model*. 2015 Apr 27;55(4):848–60.

140. Zhang W, Chen Y, Liu F, Luo F, Tian G, Li X. Predicting potential drug-drug interactions by integrating chemical, biological, phenotypic and network data. *BMC Bioinformatics*. 2017 Jan 5;18(1):18.

141. Jing Y, Bian Y, Hu Z, Wang L, Xie X-Q. Deep Learning for Drug Design: an Artificial Intelligence Paradigm for Drug Discovery in the Big Data Era. *AAPS J*. 2018 Mar 30;20(3):58.

142. Rifaioglu AS, Atas H, Martin MJ, Cetin-Atalay R, Atalay V, Doğan T. Recent applications of deep learning and machine intelligence on in silico drug discovery: methods, tools and databases. *Brief Bioinform*. 2019 Sep 27;20(5):1878–912.

143. Bray F, Ferlay J, Soerjomataram I, Siegel RL, Torre LA, Jemal A. Global cancer statistics 2018: GLOBOCAN estimates of incidence and mortality worldwide for 36 cancers in 185 countries. *CA: A Cancer Journal for Clinicians*. 2018 Nov;68(6):394–424.

Vita

Name	*Jingquan Wang*
Baccalaureate Degree	*Bachelor of Science* *Shantou University ,* *Shantou, China* *Major: Biotechnology*
Date Graduated	*July, 2015*

Name	*Jingquan Wang*
Other Degrees and Certificates	*Master of Science*, *Georgia Institute of Technology,* *Atlanta, GA* *Major: Computer Science*
Date Graduated	*May, 2021*